Combinatorial high throughput synthesis of high entropy alloys

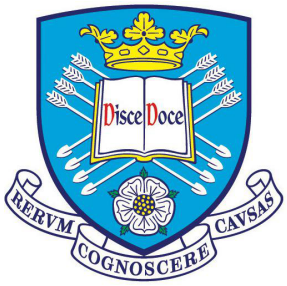

Laura Asensio Dominguez

Department of Materials Science and Engineering

University of Sheffield

This dissertation is submitted for the degree of

Doctor of Philosophy

September 2016

A mis abuelos:
Manuel Asensio Martín de Lucía,
María Domínguez Sánchez,
Pascasia Arévalo Moreno y Pascual Domínguez Arévalo

Declaration

I hereby declare that except where specific reference is made to the work of others, the contents of this dissertation are original and have not been submitted in whole or in part for consideration for any other degree or qualification in this, or any other university. This dissertation is my own work and contains nothing which is the outcome of work done in collaboration with others, except as specified in the text and Acknowledgements. This dissertation contains fewer than 65,000 words including appendices, bibliography, footnotes, tables and equations and has fewer than 150 figures.

Laura Asensio Dominguez
September 2016

Acknowledgements

Firstly, I would like to express my sincere gratitude to my supervisors Dr. Russell Goodall and Prof. Iain Todd for the continuous support of my PhD study and related research, for their patience, motivation, and immense knowledge. Their guidance, sometimes looking at different directions, helped me not only during the research stages but also on the writing of this thesis.

I would also like to thank to all and each members of Accelerated Metallurgy for their constructive comments, subjective points of view and their ethic values.
My sincere thanks also goes to all the members forming Mercury Centre, where most of the experimental part of this project has been carried out, and without them, this thesis would not have been possible. Particularly, Akemi, James, Fatos, Amit and Meurig for their comments and advices which have helped in shape this thesis.

I thank to all my colleagues Navid, Zhao, Chris, Everth and especially to Lampros for the support and stimulating discussions, for the days we have been working together until late and for all the fun we had in the last 3 years.

Last but not the least, I would like to thank to all my family for supporting me spiritually throughout writing this thesis and my life in general.

Abstract

This PhD thesis is a part of the Accelerated Metallurgy (AccMet) project funded under the Seventh Framework Programme. AccMet's aims consists on the delivery of an integrated pilot-scale facility for the combinatorial synthesis and testing of those unexplored material. The contribution of this thesis to AccMet has been expanded in 3 years while focused in the understanding and development of a methodology suitable for the combinatorial synthesis of novel materials, and particularly of High Entropy Alloys (HEAs). These novel materials are composed of multiple elements at near equiatomic levels with the capacity of forming simple crystalline phases such as bcc and fcc instead of the expected intermetallic compounds as well as their excellent combination of structural and functional properties compared to the traditional materials.

A mathematical technique known as Principal Component Analysis has been used here to identify patterns within a set of metallic systems forming a wide range of crystalline structures. This technique would not only speed up the compositional design stage but also contribute to the development of a virtual library containing all the explored systems.

Mercury Centre has been an important key during the synthesis of HEAs where Spark Plasma Sintering (SPS) and Electron Beam Melting (EBM) have been successfully applied for the development of the thesis.

The final combination of the design stage, production and characterisation of HEAs developed in this thesis would result in an advances technique suitable not only for the synthesis of novel HEAs, but also for the discovery of other unexplored systems.

Table of contents

List of figures

List of tables

Chapter 1

Introduction

Discovery of new materials has been essential for the development of civilisation; important as even epochs have been defined according the relevant material discovered and used at that time, such as the Stone, Bronze and Iron ages, besides of being strongly linked and influenced by the processing techniques employed to ease manufacture and improve the properties of those materials [14]. Traditional approaches for the discovery of new materials are based on the slow trial and error techniques to synthesise new materials, which have been (and are still being) followed by metallurgists over many decades. A traditional workflow begins by choosing the elements and their proportions, followed by processing and finally the testing of the resultant material in order to observe its properties. If the material has potential for a particular application, it would be followed by the development of the product, otherwise, the route would start again from the beginning but modifying the proportion of one or several elements included in the material in order to acquire the desired property, with the choice based perhaps on fundamental theory or the understanding of the behaviour of the element in other alloys.

This traditional methodology would require many years to produce one single novel material with a potential application. The time required to develop this material is crucial, because while a material is been developed, a new competitor material can be introduced for a potential application, which could mean that the first new material would never find a use. Consequently, both the time and financial resources used in development would be wasted.

In the last 50 years or so, an alternative approach called *Combinatorial materials synthesis* has arisen [15]; this was notably implemented to decrease time and cost related to drug discovery in pharmaceutical industries. Instead of following the slow and expensive conventional approach, it is based on the simultaneous synthesis of multiple samples in such

a manner that allows a rapid screening of their properties in order to identify suitable candidates for applications, saving time and money in the process. The chemists Peter G. Schultz together with a team of materials and physicists scientists worked on the extrapolation of the combinatorial principles from drug development to materials discovery and the successful of a publication related to the search for superconductors from a materials library marked the beginning of combinatorial materials science as a discipline [16].

Another point that must be considered in the search for new alloys is the number of elements. Looking at the periodic table, there are elements which are widely used, however there are others that are not so well known due to difficulty during processing, prices, scarcity, toxicity, etc. This results in the materials developed (to date) largely using a reduced number of elements. In addition, traditional alloy development strategies have also led to other effects; most conventional materials are composed of one or two elements in major proportion alloyed with others in minor quantity for improvement of the properties (for example superalloys). Discovery is therefore focused in the edges of the phase diagram whilst decreasing the probability of finding a suitable material composed of multiple components at major quantities (an example of such materials is the novel class of alloys commonly known as High Entropy Alloys, which are discussed in more detail in this work). Hence, study of the whole phase diagram (requiring many samples for a multi-element system) is required for a complete analysis of materials.

This thesis, which is structured in seven chapters, will introduce a suitable procedure to enable the synthesis and testing of novel materials composed of multiple components, while speeding up the process of discovery. The multicomponent alloys investigated are found at near equiatomic composition and are known as High Entropy Alloys (HEAs). The combinatorial methodology developed during this project covers 3 different stages: (1) the design of HEAs, (2) their synthesis and (3) their characterization and testing.

Chapter 2 will introduce HEAs, show their main features, stability and the most common behaviour; This chapter will also introduce Principal Component Analysis, PCA (technique used here as a exploratory technique to look at the determination of patterns within a dataset) as well as the conventional use of Spark Plasma Sintering, SPS and Electron Beam Melting, EBM as the techniques used for the production of samples in the alternative approach proposed in this project.

Chapter 3 will include the experimental conditions and methodology used for this project.

The characteristics of the materials employed; the conditions and operational parameters used with the equipment for each experiment; the general guidelines used for the metallographic preparation of the samples and for the screening technique.

The results of the main work developed for this thesis has been divided into 3 different chapters, 4, 5 and 6.

Chapter 4 will focus on how Principal Component Analysis is applied to the High Entropy Alloys collected from the literature in order to find any correlations and patters between those and the most relevant parameters (thermodynamic and electronic) previously used to determine their formation and hence permitting the design of HEAs.

Chapter 5 will explain the high throughput test methodology developed during this project, covering the synthesis, screening and characterization of HEAs. The methodology is validated with the synthesis of a known alloy system, $Ti_xFeCoCrNi$.

The combination of the results obtained in chapter 4 and chapter 5 have been used to set up a complete combinatorial procedure used for the discovery of novel refractory HEAs. Although, there remains scope for the process to be improved in order to increase the number of new samples synthesised and tested per day as well as the accuracy of the process, it is sufficient to be used as a starting point in the combinatorial discovery of High Entropy Alloys. Three novel refractory high entropy alloy systems have been successfully designed and produced; however, as it will be shown, changes on the process stage can create significant defects in the final samples.

Finally, chapter 7 will summarise the main ideas obtained for the suitability of combinatorial techniques for the discovery of HEAs, setting up some limitations, problems and possible future work that would be useful for the improvement of the technique.

Chapter 2

Literature review

This thesis is focussed on the synthesis of High Entropy Alloys using methodologies that allow speeding up the discovery of new materials. In order to achieve the objectives, both computational and technical tools have been required. This section will (1) define High Entropy Alloys showing some of their main features, properties and potential applications, (2) give a brief introduction to the "Combinatorial High Throughput" field as well as (3) introduce the techniques employed in this project.

2.1 High Entropy Alloys

2.1.1 Motivation and birth of Multicomponent High Entropy Alloys

When following a conventional strategy, the development of new materials begins with testing of a single material and then subsequently adding or removing small proportions of alloying elements until suitable properties for a certain application are found. This means that the final material is likely to be composed of one or two principal elements, with numerous other elements in small quantities. Using this conventional approach, it is easy to understand two main aspects: (1) the time required for developing a new material is huge and (2) the fact that the alloy system is composed of one or two principal elements only reduces the probability of finding the proper composition for a specific application.

Figure 2.1 shows sketch of both a ternary and a quaternary phase diagram, indicating the most common areas where a conventional strategy would focus on, leaving blank the centre of the diagram, where the elemental proportion is near-equiatomic. Vincent [17] in 1981 and later Knight [18] in 1995 published their work focused on understanding materials features found in this unexplored area of the phase diagram and called them *multicomponent*

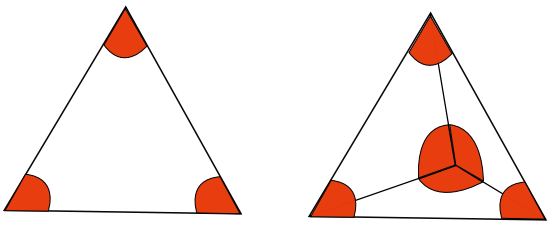

Fig. 2.1 Sketch of a ternary and a quaternary phase diagram highlighting areas where most easing alloy systems have been discovered, being where the conventional strategy is focused [1].

alloys. Almost a decade later, Cantor [19] and Yeh [2] independently published their work on alloys composed of multiple principal elements at near-equiatomic compositions, such as FeCoCrNiMn, that were particularly noted for their ability to form simple crystalline structures instead of the expected brittle intermetallic compounds. While Cantor kept the name of those alloy systems as *Multicomponent Alloys*, Yeh named them *High Entropy Alloys (HEAs)* due to the resultant increased entropy of mixing with increasing the number of elements within the equiatomic level and therefore due to his belief in configurational entropy, S_{conf}, as the main factor forming the simple crystalline structures [20].

In 10 years of research there have been more than 150 publications under the name of "High Entropy Alloys" (see Figure 2.2). The curiosity of understanding the physics behind these novel multicomponent equiatomic alloys, which can form simple crystalline structures and the exceptional properties that they are able to achieve are some of the reasons for great interest in HEAs.

Although, the understanding of HEAs is still under investigation and different researchers do not all agree on the interpretation of results, at this stage in this project, a standard definition of Multicomponent High Entropy Alloys could be: *those alloys composed of multiple elements at near equiatomic composition, which tend to form simple solid solutions*. For instance, Yeh et al.[20] filed a patent application which defines HEAs under the limit of the number of elements being between 5 and 13, where the proportion of each should be higher than 5 at% and smaller than 35 at%, tend to form simple fcc or bcc solid solutions and their mechanical properties are much higher than those of conventional alloys. However, those first ideas are under constant evolution while shaping these "unknown novel materials."

Most of the HEAs already produced are composed of elements exclusively from the transition metals and under the compositional limitations proposed by Yeh et al. [20, 21]. However,

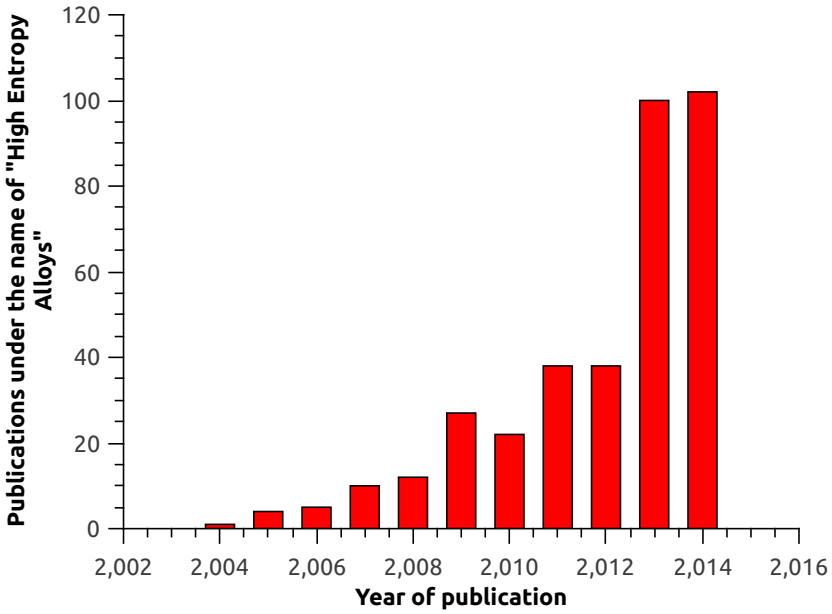

Fig. 2.2 Number of publications per year under the name of "High Entropy Alloy" from 2002 to 2014

in many cases they form not only simple fcc and/or bcc phases, but also mixtures of simple and complex phases such as bcc and/or fcc simple phases and intermetallic compounds. In addition, simple crystalline structures have also been found in alloys composed of less than 5 elements (e.g. FeCoCrNi [22]) or containing non transition metals (e.g. Si6FeCoCrNi [23]), which means that the Yeh original concept needs to be taken as a general guideline with no sharply defined boundary.

2.1.2 Basic concepts and factors affecting the formation of High Entropy Alloys

Josiah Willard Gibbs proposed a rule that gives the relationship between number of components and phases in a system under equilibrium conditions. At constant pressure, this relationship is:

$$P + F = C + 1 \tag{2.1}$$

where F is the number of thermodynamic degrees of freedom, which are the intensive variables such as temperature, pressure, composition, etc; C is the number of components in the system and P is the number of phases in equilibrium. The minimum number of degrees of freedom is zero, what makes the maximum number of phases in equilibrium to be higher

that the number of components as: $P_{max} = C + 1$. However, processing of materials at non equilibrium conditions can develop other transitory phases that would be retained at room temperature making the maximum number of phases to be even higher than the obtained at equilibrium: $P_{max} > C + 1$. Therefore, binary alloys often consist of more than 3 phases, and ternary of more than four phases at room temperature. Even though High Entropy Alloys are composed of multiple elements, surprisingly they show only a small number of phases, normally 1 single phase or no more than 3 or 4, staying far below the maximum equilibrium number of phases allowed by Gibbs phase rule.

Most processing techniques require operating conditions far away from the equilibrium, making the maximum number of phases greater than the shown by the Gibbs phase rule 2.1. As observed, most HEAs consist of single phases, however the reason for this is still under investigation.

From the point of view of statistical thermodynamics, when an alloy is composed of elements in equiatomic ratio, the entropy of the system can be expressed by the Boltzmann's entropy equation, which is related to the number of possible configurations, ω, as:

$$S_{conf} = k_B \ln\omega = -R\ln\frac{1}{n} = R\ln n \tag{2.2}$$

where S_{conf} is the configurational entropy, R is the gas constant, K_B is the Boltzmann constant and n is the number of elements involved in the system. When the number of components increases, the entropy of the system increases as well, increasing the disorder of the system and making more difficult the formation of intermetallic compounds which tend to form as ordered phases at low entropies.

According to Yeh [2] entropy of mixing is the responsible for the simplicity of the system in HEAs, reason for name them as "High Entropy Alloys". However, as will be shown, this parameter by itself is not the only one responsible for the formation of HEAs and moreover it may not have any effect on their formation.

Many factors affect the microstructure and properties of HEAs, but only four have been defined as the main ones: (1) The high entropy effect interfering on the formation of complex phases, (2) slowed down phase transformation could be due to a sluggish diffusion effect, (3) the lattice distortion effect could alter properties to an extent, and (4) the multimetallic cocktails [24].

According to the Second Law of Thermodynamics,

$$\Delta G_{mix} = \Delta H_{mix} - T\Delta S_{mix} \tag{2.3}$$

the state with the lowest Gibbs free energy of mixing ΔG_{mix} would be the equilibrium state. With Multiprincipal element HEAs at high temperatures, ΔH_{mix} (calculated as shown in Equation 2.4 where Ω_{ij} is $4\Delta H^{AB}_{mix}$, related to the mixing enthalpy of pairs of the elements A and B [25]) approaches zero, while the second term, $T\Delta S_{mix}$ would dominate the equation, leading to the formation of solid solutions rather than intermetallic compounds. On the other hand, if the enthalpy of mixing reaches too negative values, ordered phase intermetallic compounds are the most probable to form, while segregation may occur for positive enthalpy of mixing values. This fact makes the idea of ΔS_{mix} being the main contributor to the formation of solid solutions rather than intermetallic compounds in High Entropy Alloys reasonable. However, the entropy of mixing only takes into account the number of elements within the metallic system and does not consider the chemical contribution of each element. As will be shown in chapter 4, entropy of mixing is not the only significant contributor to the formation of HEAs, and indeed is less significant (within multicomponent equiatomic systems) than other contributions to the formation of simple phases.

$$\Delta H_{mix} = \sum_{i=1, i\neq j}^{n} \Delta H^{ij}_{mix} c_i c_j \tag{2.4}$$

In a multicomponent disordered metallic system, each element has neighbour atoms likely to be of different species, which can give rise to the lattice distorsion of the system as can be observed in the system CuCoNiCrFe, where the addition of Al has an influence on the lattice constant of the system (see Figure 2.3) [2].

William Hume-Rothery developed some empirical rules that help to understand the solid solubility formation of a binary system. Three are the main rules, which include the atomic effect, electronegativity and the electron concentration. This concept has been employed for understanding multicomponent alloy systems such as Bulk Metallic Glasses (BMGs) and HEAs.

- The atomic size effect states that, where the atomic difference between the solute and the solvent in a binary system does not exceed 15%, complete solubility is possible. This rule has been extrapolated to multicomponent systems, defined as *Atomic size difference,* δ and calculated as shown in Equation 2.5 (where n is the total number

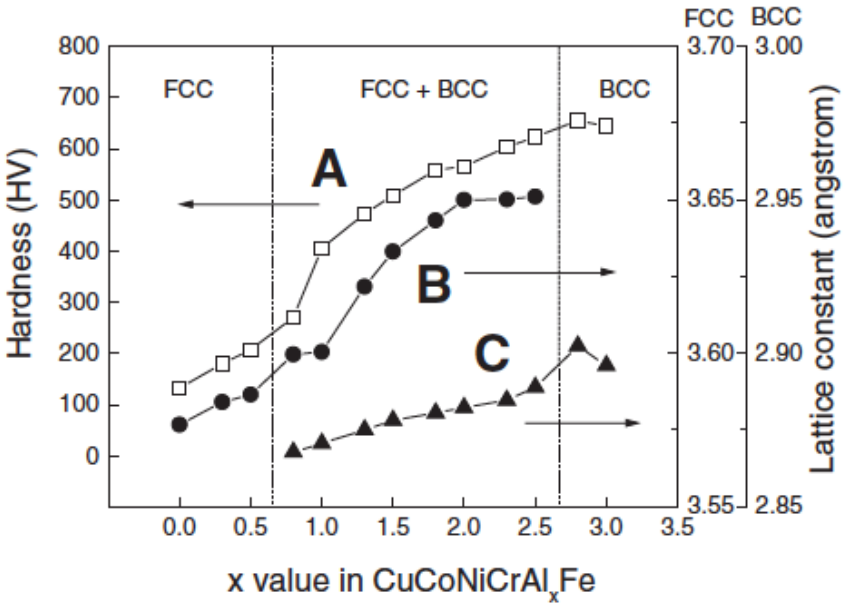

Fig. 2.3 Hardness and lattice constants of CuCoNiCrAlxFe alloy system with different Al contents: A) hardness of CuCoNiCrAlxFe alloys, B) lattice constant of fcc phase, C) lattice constant of bcc phase. [2]

of elements and c_i and r_i are the composition and atomic size of the i-th element respectively), allowing the determination of the atomic mismatch in the metallic system [26].

$$\delta = \sqrt{\sum_{i=1}^{n} c_i (1 - \frac{r_i}{\bar{r}})^2} \tag{2.5}$$

- Electronegativity is a chemical property that describes the tendency of an atom to attract electrons towards itself [27]. The Hume-Rothery rule of electronegativity especifies that the formation of solid solutions requires similar electronegativity between solvent and solute in the binary system, otherwise intermetallic compounds would form. The electronegativity difference between the elements of a multicomponent alloy is defined by Equation 2.6, where n is the number of elements, c_i and χ_i are the composition and electronegativity of the i-th element and χ_{av} is the mean of the electronegativity, $\sum c_i \chi_i$ [26].

$$\Delta\chi = \sqrt{\sum_{i=1}^{n} c_i (\chi_i - \chi_{av})^2} \tag{2.6}$$

- Valence Electron Concentration (VEC) indicates the number of all valence electrons in an alloy per atom and it is an important parameter for defining the structure and prop-

erties of a system. Its calculation for multicomponent systems is defined in Equation 2.7, where c_i and VEC_i are the composition and the Valence Electron Concentration of the i-th element in the system [6, 28, 29].

$$VEC = \sum_{i=1}^{n} c_i VEC_i \tag{2.7}$$

The concept of these rules is generally accepted for binary systems and their extrapolation to multicomponent alloy systems have therefore been applied to design of HEAs (along with ideas such as entropy).

Zhang et al. [3] analysed the effect of three parameters: the entropy of mixing, ΔS_{mix};

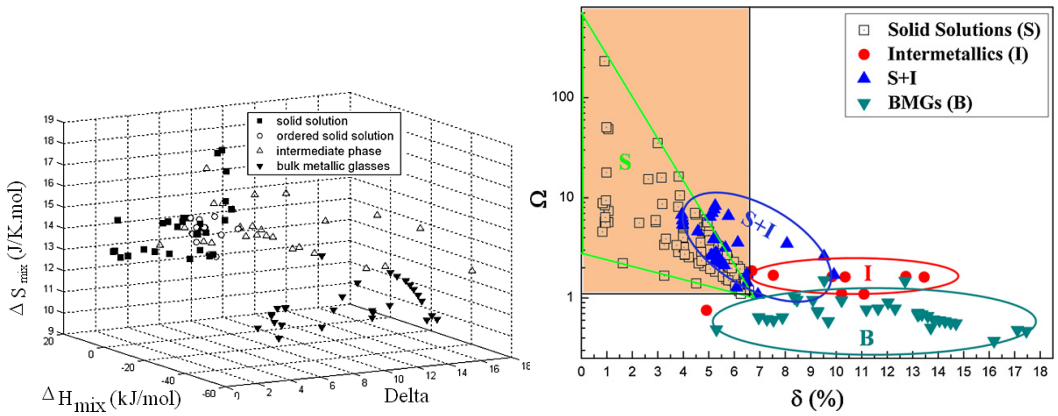

(a) (b)

Fig. 2.4 (a) The effect of ΔS_{mix}, ΔH_{mix} and δ on the phase formation of HEAs and typical multicomponent BMGs [3]. (b) the relationship between parameters δ and Ω for multicomponent alloy systems [4].

the enthalpy of mixing, ΔH_{mix}; and the atomic size difference, δ (see Figure 2.4a) on the formation of HEAs and BMGs. Further research showed how the combination of ΔH_{mix} and ΔS_{mix} to obtain a new parameter, Ω (Equation 2.8) allows the prediction of the formation of disordered solid solution phases (in other words the simple structure sought for HEAs) when $\Omega \geq 1.1$ and $\delta \leq 6.6\%$ [4] as shown in Figure 2.4b.

The results indicate that the formation of solid solutions in HEAs or amorphous phases in BMGs require different conditions of those three parameters. Note that intermetallics are also formed for some compositions that meet these requirements so the prediction is not perfect and therefore this technique was not able to discriminate between solid solutions and

intermediate phases.

$$\Omega = \frac{T_m \Delta S_{mix}}{\Delta H_{mix}} \tag{2.8}$$

In addition, Cunliffe et al. [30] defined and studied the effect of a critical temperature, T_c at equilibrium conditions, $\Delta G_{mix} = 0$ (shown in Equation 2.9), which helps in the prediction of solid solution phases of HEAs.

$$T_c = \frac{|\Delta H_{mix}|}{\Delta S_{mix}} \tag{2.9}$$

It is observed that the combination of equations 2.8 and 2.9 results in the ratio of temperatures shown in Equation 2.10 relating Ω to T_c.

$$\Omega = \frac{T_c}{T_m} \tag{2.10}$$

Under the same line of work, Guo et al. [5] analysed the relationship between the Hume-Rothery rules and these multicomponent alloy systems. It was found that electronegativity does not have a significant effect on the formation of solid solution, but that this requires enthalpy of mixing, entropy of mixing and atomic size difference to fit simultaneously within the ranges: $-22 \leq \Delta H_{mix} \leq 7 \text{kJ/mol}$, $11 \leq \Delta S_{mix} \leq 19.5 \text{J/molK}$ and $0 \leq \delta \leq 8.5$ as seen in Figure 2.5a.

In addition, VEC would help to classify the crystalline structure formation as shown

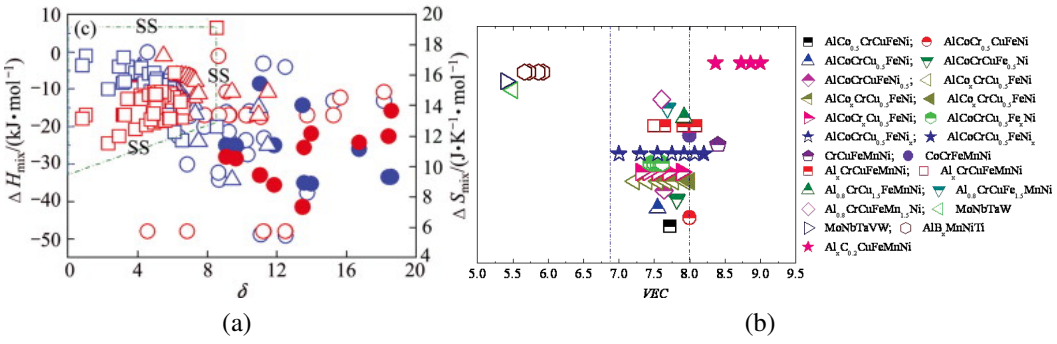

(a) (b)

Fig. 2.5 (a) Superimposed effect of all three parameters ΔH_{mix}, ΔS_{mix} and δ on phase stability in HEAs and BMGs [5] and (b) the effect of VEC on the stability of some HEAs [6].

in Figure 2.5b, where bcc phase alloys will form at VEC ≤ 6.87, fcc at VEC ≥ 8.0 and both of them will coexist at intermediate values: $6.87 \leq \text{VEC} \leq 8.0$ [6].

Those previous prediction techniques are useful to understand whether HEAs could potentially form for a given alloy system, however they are not able to discriminate between distinct phases and single or multiple combination of phases. Guo did not observe any effect of the electronegativity on the formation of solid solution phases. However, Poletti and Batezzati [7] plotted the effect of the electronegativity expressed in the experimental and theoretical Allen scale (related to the average energy of the valence electrons in a free atom), instead of the empirical Pauling scale, and VEC on the discrimination between simple and complex phases, as well as locate either bcc and fcc alloys on the map as seen in figure 2.6. It means that the electronegativity does have an important role on the formation of HEAs.

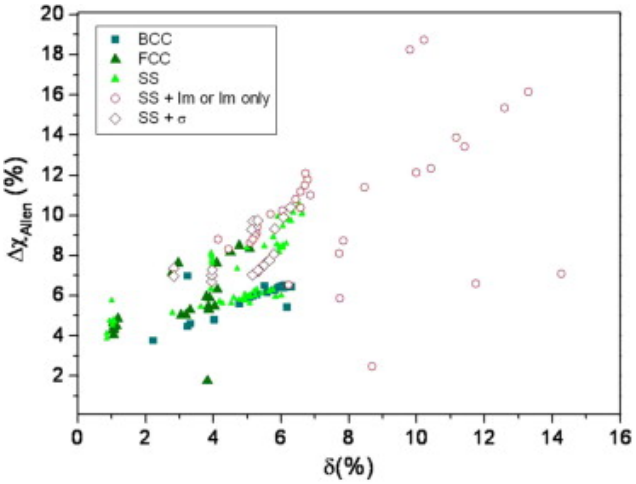

Fig. 2.6 Mapping of several HEAs according to their Allen electronegativity and atomic size difference grouped by their crystalline structure [7].

Nevertheless, despite these various advances, the fundamental parameters affecting the formation and stability of HEAs are not completely established yet, and therefore further work is required.

2.1.3 Processing routes

Both the composition and the processing technique selected will affect the final microstructure of the materials and therefore their properties. HEAs have been produced by a wide range of techniques within either ingot metallurgy, powder metallurgy or coating technology. Figure 2.7 shows a pie chart of the processing routes reported to be used for the synthesis of HEAs from 2004 until 2014. Liquid state techniques such as arc melting are the most common,

covering more than a half of all the production methods, due to its efficiency and low cost, since the synthesis of HEAs does not require any special conditions [19, 30–32]. Surface coating is the second most common method due to the potential applications when protecting components against damage (i.e. laser cladding, DC sputtering, etc) [13, 23, 33, 34]. In the last few years, solid state processing routes such as mechanical alloying usually followed by consolidation through either hot/cold pressure [35] or spark plasma sintering [36, 37] gained ground on liquid state synthesis methods. Some attention to other techniques such as LENS (Laser Engineered Net Shaping) has also been paid for developing HEAs, particularly FeCoCrNi through additive manufacturing and the determination of some of its mechanical properties [22].

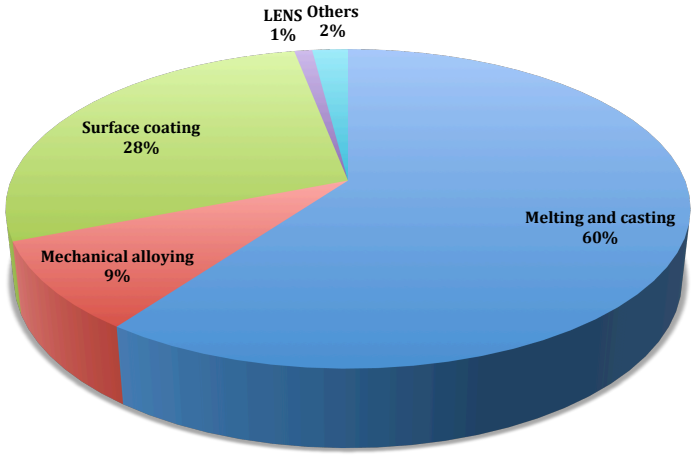

Fig. 2.7 Processing routes used for the synthesis of HEAs between 2004 and 2014.

The development of novel techniques to process material such as electron beam melting, produces a melt to solidify as fast that a deviation from equilibrium can happen, and metastable phases may therefore occur and besides, material properties may achieve a significant improvement. For example, Martensite is obtained in carbon steels by quenching of Austenite at such high rate that the carbon atoms do not have time enough to diffuse out of the crystal structure and form Cementite. As Martensite is not obtained through slow cooling, it is not a equilibrium phase. The basic procedure for the production of such phases (metastable phases) is to energise and then quench the material and can be done by several means [38].

In deed, nucleation and growth kinetics of the competing phases will determine whether the microstructure is composed of stable or metastable phases (i.e. metastable phase can nucleate before the stable phase can do it and the crystal growth rate of the metastable phase exceeds that of the stable phase) [39].

2.1.4 Formation and microstructures

As mentioned earlier, the characteristic that identifies HEAs the most is clearly their simplicity when forming single fcc/bcc crystalline solid solution phases rather than multiple phases, even though they are composed of multiple elements. Some of those simple systems are FeCoCrNi [40] , FeCoCrNiMn [19] forming a single simple fcc phase, NbMoTaW [41], TaNbHfZrTi [42] forming a single simple bcc phase and others forming a mixture of those simple phases such as FeCoCrNiCu forming two similar fcc phases [43], FeCoCrNiAl forming a mixture of bcc and fcc [2], or MoWAlCrTi forming two similar bcc phases [44]. Although their unexpected structural simplicity is the most relevant feature of HEAs, many systems in which the crystalline phase is composed of the simple phases bcc/fcc with addition of other phases such as Laves (i.e. CrMo0.5NbTa0.5TiZr forming two bcc phases and one laves phase [45]) are also reported under the name HEAs just because they are "alloys composed of multiple elements at near-equiatomic ratio".

For instance, the crystalline structure of the alloy system FeCoCrNiCu changes from fcc single phase to bcc single phase passing through a mixture of fcc and bcc when increasing the quantity of Al [2] whereas the amount of intermetallic phases such as Laves phase (intermetallic phases of the form AB_2 such as $NbCr_2$ and $NbFe_2$ [46]) increases if titanium or niobium is added into the system [12]. Although those alloy systems do not form single phases when increasing Al, Ti or Nb contents, they are still considered to be HEAs.

The single phase HEAs can achieve high mechanical properties when compared to conventional metallic systems, and therefore some authors focus their research on single phase HEAs [23, 42, 47]. However it is shown that structures consisting of single phases with the addition of a minor quantity of second phases such as intermetallic compounds have great potential as well [48].

If a homogeneous liquid is undercooled into the metastable inmiscibility gap (region in the phase diagram of a mixture of elements where the mixture exists as more than one phase), it would decompose into two liquids where liquid-phase microstructures can be obtained.

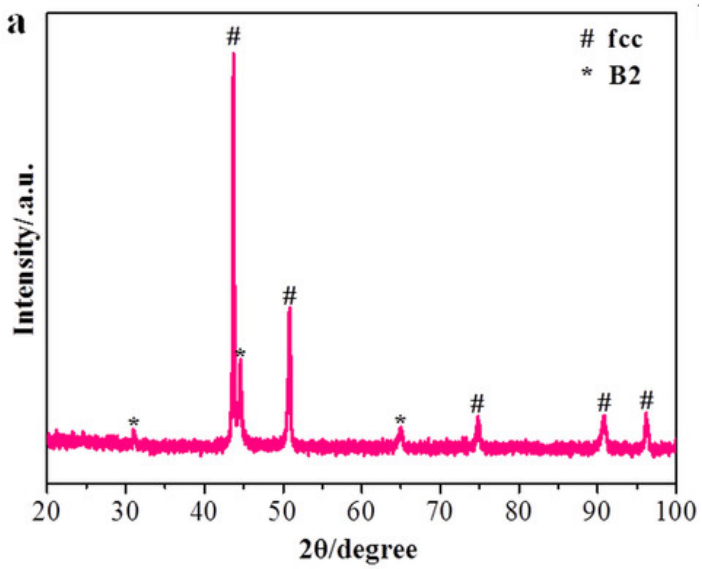

(a) x-ray trace

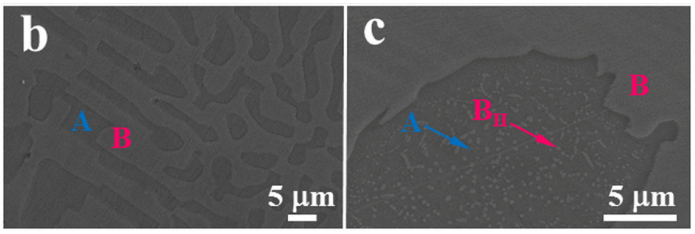

(b) SEM Images

Fig. 2.8 a) X-ray trace and b) high magnification microstructure of the HEA $AlCoCrFeNi_{2.1}$.

The effect of the cooling rate has already been observed in the known HEA composed of Fe, Co, Cr, Ni and Cu where a second Cu-rich phase was observed probably due to the effect of the the positive enthalpy of mixing of copper as well as the sluggish diffusion amount elements in the solid state [49].

2.1.5 Properties

Mechanical and wear resistance

HEAs have attracted a high degree of interest not only in the academic field but also in industry largely due to the structural and functional properties they can achieve. Focussing on the structural properties, Figure 2.9 represents two different Ashby charts plotting the property ranges of general materials classes, making reference to Young's Modulus against density (top figure) and strength against density (bottom figure), and Figure 2.10a represents the reported hardness of some HEAs in comparison with several commercial alloys. While HEAs cannot compete with composites or foams for high values of specific properties as shown by these charts, they do with some ceramics and the most resistant metals and alloys and their absolute strength is very high.

Corrosion

Corrosion resistance under certain environments has also been tested and compared with other conventional alloy systems [50]. As shown in Figure 2.11a and 2.11b the corrosion rates of several materials under 2 different environments have been compared with HEAs. The results make HEAs a competitive material for certain conditions as it reaches similar corrosion rate to most of the conventional systems.

Functional properties

Most of the research of HEAs has been focused on the analysis of their microstructures and mechanical response, whereas functional properties such as thermal, electrical and magnetic behaviour of HEAs has attracted only a small interest of the research community.

Chou et al. [51] studied the relationship between the crystalline structure and both the electrical and thermal conductivity of the HEA $Al_xFeCoCrNi$. It was observed that the addition of Al into the system increases the lattice distortion of the structure, and thus it affects the electrical and thermal conductivity.

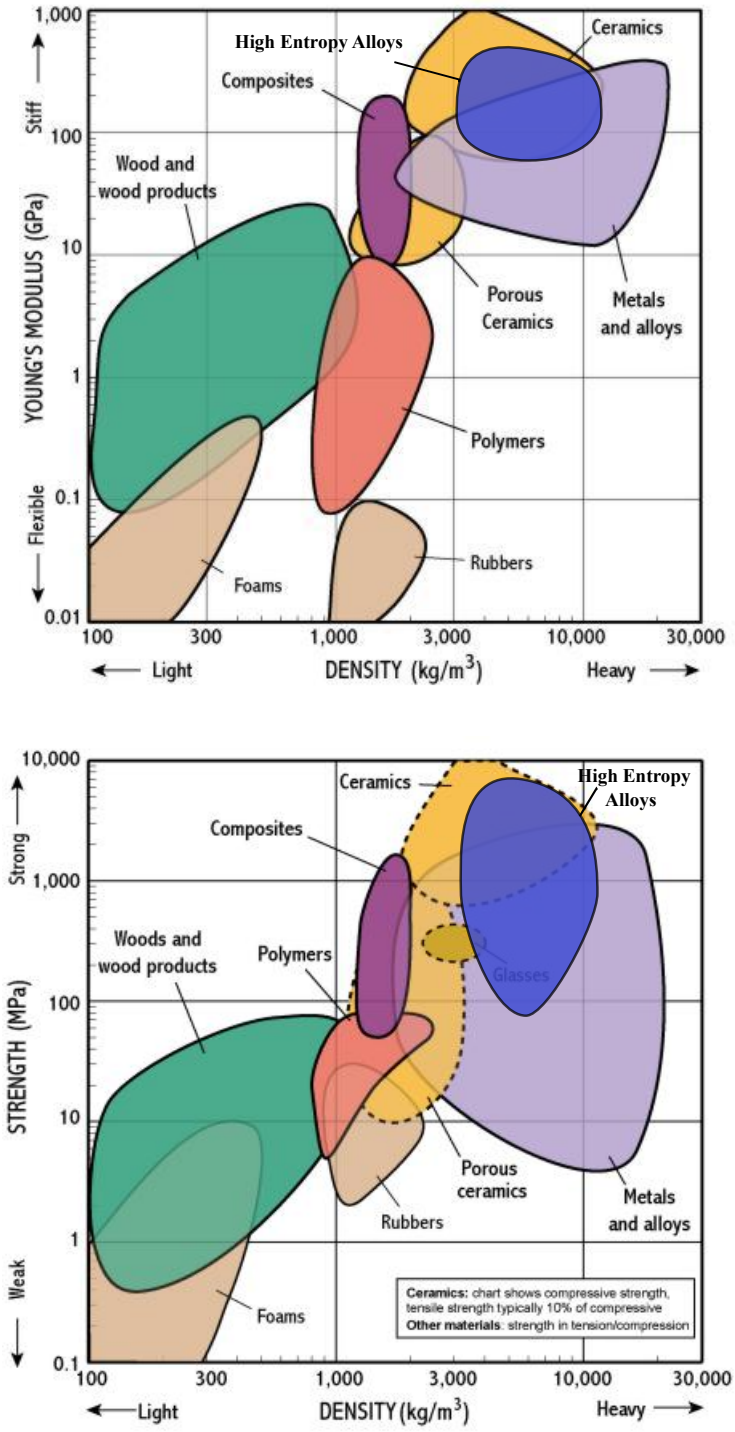

Fig. 2.9 Ashby charts showing the ranges of mechanical property of material classes including estimated position of the HEAs already reported. From top to bottom: Young's modulus against density, yield strength against density.

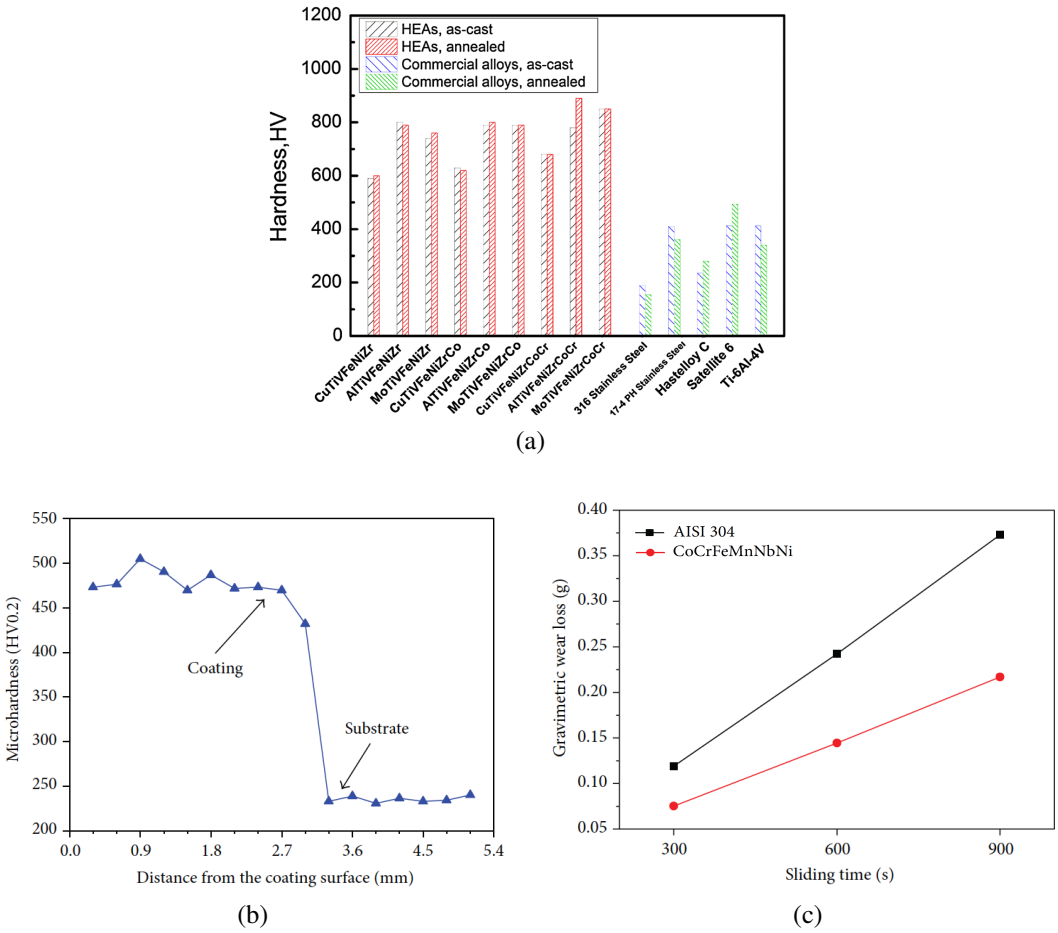

Fig. 2.10 (a) Hardness of the as-cast and fully annealed HEAs (at 1000 °C for 12 h) in comparison with that of several commercial alloys, (b) microhardness profile of CoCrFeMnNbNi coating, (c) mass losses of CoCrFeMnNbNi coating and substrate AISI 304 as a function of sliding time [8].

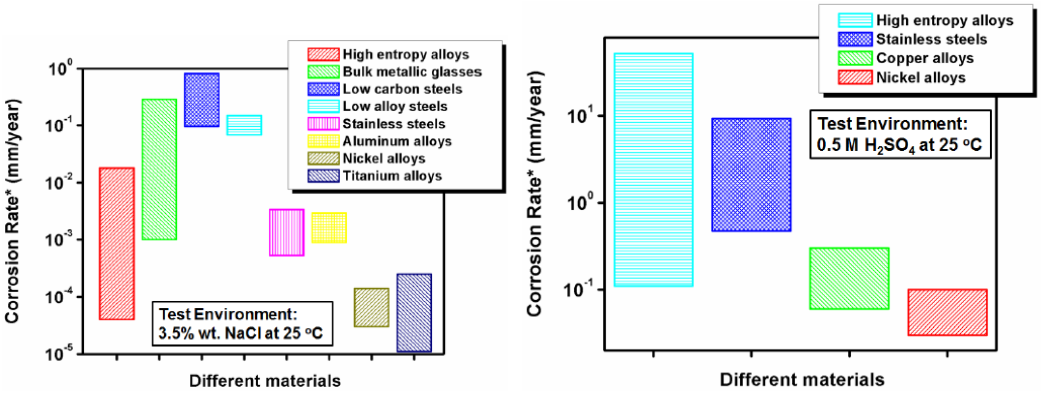

(a) (b)

Fig. 2.11 Corrosion rate of several type of materials (a) tested under 3.5%wt NaCl at 25 °C and (b) tested under 0.5M H_2SO_4 at 25 °C.

Table 2.1 contains the electrical resistivity and thermal conductivity of the HEA $FeCoCrNiAl_x$, which is compared with some common conventional alloys [13]. It is seen that the electrical resistivities of the multicomponent systems are of 1 or 2 orders higher than these of pure elements and conventional alloys. Thermal conductivity is smaller than the one of pure elements and similar to the one of some conventional alloys.

2.1.6 Potential applications

The combination of structural and functional properties achieved and the wide range of elemental combinations of High Entropy Alloys open a new era of exploitation for potential new alloy systems for use in applications in many industries such as aerospace, automotive, nuclear and medical. Some HEAs have already been proposed for a broad range of applications.

The excellent mechanical properties of FeCoCrNiMn achieved at low temperatures (77K) makes this alloy suitable for cryogenic applications such as those of hydrogen, oxygen and hydrocarbon storage [52]. Similar applications would be possible for ZrTiVCrFeNi [52] and $CoFeMnTi_xV_yZr_z$ [53]. AlMoNbSiTaTiVZr [34] and NbSiTaTiZr [54] appear to have potential use as effective diffusion barriers for copper metallization. $FeCoNi(AlSi)_x$ as a soft magnetic material [55].

Catergory	Composition	Electrical resistivity ($\mu\Omega - \text{cm}$)	Thermal conductivity (W/mK)
HEA	CoCrFeNi	142	12
	AlCoCrFeNi	221	11
	$\text{Al} - 2\text{CoCrFeNi}$	211	16
Pure Element	Al	3	237
	Fe	10	80
	Ni	7	91
	Ti	42	22
	Cu	2	398
Conventional Alloy	7075 Al alloy	6	121
	Low carbon steel	17	52
	304 Stainless Steel	69	15
	Inconel 718	125	11
	Ti-6Al-4V	168	6
BMG	$Zr_{41}Ti_{14}Cu_{12.5}Ni_{10}Be_{22.5}$	171	-
	$Fe_{72}Si_9F_{13}$	137	-
	$Co_{63}Fe_9Zr_8B_{20}$	188	-

Table 2.1 Electrical resistivity and thermal conductivity of the system $Al_xCoCrFeNi$, pure elements, some conventional alloys and Bulk Metallic Glasses (BMGs) [13].

2.2 Computational informatics

To make a combinatorial experimental strategy successful for materials discovery, prior data and knowledge needs to be built and use those data to associate and anticipate structure-property correlations before conduction further experiemnts.

The evolution of the combinatorial approach has offered the development of experimental procedures, which means that, nowadays, the bottleneck is often found in data management and data analysis [56].

Some strategies are already applied for dissolving this drawback and involve computational techniques such as (a) planning and selecting high-throughput experiments using Design of experiments, DOE; (b) Genetic algorithms, GA; (c) Artificial Neuronal Network, ANN; and (d) the extraction of knowledge out of large data sets using both statistical and mathematical tools for a complete interpretation of the data, as it is data-mining. Some of the important data-mining techniques used for knowledge discovery are Principal Component Analysis (PCA), clustering techniques, classification methods, regression, kernel methods, etc. Amount all these techniques, PCA has been used here for the interpretation and understanding of factors affecting the behaviour of HEAs.

2.2.1 Data mining: Principal Component Analysis

Here is included the basics of combinatorial and high throughput (HT) techniques, explaining the difference between them as well as a brief introduction to the data analysis techniques such as PCA (as the data mining step).

Traditional procedures used for the discovery of novel materials are based on the synthesis, characterization and testing of one sample at a time. The process begins by selecting one single composition, which goes through an iterative sequence of slight modifications after observing its properties until it achieves the right properties for a certain application. This trial and error technique could require 2 years for the discovery of the right material for a certain application, during which only around 100 samples of differing composition would be produced and tested.

Alternatively, an efficient route to discover, develop and optimize materials aiming at the reduction of consumption of time, money and human effort, a combinatorial approach would be suitable for this objective. Essentially, this technique would be able to synthesise, charac-

terise and test a huge set of different compositions (instead of one) at a time.

Although, combinatorial approaches were first proposed in the 70s [15], they began being exploited in the 90s for the discovery and improvement of drugs in the pharmaceutical industry. The success of this method should be gauged by the number of experiments carried out, the performance speed and efficiency (as well as, of course, the accuracy). Hence, when comparing with traditional approaches, where 2 years might be required for the production of 100 samples, a efficient combinatorial approach would be able to achieve this after a year [57].

A classic combinatorial workflow has been described by Fasolka and Amis [58], dividing the procedure in 4 steps: library design, library fabrication, measurements and analysis.

- The library design would determine the materials properties of interest and the portion of variable space to include into the combinatorial library. This step would be performed while using a design of experiments approach (DOE) extended to multivariate parameter spaces.
- Library fabrication includes the physical production of the designed material. This production stage should be completely or highly automated.
- Measurements are required in a high-throughput route that allows faster and more intelligent characterization of the library.
- Analysis includes scientific calculations and data handing in a faster manner, which could involve data-mining schemes and multivariate statistical treatment of the library data space for observing patters and correlations. It could include single values, spectra and images.

The most interesting contribution of the analysis stage is the visualization of a large dataset. Where large amounts of data are available, multivariate statistical analysis by techniques such as Principal Component Analysis (PCA), could be used as a feedback mechanism ready to close the combinatorial cycle. The PCA technique is used in this project, and therefore its basics will be explained.

Basic concepts of Principal Component Analysis

Principal Component Analysis, PCA is a multivariate technique the core of which is to reduce the dimensionality of a large data set of interrelated variables, while retaining as much as

possible of their variance [59].

A dataset composed of p variables can be defined as $x = (x_1, x_2, ..., x_p)$. When the correlations between a small amount of variables p are of interest, it is an easy task to analyse the correlation values obtained from the correlation matrix shown in equation 2.11. Those values will indicate whether the two variables:

- are perfectly correlated (correlation value equal 1)
- tend to increase or decrease together (values between 0 and 1)
- do not vary together at all (correlation equal 0)
- increases as the other one decreases (correlation values between -1 and 0)
- are perfectly negatively correlated (-1)

$$cov = \frac{\Sigma(x_i - \overline{x})(y_i - \overline{y})}{n-1} \tag{2.11}$$

However as the number of variables p increases, this task became much more tedious. In this case, PCA is an alternative technique that searches for only a few variables (< p) that preserve most of the information given by the p variances and correlations. Those new variables are called Principal Components (PCs).

The first step is to look for a lineal function $\alpha_1' x$ of the elements of x having maximum variance:

$$\alpha_1' x = \alpha_{11} x_1 + \alpha_{12} x_2 + ... + \alpha_{1p} x_p = \sum_{j=1}^{p} \alpha_{1j} x_j \tag{2.12}$$

where α_1 is a vector of constants $(\alpha_{11}, \alpha_{12}, ..., \alpha_{1p})$ and ' denotes the transpose.
The second step is to look for a linear function $\alpha_2' x$ uncorrelated with $\alpha_1 x$ having maximum variance and so on, then the kth step is to look for a linear function $\alpha_k' x$ having maximum variance uncorrelated with $\alpha_1' x$, $\alpha_2' x$,...and $\alpha_{k-1}' x$. The k values correspond to the principal components and the maximum possible value is p, however it is expected that a few principal components, m (where $m << p$) will preserve the maximum variance of x.

Mathematical description

To obtain the form of the PCs, $\alpha_1' x$ will determine the first PC where the vector α_1 maximizes the variance as $var[\alpha_1' x] = \alpha_1' \sum \alpha_1$ ($\sum$ is the covariance matrix) subject to the constraint

$\alpha_1'\alpha_1 = 1$, the problem can therefore be expressed as follows:

$$\begin{cases} \max & \alpha_1' \sum \alpha_1, \\ \text{subject to} & \alpha_1'\alpha_1 = 1 \end{cases} \tag{2.13}$$

Thus, the function to maximize can be calculated using the Lagrange multipliers

$$\alpha_1' \sum \alpha_1 - \lambda(\alpha_1'\alpha_1 - 1) \tag{2.14}$$

where λ is a Lagrange multiplier. The maximum is obtained through differentiation with respect to α_1, solution of which is given by

$$\frac{\delta}{\delta\alpha_1} = 0 = \sum \alpha_1 - \lambda\alpha_1 \tag{2.15}$$

$$(\sum -\lambda I_p)\alpha_1 = 0 \tag{2.16}$$

where λ is the eigenvalue and α_1 its corresponding eigenvector of $\sum$, and $\mathrm{I_p}$ is the identity matrix with p-dimensionality. As the vector α_1 cannot give a null result, the determinant of $(\sum -\lambda \mathrm{I_p})\alpha_1$ must be zero.

To decide which of the p eigenvectors gives $\alpha_1'\mathrm{x}$ with maximum variance, the value to maximize corresponds to λ as shown below:

$$\sum \alpha_1 - \lambda\alpha_1 = 0 \tag{2.17}$$

$$\alpha_1' \sum \alpha_1 = \alpha_1'\lambda\alpha_1 = \lambda, \tag{2.18}$$

which means that λ must be as large as possible; therefore α_1 is obviously the eigenvector corresponding to the largest eigenvalue of $\sum$ and $var(\alpha_1'\mathrm{x}) = \alpha_1' \sum \alpha_1 = \lambda_1$.

The second PC, $\alpha_2'\mathrm{x}$ must reach maximum variance $var[\alpha_2'\mathrm{x}] = \alpha_2' \sum \alpha_2$ subject to be uncorrelated with the first PC, $\alpha_1'\mathrm{x}$ and be of a unit length:

$$\begin{cases} \max & \alpha_2' \sum \alpha_2, \\ \text{subject to} & \alpha_2'\alpha_2 = 1 \\ & cov[\alpha_1'x, \alpha_2'x] = 0 \end{cases} \tag{2.19}$$

The uncorrelated value between the first and the second PC is expressed as $cov[\alpha_1'\mathrm{x}, \alpha_2'\mathrm{x}]$ and results as follows:

$$\mathrm{cov}[\alpha_1'\mathrm{x}, \alpha_2'\mathrm{x}] = \alpha_2' \sum \alpha_1 = \alpha_1' \sum \alpha_2 = \alpha_2' \lambda \alpha_1' = \lambda_1 \alpha_2' \alpha_1 = \lambda_1 \alpha_1' \alpha_2 \tag{2.20}$$

Thus, using any of the constraints shown above, the function to maximize can be derived from equation 2.22, using the Lagrange multipliers, λ and ϕ, as shown in equation 2.23.

Multiplying equation 2.23 by α_1' results on equation 2.24. Looking at that equation, as the first two terms of equation 2.24 are equal zero and the constraint $\alpha_1'\alpha_1$ preserve the unit length, the second Lagrange multiplier, ϕ becomes zero. Consequently, the calculation of the eigenvalue and eigenvector of the second PC is carried out through

$$(\sum -\lambda I_p)\alpha_2 = 0 \tag{2.21}$$

where the maximum variance $\mathrm{var}[\alpha_2'\mathrm{x}]$ is λ and α_2 is the corresponding eigenvector.

$$\alpha_2' \sum \alpha_2 - \lambda(\alpha_2'\alpha_2 - 1) - \phi(\alpha_2'\alpha_1) \tag{2.22}$$

$$\frac{\delta}{\delta \alpha_2} = 0 = \sum \alpha_2 - \lambda \alpha_2 - \phi \alpha_1 \tag{2.23}$$

$$\alpha_1' \sum \alpha_2 - \alpha_1' \lambda \alpha_2 - \alpha_1' \phi \alpha_1 \tag{2.24}$$

The calculation of the following PCs (3, 4, ...,k) is performed under the same basis, where the maximum variance of the kth PC, $var[\alpha_\mathrm{k}'\mathrm{x}]$ corresponds to λ_k and α_k is kth eigenvector.

Finally, graphical techniques such as biplots can also be used to interpret the relationship between variables and observations and variables themselves. A biplots is a graphical display of the "observations" as points and the variables as "vectors" in a low-dimensional space, usually of dimensionality two or three. The biplot is constructed by using Singular Value Decomposition (SVD) as first described by Gabriel K.R. [60].

Nowadays, there are several commercial software such as OriginLab, MatLab and MiniTab amongst others that already allow multivariate statistical analysis of a large amount of data where PCA can easily be performed.

In order to make it easier to understand, an example of the methodology applied for the calculation of eigenvalues and eigenvectors of the covariance matrix is shown below. It needs to be mentioned here that, although PCA is useful when the number of variables is large, the example shown corresponds to a simple case of a dataset composed of 2 variables to give a simpler and clearer demonstration.

The objective of the following example is to show how to obtain the eigenvalues and eigenvectors of a covariance matrix.

First of all, the original dataset containing the observations of 2 variables is selected as the one shown in Table 2.2. It contains 10 observations of the variables x_1 and x_2. The corresponding plot of these observation is shown in Figure 2.12a where the variablility of the data is observed to be higher on x_2 than on x_1, but still present in both variables. Firstly,

x_1	x_2
0.3	0.2
0.3	0.4
0.4	0.6
0.5	0.5
0.4	0.9
0.3	1.2
0.5	1.3
0.7	1.3
0.6	1.5
0.7	1.6

Table 2.2 Original dataset containing 10 observations of 2 different variables.

the covariance matrix $cov(\mathrm{x_1}, \mathrm{x_2})$ is calculated from Equation 2.25, where $\overline{\mathrm{x_i}}$ is the mean. As $cov(\mathrm{X}, \mathrm{Y}) = cov(\mathrm{Y}, \mathrm{X})$, the obtained matrix will be symmetric, which structure corresponds to the one shown in the matrix 2.2.1)

$$cov(x_1, x_2) = \frac{\sum_{i=1}^{n}(x_{1i} - \overline{x_1})(x_{2i} - \overline{x_2})}{(n-1)} \tag{2.25}$$

$$\sum = \begin{bmatrix} cov(x_1, x_1) & cov(x_1, x_2) \\ cov(x_2, x_1) & cov(x_2, x_2) \end{bmatrix}$$

$$\sum = \begin{bmatrix} 0.0246 & 0.0561 \\ 0.0561 & 0.2472 \end{bmatrix}$$

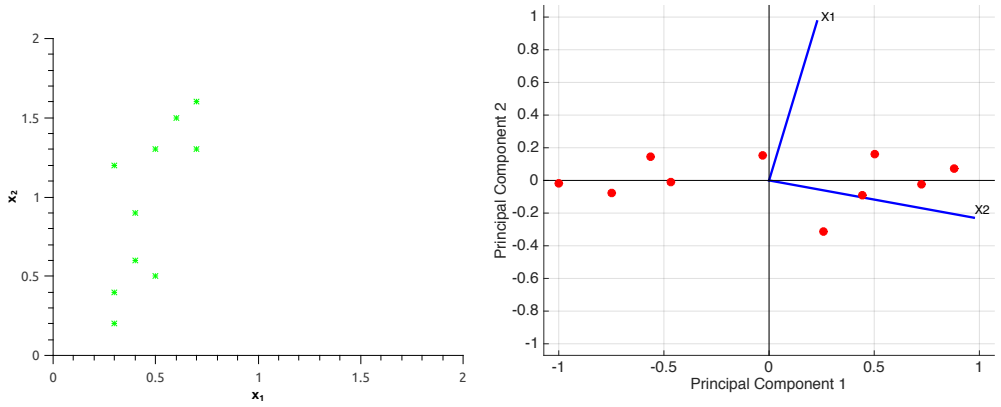

(a) (b)

Fig. 2.12 (a) Plot of the 10 observation x_1 against x_2 and (b) biplot containing scores representing the observations and the vectors representing the variables x_1 and x_2 according to PC1 and PC2.

Secondly, the eigenvalues and then eigenvectors of the covariance matrix must be found using Equation 2.16. The solution of this problem returns two eigenvalues and their corresponding eigenvectors as shown in the vectors below, where the diagonal matrix contains both of the eigenvalues and the columns of the following matrix are the corresponding eigenvectors.

$$Eigenvalues = \begin{bmatrix} 0.0112 & 0 \\ 0 & 0.2606 \end{bmatrix}$$

$$Eigenvectors = \begin{bmatrix} -0.9729 & 0.2313 \\ 0.2313 & 0.9729 \end{bmatrix}$$

Finally, the PCs need to be defined; as the variance of the first PC must be the largest one, and the variance of the kth PC is the same as kth eigenvalue, the first PC corresponds therefore to the one at higher eigenvalue. Table 2.3 includes the corresponding eigenvalues and eigenvectors of each PC. It also shows the total amount of information of the original dataset is retained by each PC. In this example, PC1 retains more than 95% of the variance (also seen in Figure 2.12a), which means that 1 PC would be considered to be enough to represent the original dataset.

Here, it needs to be clarified that the full potential of Principal Component Analysis as a mathematical tool cannot be easily appreciated with a 2 dimensional example, however, it helps in the understanding of its basics.

	PC1	PC2
Eigenvector	0.2313	-0.9729
	0.9729	0.2313
Eigenvalues	0.2606	0.0112
% Variance	95.88	4.13
Cumulative variance	95.88	100

Table 2.3 Eigenvectors and eigenvalues of the PCs showing the % variance of the original information retained.

2.3 Processing techniques for advanced materials

The discovery of novel materials implies the evolution of the manufacturing routes, and to fully explore the possibilities for high throughput fabrication, all possible techniques should be considered. This section will cover three particular techniques used for processing advanced materials in this project.

2.3.1 Vacuum Arc melting

Vacuum arc melting is a process for the production of metal ingots with high chemical and mechanical homogeneity. The ingot (mainly made of Ni, Ti , Fe superalloys) is typically used for parts of jet engines and gas turbine due to the demanded properties.

Figure 2.13 shows an schematic of the arc melting furnace. The heat of a direct current electric arc melts the metal into the water cooled copper crucible, where solidification of the metal part takes places at the end of the process. The electrode is moved down to maintain constant arc length during melting and the electric arc is maintained by a DC powder supply connected to the electrode and the crucible. The torch can reach temperatures above 3000 °C and is controlled by adjusting the electrical powder.

Some of the features of this technique are the removal of non-metallic inclusions and dissolved gases, high density with desirable grain structure and low macrosegregation. The high temperature and vacuum environment provide favourable conditions for removal of entrapped gases and high vapour pressure elements. High temperature within the electric arc produce the separation of the non-metallic and high melting temperature inclusions into smaller parts. The typical grain structure of parts produced by arc melting consist of columnar for small diameter parts or a mixture of columnar and equiaxed grains for larger parts.

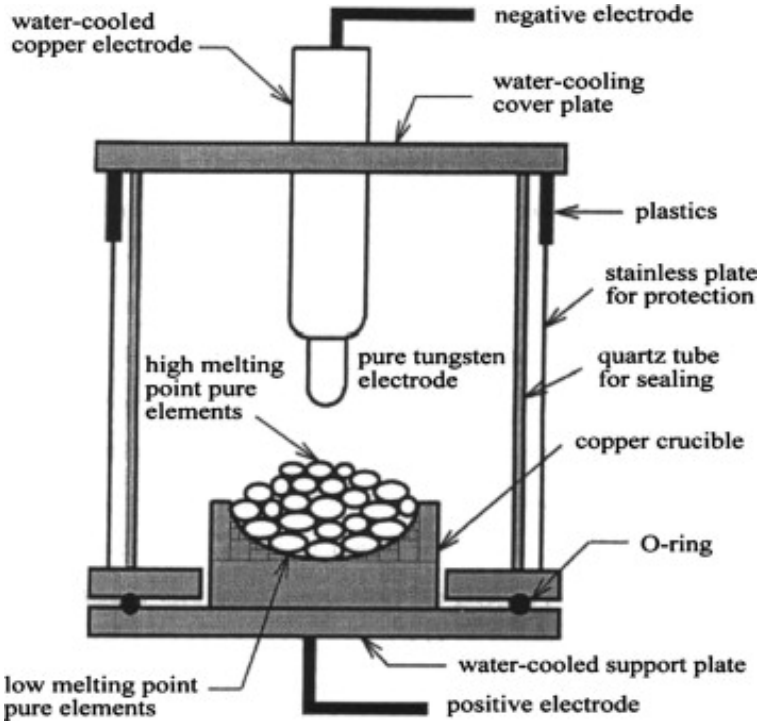

Fig. 2.13 Schematic of the arc melting furnace [9].

The technique becomes useful when processing elements with high melting point, however, for those elements with low melting point (easy to evaporate) such as Mg, Zn, Mn, this technique cannot control the composition and therefore it may not be the best synthesis choice. Nevertheless, as most elements can be mixed in their liquid state in this type of furnace, arc melting becomes the most popular liquid processing technique used for the synthesis of HEAs. Alternatively, for low melting point elements, heating or induction heating could be more appropriate. On the other hand, from the fabrication point of view, arc melting is not the best choice due to the limitation in shape and size of the final part and the manufacturing cost. Hence, powder metallurgy would be a more convenient route to ease the mentioned limitations.

2.3.2 Spark Plasma Sintering

Electrical current can be used as a method for activating the sintering process of a material. Spark Plasma Sintering -also known from the initials as SPS- is a solid state sintering tech-

nique which sinters powder under the simultaneous influence of pressure and an electrical current. This technique is also known as Plasma Assisted Sintering (PAS), Pulsed Electric Current Sintering (PECS) and Electric Pulse Assisted Consolidation (EPAC). Figure 2.14 shows a schematic of an SPS chamber where a powder (metallic or ceramic) is loaded into a graphite die; then, a uniaxial pressure is applied to the sample while an electrical DC current passes through the sample (if conductive), die and punches, heating the sample and producing the sintering.

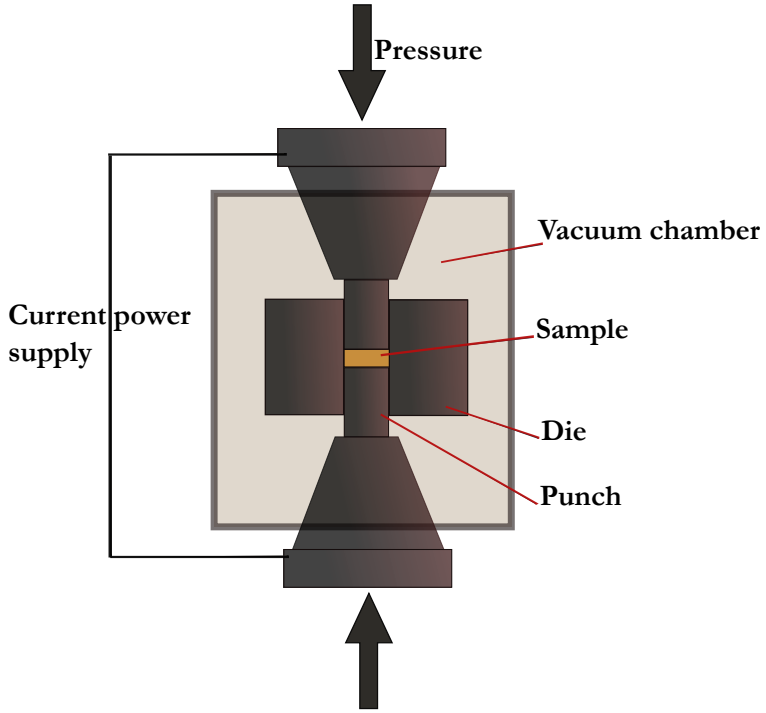

Fig. 2.14 Schematic of an SPS chamber.

SPS offers some advantages over conventional methods such as pressureless sintering and hot pressing as lower sintering temperature and shorter dwell times are required, and for obtaining improved properties of the material. The characteristics of the SPS method include (1) Application of a pressure, (2) High heating rate and (3) Effect of a current; the general effects on the material have already been studied [10].

(1) Effect of applied pressure A sample can reach higher density values when pressure is applied than when it is not, even though the temperature remains constant. Mechanically,

the pressure applied has a direct contribution to the particle re-arrangement and also the destruction of agglomerates.

The equation of the driving force for sintering can be expressed as

$$\frac{1}{(1-\rho)}\frac{\delta \mathrm{P}}{\delta \mathrm{t}} = \mathrm{B}(\mathrm{g}\frac{\gamma}{\mathrm{x}} + \mathrm{P}) \tag{2.26}$$

where ρ is the density of the material, B is a function dependant on the diffusivity and temperature, g is a geometric constant, γ is the surface energy, x is related to the particle size, t is the time and P is the pressure applied. The pressure applied to small particle sizes does not have a considerable effect on the density of the sample, however, it does when the pressure increased. This effect can be determined with the second term of Equation 2.26 when the two contributions are equal, as shown in Equation 2.27.

$$\mathrm{P} = \mathrm{g}\frac{\gamma}{\mathrm{x}} \tag{2.27}$$

An example of the intrinsic effect of the driving force for sintering can be observed in Figure 2.15, which shows the effect of the pressure applied on the grain size and temperature of a Zr_2O sample which is intented to have 95 % relative density.

As would be expected, as the pressure increases, the temperature required to achieve the same density decreases and the effect of the pressure on the grain size is reduced as it increases.

The effect of the pressure upon the density and the grain size when the same temperature is applied can be observed in Figure 2.16. In this case, the pressure does not show any effect on the grain size but only on the density.

(2) Effect of heating rate It has been observed that higher heating rates can be reached when no pressure is applied [10]. The effect of the heating rate on the densification and grain size of the material has also been studied by [61–63]. It was shown that as heating rate increases, the final density of the material is either slightly decreased [61] or is unaffected [62]. It has however a significant inverse effect on the grain size of the samples [63]. These effects could be due to a high thermal gradient existing with high heating rates, as the sample is sintered outside but contains a high level of porosity inside.

(3) Effect of the current The important aspect of the current is the pulsing and the creation of a plasma, although the existence and effect of the latter remains unclear. Studies have been

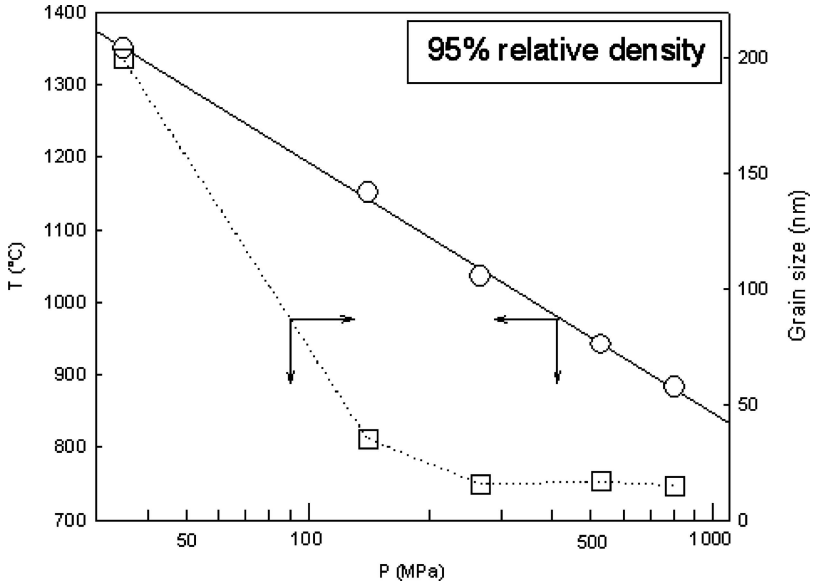

Fig. 2.15 The effect of the pressure on the temperature required to obtain 95% relative density for cubic ZrO_2 and the evolution of the grain size [10].

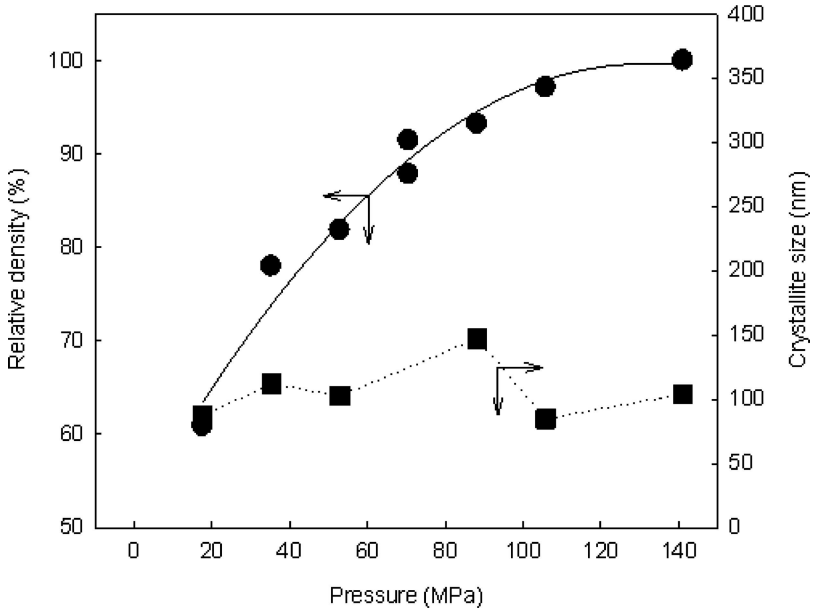

Fig. 2.16 The effect of the pressure on the density and the grain size of ZrO_2 at 1200 °C with 5min dwell time and heating rate of 200 °C/min [10].

carried out on aluminium samples where it has been observed that either with or without a pulse frequency, no effect on density, electrical resistivity and tensile properties of the material is found.

2.3.3 Electron Beam Melting

Electron Beam Melding (EBM) is a thermal processing technique that modifies shape and properties of a solid material by using an electron beam as a heat source. It consists on the projection of energetic electrons onto a solid material where some of them are reflected from the surface by elastic or inelastic collisions, while most of the electrons are absorbed by the solid material reducing their kinetic energy and consequently heating the material [64, 65].

The technique offers some advantages over other conventional welding techniques: (1) It is a chemically pure process due to the use of a vacuum environment to transfer electrons from a emitting cathode to the receiving solid material, and the fact that the electrons themselves are chemically inert; (2) The wide range of power allows the same equipment to melt a 50mm steel plate and a sheet of 0.1μm with no modification; (3) The magnitude of heating in the irradiated material can be controlled through the power density, where the beam power can be spread over an area or focused to a fine spot with power densities varying from $0.1\mathrm{W/mm^2}$ to $10^7\mathrm{W/mm^2}$; (4) There is a small amount of energy loss due to the emission of secondary electrons and the generation of x-ray, however the rest of the energy is expended in heating the workpiece making this process a highly efficient one; (5) The is a rapid thermal response due to (a) the speed of the electron (which is of the same order of magnitude as the speed of light in the range of accelerating voltages of interest) and (b) the heating, which is due to the interaction of the electrons with the solid matter, and takes place in a period of microseconds.

Besides those beneficial features there are other undesirable ones that need to be mentioned such as (1) the requirement of high vacuum for transporting the electrons and a large capacity power supply which compose most of the capital cost of the plant; (2) when electrons are projected into the workpiece, some of them are reflected as x-rays, causing hazardous; (3) a magnetic field within the vacuum chamber may deflect the beam from its normal path.

Theory of moving heating sources Numerical modelling can be used for estimating the conditions under which welding process takes place. Several models for the description of the thermal conditions and heat flow for a moving heat source have been developed and used

for prediction of welding processing. As an example is the Rosenthal solution to a moving heat source, which describes the temperature field for a point source moving on the surface of a semi-infinite plate:

$$T(x,y,z) = T_0 + \frac{q}{2\pi\kappa\sqrt{x^2+y^2+z^2}}\exp\{-\frac{v}{2\alpha}(x+\sqrt{x^2+y^2+z^2})\} \tag{2.28}$$

where T_0 and q are the temperature and power at which the welding takes place respectively; κ and α are properties of the material: conductivity and diffusivity respectively; x is the welding direction in which the beam moves at the speed v. Figure 2.17 shows a schematic diagram of the welding of a workpiece with an electron beam with direction of the welding along OX, the width and penetration of the electron beam are along OY and OZ respectively. Some authors have already used this solution for the prediction of welding parameters [22]

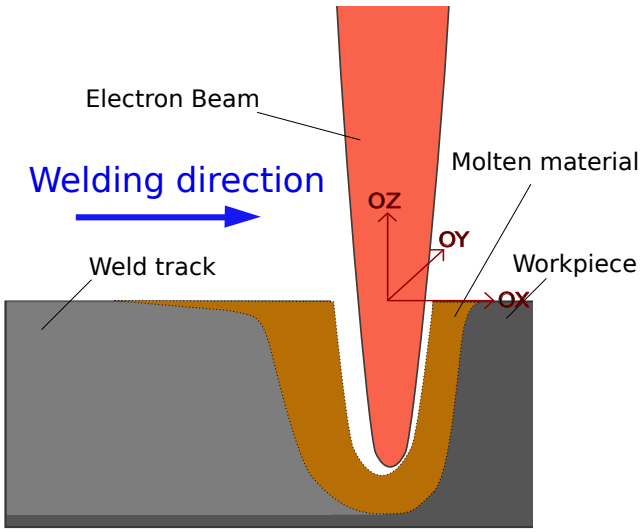

Fig. 2.17 Schematic of the melting process of a workpiece using an electron beam.

[66], while others have correlated some of them [11, 67].

Schwarz et al. [67] showed how the beam power and its travel speed affect the penetration and porosity of the materials after welding. It was observed that the porosity of the material increased with the power applied and with decreasing speed. On the other hand, the greatest effect on the penetration depth was observed with travel speed as shown in Figure 2.18.

Giedt et al. [11] correlated the operational and material properties. A possible universal trend was found as in the plot shown in Figure 2.19 which includes the relationship between certain

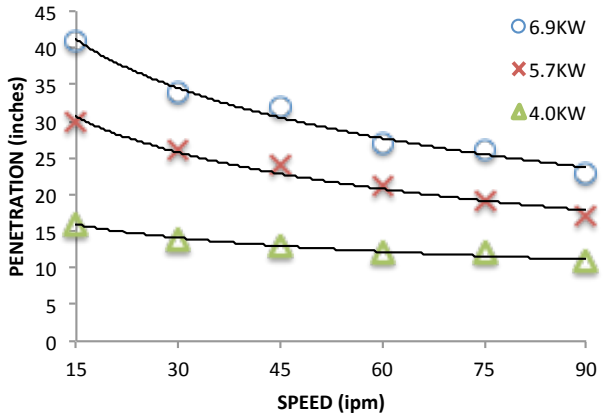

Fig. 2.18 The effect of the speed and power of an electron beam on the maximum penetration during melting [11].

operational and material parameters for several materials. Using this plot, the relationship between depth and width of the weld can be obtained as shown in Equation 2.29. It can be observed that penetration increases when increasing the power applied or the thermal diffusivity of the material and decreases with travel speed, thermal conductivity or difference in temperature.

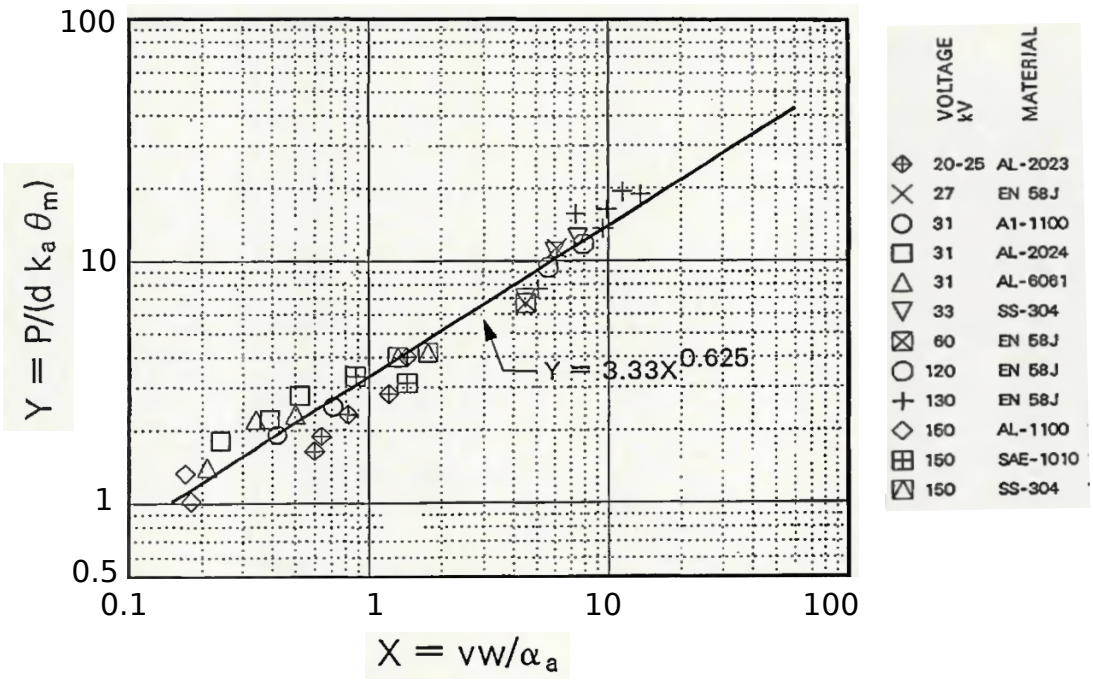

Fig. 2.19 Comparison of measured with predicted values of the electron beam penetration [11].

$$\text{penetrationD} = \frac{Q * \alpha^{0.625}}{3.33\kappa\theta_m \nu^{0}.625}(\frac{1}{\text{width}})^{0.625} \tag{2.29}$$

Evaporation phenomenon When deep weld tracks are required, the boiling temperature of the material can be reached in the centre of the molten pool and evaporation can therefore occur. This is one of the reasons why a hole in the weld track can be formed: (1) Removal of metal by evaporation. This effect could be determined by the calculation of the evaporation rate at the temperature achieved at the centre of the molten pool. (2) Pressure produced by the impact of the stream of electrons on the molten material. Electrons reach the workpiece which is a function of some of the processing conditions as shown in Equation 2.30

$$p_e = I\sqrt{\frac{2Vm_e}{e}} \tag{2.30}$$

where I is the current of the electron beam, V is the acceleration voltage, m_e is the mass of an electron and e is the electron charge. For this pressure to cause a hole, the curvature ratio shown in Equation 2.31, where γ is the surface tension, should be similar to the beam diameter.

$$r_c = \frac{2\gamma}{p_e} \tag{2.31}$$

(3) Internal pressure of the metal vapour. If the vapour pressure reached at the centre of the molten pool is as high as that the curvature ratio at a size similar to the beam diameter, the vapour pressure will be sufficient to cause the generation of the hole.

Internal welding stress Internal welding stress generated during heating and cooling can remain at room temperature. It is the main cause of workpiece distortion, the magnitude of which depends on the welding processing parameters, the shape of the weld track, structural factors such as the geometry and stiffness of the workpiece and material factors such as thermal expansion, metallurgical behaviour, yield point, etc.

Welding of dissimilar materials The weldability of dissimilar materials depends not only on their physical properties but also in the chemical affinity between those elements being welded together which can cause the undesired formation of brittle intermetallic compounds. The weldability of certain transition metals can be predicted when rearranging them into different groups [65]; Table 2.4 shows the transition elements arranged in two different groups, A and B. Elements included in group A or B are considered suitable to weld with

any of the elements included in the same group. However, when trying to weld an element of group A with another one outside of its group, intermetallics are more likely to form.

Group A

25 Mn	43 Tc	75 Re	93 Np
26 Fe	44 Ru	76 Os	94 Pu
27 Co	45 Rh	77 Ir	95 Am
28 Ni	46 Pd	78 Pt	96 Cm
29 Cu	47 Ag	79 Au	97 Bk

Group B

22 Ti	40 Zr	72 Hf	90 Th
23 V	41 Nb	73 Ta	91 Pa
24 Cr	42Mo	74 W	92 U

Table 2.4 Arrangement of transition metals according to their capability of being melted together.

Chapter 3

Experimental Techniques

3.1 Introduction

This chapter will go through the experimental techniques required for this research project. The techniques are divided into 3 groups: (1) Design and Prediction, (2) Processing and (3) Characterization and testing. The first group describes the algorithms used for the design and prediction of the crystalline structures of High Entropy Alloys (HEAs) by Principal Component Analysis (PCA) as well as the prediction of the penetration of the electron beam using the Rosenthal solution of the heat equation in 3D. The second group goes through the processing techniques Spark Plasma Sintering (SPS) and Electron Beam Melting (EBM) and the explanation of the alternative protocol to follow, developed for high-throughput. Finally, the preparation procedures, characterization of the produced samples and the testing techniques applied are explained in the third group.

3.2 Design and prediction techniques

Calculation of thermodynamic and electronic parameters of Multicomponent High Entropy Alloys

The prediction of HEAs used here is based on thermodynamic and electronic parameters such as enthalpy of mixing ΔH_{mix}, entropy of mixing ΔS_{mix}, atomic size difference δ, valence electron concentration VEC and electronegativity difference $\Delta\chi$. A Matlab macro has been created to allow systematic calculation of the thermodynamic and electronic parameters introduced above. The macro allows the user to choose the elements added into the system as well as determining their quantity. Its output contains the theoretical values of certain

parameters of the desired metallic system. The output includes the following parameters: the density, ρ and the melting temperature, T_m, both obtained from the rule of mixing; the critical temperature, T_c; the ratio between critical and melting temperature defined as Ω; the enthalpy of mixing, ΔH_{mix}; the entropy of mixing, ΔS_{mix}; the atomic size difference, δ; the valence electron concentration, VEC; the electronegativity, $\Delta\chi$ and the atomic weight, A_w. A copy of the macro created in Matlab has been included into Appendix A.

Performance of Principal Component Analysis

A multivariate analysis, based on Principal Component Analysis (PCA), has been performed using Matlab. The dataset used includes a combination of 79 alloy systems collected from those in the literature in Table 3.2. These alloy systems have been reported as showing single phase bcc, single phase fcc, a mixture of multiple bcc and/or fcc phases and multiple phases including intermetallic compounds (for use here the reported phases are used; data from the literature is not reanalysed). Five thermodynamic and electronic parameters have been used as the variables, which comprise the enthalpy of mixing, ΔH_{mix} (equation 2.4); the entropy of mixing, ΔS_{mix} (equation 2.2); the atomic size mismatch, δ (equation 2.5); the electronegativity difference, $\Delta\chi$ (equation2.6) and the Valence Electron Concentration, VEC (equation 2.7).

Reference	System	Structure	ΔH_{mix}	ΔS_{mix}	δ	VEC	$\Delta\chi$
[55]	Al0.1Si0.1FeCoNi	fcc	-7.69	10.87	2.95	8.66	0.06
[51]	Al0.25CrFeCoNi	fcc	-12.32	13.38	5.78	7.20	0.12
[55]	Al0.2Si0.2FeCoNi	fcc	-12.72	11.75	4.02	8.35	0.07
[68]	Al0.2TiVNbTa	bcc	-3.99	12.57	3.85	4.67	0.05
[2]	Al0.3CrFeCoNiCu	fcc	0.16	14.43	3.42	8.47	0.10
[55]	Al0.3Si0.3FeCoNi	fcc+bcc	-16.73	12.32	4.76	8.08	0.08
[55]	Al0.4Si0.4FeCoNi	fcc+bcc	-16.73	12.32	4.76	8.08	0.08
[51]	Al0.5CrFeCoNi	fcc +bcc	-9.09	13.15	4.60	7.67	0.11
[2]	Al0.5CrFeCoNiCu	fcc	-1.52	14.70	4.17	8.27	0.11
[55]	Al0.5Si0.5FeCoNi	bcc	-22.56	12.97	5.78	7.63	0.09
[69]	Al0.5TiCrFeCoNi	bcc+fcc+CoTi2+FeTi	-19.57	14.70	7.04	7.00	0.14
[68]	Al0.5TiVNbTa	bcc	-8.40	13.15	3.74	4.56	0.05
[51]	Al0.75CrFeCoNi	fcc+bcc	-10.90	13.33	5.30	7.42	0.12
[2]	Al0.8CrFeCoNiCu	fcc+bcc	-3.61	14.87	4.92	8.00	0.12
[55]	Al0.8Si0.8FeCoNi	bcc	-27.82	13.33	6.76	7.09	0.11
[2]	Al1.3CrFeCoNiCu	fcc+bcc	-6.24	14.85	5.69	7.60	0.12

[2]	Al1.5CrFeCoNiCu	fcc+bcc	-7.05	14.78	5.89	7.46	0.12
[69]	Al1.5TiCrFeCoNi	bcc+bcc	-22.72	14.78	7.29	6.38	0.14
[2]	Al1.8CrFeCoNiCu	fcc+bcc	-8.08	14.64	6.13	7.26	0.13
[2]	AlCrFeCoNiCu	fcc+bcc	-4.78	14.90	5.28	7.83	0.12
[69]	AlTiCrFeCoNi	bcc+fcc+compounds	-21.56	14.90	7.22	6.67	0.14
[2]	Al2.3CrFeCoNiCu	fcc+bcc	-9.38	14.35	6.40	6.97	0.13
[2]	Al2.5CrFeCoNiCu	fcc+bcc	-9.78	14.21	6.48	6.87	0.13
[2]	Al2.8CrFeCoNiCu	bcc	-10.28	14.01	6.57	6.72	0.13
[69]	Al2TiCrFeCoNi	bcc+bcc	-23.35	14.53	7.30	6.14	0.14
[70]	Al2TiVCrMnFeCoNiCu	bcc	-15.44	17.99	6.27	6.60	0.14
[2]	Al3CrFeCoNiCu	bcc	-10.56	13.86	6.61	6.63	0.13
[71]	AlCrFeCoNi	bcc	-12.32	13.38	5.78	7.20	0.12
[9]	AlCrFeCoNiCu0.25	bcc	-9.94	14.34	5.64	7.38	0.12
[72]	AlCrFeCoNiMo0.1	bcc	-12.13	13.92	5.78	7.18	0.13
[72]	AlCrFeCoNiMo0.2	bcc+α	-11.95	14.22	5.77	7.15	0.14
[72]	AlCrFeCoNiMo0.3	bcc+α	-11.78	14.43	5.77	7.13	0.15
[72]	AlCrFeCoNiMo0.4	bcc+α	-11.60	14.59	5.76	7.11	0.15
[72]	AlCrFeCoNiMo0.5	bcc+α	-11.44	14.70	5.76	7.09	0.16
[69]	AlCrFeCoNiNb0.1	bcc	-13.32	13.92	5.92	7.16	0.12
[69]	AlCrFeCoNiNb0.25	bcc+Laves	-14.66	14.34	6.10	7.10	0.12
[69]	AlCrFeCoNiNb0.5	bcc+Laves	-16.53	14.70	6.33	7.00	0.13
[69]	AlCrFeCoNiNb0.75	bcc+Laves	-18.03	14.85	6.50	6.91	0.13
[9]	AlCrFeNiCu	fcc+bcc	-4.00	13.38	5.63	7.60	0.12
[73]	AlSiCrFeCoNiCu	fcc+bcc	-18.86	16.18	6.13	7.29	0.12
[23]	AlSiTiCr6FeCoNi	bcc	-21.22	13.21	6.56	7.00	0.11
[70]	AlTi0.5CrFeCoNi	bcc	-17.92	14.70	6.72	6.91	0.13
[70]	AlTi1.5CrFeCoNi	bcc+Laves	-23.91	14.78	7.50	6.46	0.15
[70]	AlTiCrFeCoNi	bcc+bcc	-21.56	14.90	7.22	6.67	0.14
[74]	AlTiCoNiCuZn	fcc+bcc	-20.56	14.90	6.91	7.33	0.14
[70]	AlTiVCrMnFeCoNiCu	bcc+fcc	-12.74	18.27	6.03	7.00	0.15
[4]	AlTiVNbTa	bcc	-13.44	13.38	3.57	4.40	0.05
[9]	AlTiVYZr	Compounds	-14.88	13.38	10.95	3.80	0.16
[9]	CoNiCuZn	fcc	-0.75	11.53	4.67	10.50	0.11
[43]	CrFeCoNi	fcc	-3.75	11.53	0.29	8.25	0.096
[43]	CrFeCoNiCu	fcc+cu-rich fcc	3.20	13.38	1.03	8.80	0.09
[43]	CrFeCoNiCu0.5	fcc	0.49	13.15	0.84	8.56	0.09

[13]	CrFeCoNiPd	fcc	-5.60	13.38	4.04	8.60	0.17
[75]	CrFeNiCuMo	fcc+fcc+bcc	4.64	13.38	3.58	8.20	0.16
[75]	CrFeNiCuZr	bcc+compounds	-14.40	13.38	10.61	7.80	0.22
[19]	CrMnFeCoNi	fcc	-4.16	13.38	3.27	8.00	0.14
[19]	CrMnFeCoNiCu	fcc+bcc	1.44	14.90	3.00	8.50	0.14
[55]	FeCoNi	fcc	-1.33	9.13	0.33	9.00	0.03
[41]	NbMoTaW	bcc	-6.50	11.53	2.31	5.50	0.36
[76]	Ti0.5CrFeCoNiCu	fcc	-3.70	14.70	4.82	8.36	0.12
[76]	Ti0.8CrFeCoNiCu	fcc+Laves	-6.75	14.87	5.70	8.14	0.13
[9]	Ti2CrFeCoNiCu	Compounds	-14.04	14.53	7.24	7.43	0.15
[69]	TiCrFeCoNi	fcc+bcc+CoTi2	-16.32	13.38	6.68	7.40	0.14
[76]	TiCrFeCoNiCu	fcc+Laves	-8.44	14.90	6.12	8.00	0.14
[45]	TiCrZrNbMo0.5Ta0.5	bcc+bcc+Laves	-4.92	14.53	8.04	4.90	0.22
[69]	TiV0.25ZrNbMo	bcc	-2.60	12.71	6.32	4.76	0.30
[69]	TiV0.5ZrNbMo	bcc	-2.60	12.71	6.32	4.76	0.30
[69]	TiV0.75ZrNbMo	bcc	-2.70	13.33	6.73	4.79	0.28
[69]	TiV1.5ZrNbMo	bcc+β-Zr bcc	-2.71	13.25	7.01	4.82	0.26
[69]	TiV2ZrNbMo	bcc+β-Zr bcc	-2.67	12.98	7.07	4.83	0.25
[69]	TiV3ZrNbMo	bcc+β-Zr bcc	-2.53	12.26	7.06	4.86	0.23
[68]	TiVNbTa	bcc	-0.25	11.53	3.93	4.75	0.05
[69]	TiVZrNbMo	bcc+β-Zr bcc	-2.72	13.38	6.85	4.80	0.27
[42]	TiZrNbHfTa	bcc	2.72	13.38	4.99	4.40	0.12
[69]	TiZrNbMo	bcc	-2.50	11.53	5.99	4.75	0.31
[77]	VFeCoNiCu	fcc	-2.24	13.38	2.20	8.60	0.10
[41]	VNbMoTaW	bcc	-4.64	13.38	3.15	5.40	0.34
[78]	ZrNbHf	bcc	3.56	9.13	5.00	4.33	0.13

Table 3.1 Collection of thermodynamic and electronic parameters of some HEAs published between 2004 and 2014, which have been calculated using the macro included in Appendix 1.

Prediction of weld tracks penetration

The objective of the electron beam melting to create a weld pool was to mix the various elements and the foil together uniformly and so calculation were performed to estimate the weld pool depth, to ensure it was sufficient to penetrate a significant depth below the

foil at different beam speeds. Therefore, the combinatorial approach reported here requires the determination of the electron beam penetration during melting in order to estimate the final weld pool depth. The heat transfer solution obtained from the Rosenthal equation, explained in chapter 2, is used for predicting the penetration of the molten pools into the solid. The calculation of the electron beam penetration into the workpiece requires an explicit mathematical method such as Newton-Raphson. An algorithm to obtain the penetration of the beam has been developed under the platform Scilab, which is included in Appendix 1. The calculation requires the identification of (1) the operational parameters including efficiency, electron beam power and speed; and (2) the material properties at the welding temperature such as thermal conductivity, κ; heat capacity, C_p; density, ρ; thermal diffusivity, α and melting temperature, T_m.

3.3 Processing Techniques

Production of HEAs by Arc Melting

Required alloys were produced at equiatomic composition, from high purity elemental material $(> 99.9\%)$ mainly supplied by Goodfellow and Sigma-Aldrich. For equiatomic composition, 5 grams of each alloy was melted into buttons of around 10mm diameter in an argon backfilled vacuum arc-melter (MAM-1 Edmund Buehler), and remelted 5 times to ensure homogeneity. The weight of each element required for the produced alloy systems is included in Table 3.2.

Alloy system	Ti	V	Mn	Fe	Co	Ni	Nb
TiMnFeNi	1.1		1.26	1.28		1.35	
MnFeCoNi			1.20	1.22	1.29	1.28	
TiVMnNb	0.97	1.03	1.11				1.88

Table 3.2 Amount (in grams) of each element required for producing 5 g of each alloy by arc melting.

Material preparation for High throughput processing route

The processing route used for the combinatorial high-throughput approach uses high purity raw materials in powder or/and foil shape. Four different systems (1) $Ti_xCrFeCoNi$, (2) $V_xTiMnNb$, (3) $Zr_xTiNbHf$ and (4) $Ti_xHfTaWRe$ have been identified as SUX01, SUX02, SUX03 and SUX04 respectively and produced by SPS and EBM.

The element that varies in quantity over the whole system (i.e. Ti in SUX01 and SUX04, V in SUX02 and Zr in SUX03) is made up as a sheet, while the other components in the system are powders of similar sizes mixed in equiatomic ratio. Table 3.3 contains the main characteristics of each element, such as purity and form as well as their atomic and weight% included in each experiment.

	Element used as a foil			Element used as powder			
Alloy system	Element	Purity (%)	Disc shape (mm)	Element	Purity (%)	(at%)	(wt%)
SUX01	Ti	99.6+	60x0.075	Cr	99.9	25	23.06
$Ti_xCrFeCoNi$				Fe	99.9	25	24.77
				Co	99.9	25	26.14
				Ni	99.9	25	26.03
SUX02	V	99.9+	60x3	Ti	99.9	33.3	24.46
$V_xTiMnNb$				Mn	99.9	33.3	28.07
				Nb	99.9	33.3	47.47
SUX03	Zr	99.8	60x0.25	Ti	99.9	33.3	24.46
$Zr_xTiMnNb$				Mn	99.9	33.3	28.07
				Nb	99.9	33.3	47.47
SUX04	Ti	99.6+	40x0.075	Hf	99.9	25	24.47
$Ti_xHfTaWRe$				Ta	99.9	25	24.8
				W	99.9	25	25.2
				Re	99.9	25	25.53

Table 3.3 Characteristics of the elements used for the high throughput processing experiments.

Processing by Spark Plasma Sintering (SPS)

The high throughput approach requires a thin layer composed of one single element and a sample composed of a mixture of various elements. An Spark Plasma Sintering FCT Systeme GmbH from Rauenstein was used to produce compact samples of a powder mixture with a metallic foil attached to one of the surfaces. Other consolidation techniques such as hot isostatic pressure or pressureless techniques could have given the same results whereas longer dwell times or higher temperature is required. Spark Plasma Sintering, SPS is used here as the first processing technique to create pre-consolidated samples. Figure 3.1 shows a sketch of the SPS chamber (left) and the differences between the conventional approach (top right) used to sinter powder materials and the alternative approach (bottom right) used for the high throughput route proposed in this project. In the alternative route, a thin metallic foil is attached on the top surface of the powder mixture and is then compacted by SPS following

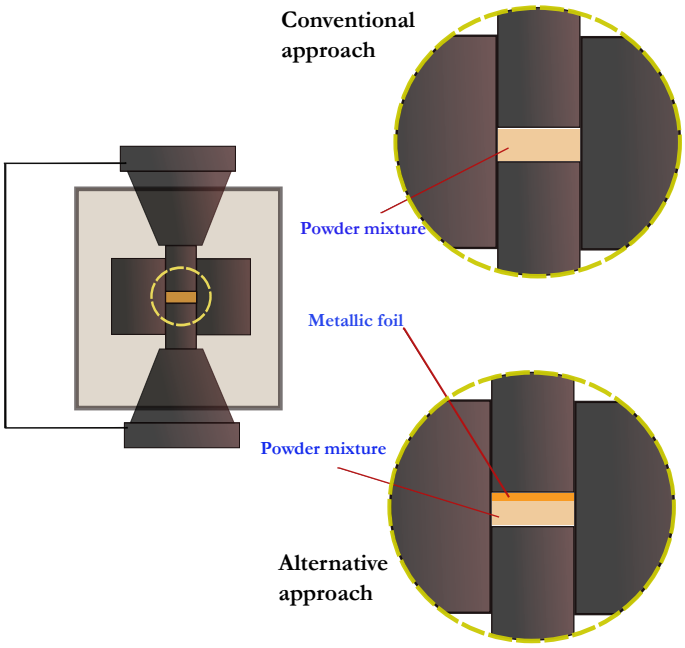

Fig. 3.1 Schematic of the SPS chamber showing the conventional approach (top right) and the alternative method (bottom right) for the synthesis of specimens through the high throughput approach.

the conventional approach (see Figure 2.14 in Chapter 2). The metallic foil was obtained from two different methods: (1) A commercial metallic sheet composed of a high purity element, which was shaped to the desired diameter delimited by the mould and (2) producing a thin disc of a single high purity element from powders through SPS. Table 3.4 includes the conditions of both foil and powder mixture for consolidation of SUX01, SUX02, SUX03 and SUX04.

Processing by Electron Beam Melting (EBM)

During melting, an electron beam is provided to melt 10 mm length lines (also called weld tracks) at different speeds on top the thin layer of the SPS-ed sample. By doing this, the penetration of the beam into the weld track will differ and, consequently the composition of each weld track.

The electron beam of an ARCAM EBM S12 (a machine designed for additive manufacturing) was used here to produce several weld tracks in the pre-consolidated specimen by SPS. A simple diagram showing the use of the electron beam for the creation of the weld tracks can be seen in Figure 3.2. One single sample contains several weld tracks, which differ in the operational conditions of the electron beam, and consequently in the shape of the actual weld

	SUX01	SUX02	SUX03	SUX04
MATERIALS				
Foil	3 Sheet 3x75 mm	Powder 50 g	1 Sheet 1x250 mm	3 Sheets 3x75 mm
Powder mixture				
Mould diameter / mm	60	60	60	40
Weight / g	140	95	140	116
OPERATIONAL PARAMETERS				
Atmosphere	Ar	Ar	Ar	Ar
Temperature / °C	900	900	1085	900
Pressure / kN	57	57	57	57
Dwell time / min	5	20	5	5

Table 3.4 Conditions of material consolidated through SPS and the operational parameters.

tracks.

The control of several electron beam parameters and conditions of the chamber allows the

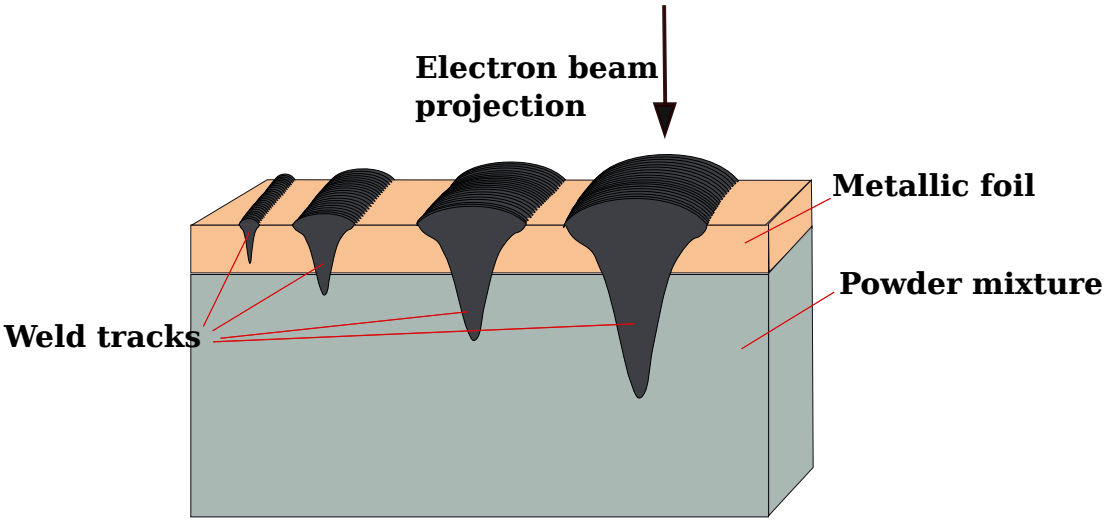

Fig. 3.2 Schematic diagram of the production of several weld tracks into the top surface of the SPS consolidated specimen.

user to choose the conditions at which each weld track will be produced. The operational parameters are electron beam current, speed and focus offset and temperature at which the welding should take place. Tables 3.5 and 3.6 include the operational parameters selected for both the consolidation and the welding for each metallic system; Operational parameters for production of SUX01 and SUX02 are shown in Table 3.5 while Table 3.6 includes the production parameters of SUX03 and SUX04.

ID: **SUX01**	TixFeCoCrNi			
Spark Plasma Sintering				
Mould diameter:	**60mm**			
Foil production:	Consolidation of 3 sheets			
	Temperature / °C: Pressure / kN:	900 57	Atmosphere: Dwell time / min:	Ar 5
Foil and mixture				
	Temperature / °C: Pressure / kN:	850 57	Atmosphere: Dwell time / min:	Ar 10
Electron Beam Welding				
wt ID	Voltage kV	Current mA	Focus Offset mA	Speed mm/s
SUX01-01	60	20	4	1300
SUX01-02	60	20	4	1200
SUX01-03	60	20	4	1100
SUX01-04	60	20	4	1000
SUX01-05	60	20	4	900
SUX01-06	60	20	4	800
SUX01-07	60	20	4	700
SUX01-08	60	20	4	600
SUX01-09	60	20	4	500
SUX01-10	60	20	4	400
SUX01-11	60	20	4	300
SUX01-12	60	20	4	200
SUX01-13	60	20	4	100
SUX01-14	60	20	4	90
SUX01-15	60	20	4	80
SUX01-16	60	20	4	70

ID: **SUX02**	VxTiMnNb			
Spark Plasma Sintering				
Mould diameter:	**60mm**			
Foil production:	Consolidation of high purity vanadium powder			
	Temperature / °C: Pressure / kN:	1200 57	Atmosphere: Dwell time / min:	Ar 40
Foil and mixture				
	Temperature / °C: Pressure / kN:	900 57	Atmosphere: Dwell time / min:	Ar 10
Electron Beam Welding				
wt ID	Voltage kV	Current mA	Focus Offset mA	Speed mm/s
SUX02-01	60	25	4	1300
SUX02-02	60	25	4	1200
SUX02-03	60	25	4	1100
SUX02-04	60	25	4	900
SUX02-05	60	25	4	700
SUX02-06	60	25	4	500
SUX02-07	60	25	4	300
SUX02-08	60	25	4	1200
SUX02-09	60	25	4	100
SUX02-10	60	25	4	90
SUX02-11	60	2	4	70
SUX02-12	60	25	4	50
SUX02-13	60	25	4	30
SUX02-14	60	25	4	10

Table 3.5 Operational conditions used during consolidation and welding stages of SUX01 and SUX02

ID: **SUX03**	ZrxTiNbHf			
Spark Plasma Sintering				
Mould diameter:	**60mm**			
Foil production:	1 sheet			
	Temperature / °C: Pressure / kN:	N/A required	Atmosphere: Dwell time / min:	N/A required
Foil and mixture				
	Temperature /°C: Pressure / kN:	1085 57	Atmosphere: Dwell time / min:	Ar 5
Electron Beam Welding				
wt ID	Voltage kV	Current mA	Focus Offset mA	Speed mm/s
SUX03-01	60	20	4	1200
SUX03-02	60	20	4	1100
SUX03-03	60	20	4	1000
SUX03-04	60	20	4	900
SUX03-05	60	20	4	800
SUX03-06	60	20	4	700
SUX03-07	60	20	4	600
SUX03-08	60	20	4	500
SUX03-09	60	20	4	400
SUX03-10	60	20	4	300
SUX03-11	60	20	4	200
SUX03-12	60	20	4	100
SUX03-13	60	20	4	90
SUX03-14	60	20	4	80
SUX03-15	60	20	4	70
SUX03-16	60	20	4	60

ID: **SUX04**	$Ti_xTaWReHf$			
Spark Plasma Sintering				
Mould diameter:	**40mm**			
Foil production:	Consolidation of 3 sheets			
	Temperature /°C: Pressure /kN:	900 57	Atmosphere: Dwell time / min:	Ar 5
Foil and mixture				
	Temperature /°C: Pressure /kN:	1000 57	Atmosphere: Dwell time / min:	Ar 10
Electron Beam Welding				
wt ID	Voltage kV	Current mA	Focus Offset mA	Speed mm/s
SUX04-01	60	20	4	1100
SUX04-02	60	20	4	1000
SUX04-03	60	20	4	900
SUX04-04	60	20	4	800
SUX04-05	60	20	4	700
SUX04-06	60	20	4	600
SUX04-07	60	20	4	500
SUX04-08	60	20	4	400
SUX04-09	60	20	4	300
SUX04-10	60	20	4	200
SUX04-11	60	20	4	100
SUX04-12	60	20	4	90
SUX04-13	60	20	4	80
SUX04-14	60	20	4	70

Table 3.6 Operational conditions used during consolidation and welding stages of SUX03 and SUX04

3.4 Characterization Techniques

Micropreparation techniques

The sample produced were prepared for microstructural characterization and testing. Firstly, the section across both the arc melted and weld tracks sample were cut off using a Buehler, Isomet 5000 Linear Precision Saw and mounted in a Buehler, Simplimet 1000 automatic mounting press with conductive Bakelite; Secondly, samples were ground and polished in a Buehler, EcoMet/AutoMet 250 Grinder-Polisher machine until a flat mirrored surface was obtained.

A standard guide for preparation of metallographic specimens is described in the ASTM Standards under the designation number **E3-11**. This standard was used here for grinding and polishing of samples following the methods tabulated in E3-11 according to the hardness of the specimens (softer or harder materials are discriminated by their hardness being lower or higher than 450HV).

Within the scope of this project, the specific steps for the preparation of samples have been followed and are shown in Table 3.7. It contains four grinding steps followed by other four polishing steps and one finishing under certain conditions including: suspension, time, force applied, speed of the head and the plate and the rotation direction between the head and the plate.

Scanning Electron Microscopy (SEM)

Scanning Electron Microscopy is the type of microscope where an electron beam scans a sample obtaining an image from the signal generated at each point in the scan. The primary electrons projected on to the surface of the sample produce the emitted electrons and other radiations useful to form images, such as secondary and backscattered electrons, and analyse chemically the elements contained in the sample, such as x-rays.

The prepared samples were examined under Scanning Electron Microscopy (SEM, Siemens Inspect F), using secondary and backscattered electrons. EDX mapping was carried out at low and high magnification in order to determine the homogeneity of the samples. JEOL JSM 6400 SEM was used for EDX quantitative chemical analysis of the samples.

GRINDING					
	G1	G2	G3	G4	G5
Paper	P120	P240	P600	P800	P1200
Suspension	water				
Time / min	5-10				
Force / kN	15-20				
Disc speed / rpm	70-100				
Head speed / rpm	60				
Rotation direction	CONTRA				
POLISHING AND FINISHING					
	P1	P2	P3	F1	
Paper	cloth	cloth	cloth	cloth	
Suspension diamond	6 μm	3μm	1 μm	SiO_3-AlO_3	
Time / min	5-10	5-10	5-10	5-20	
Force / kN	5-10	5-10	5-10	5-10	
Disc speed / rpm	60-80	60-80	60-80	60-80	
Head speed / rpm	60				
Rotation direction	COMPO				

Table 3.7 General procedure followed during grinding (G1-G5) and polishing (P1-P3 and finishing, F1) of HEAs within the scope of this project.

Quantitative Phase Analysis

The volume % of the phases present in each weld track was measured through image analysis techniques. A commercial software Image J was used to prepare the candidate microstructure for the image analysis while a protocol has been followed as shown in Table 3.8.

X-ray diffraction for determination of the crystalline structure

X-ray diffraction is a method widely used for determining the structure of materials in the atomic scale. In the scope of this project it has been used for determining the crystalline structure of HEAs using either manual methods when simple structures are presented or chart comparison for identification of more complex phases in the database.

A flat surface of the bottom of the samples after arc melting was used for X-Ray Diffraction (XRD) scans for crystal structure characterization using a Siemens model D5000 XRD with Cu K_α radiation (wavelength 1.54056 A). X-ray traces were produced for a wide range of angles 2Θ from 30 to 120 °and corrected for systematic peak broadening with a $K_{\alpha 2}$ correction after measurement.

Step	Operation	Command
1	Scale image	Analyze-Set scale
2	Duplicate image	Image-Duplicate
3	Threshold	Adjust-Threshold
4	Make binary	Process-Binary-Make binary
5	Close/open	Process-Binary-Open or Close
6	Choose area	Rectangular selection
7	Measure 9 areas of the weld track	Analyze-Analyse particles
8	Calculate mean and error	using 9 measurements

Table 3.8 Steps followed during the manual measuring of quantity of the phases present in the weld tracks.

Testing Techniques

The samples produced were subjected to Vickers hardness testing using a Struers Durascan 70 system, with loads between 50 and 100 g and a dwell time of 15 sec.

The ASTM standard **E348 11e1** is used here as a reference. In order to measure the hardness of each weld track, where one single measurement may not be representative of the bulk hardness of the material, several indentations were made in the section across the weld tracks after microstructural evaluation. The spacing between indentations is higher than 2.5 times the diagonal of one indentation, which is the usually recommended separation to avoid intererference between results. Due to the small area of surface exposed to testing, a microindentation hardness test was used. It also may allow testing of the individual phases presented within a weld track.

Chapter 4

Prediction of High Entropy Alloys using Principal Component Analysis

4.1 Introduction

Chapter 2 has discussed the predictive techniques which could be used for alloy design and have previously been employed for HEAs. Most of the techniques end up indicating the split of HEAs from BMGs or just mapping all the HEAs found in the literature according to certain values. However, approaches exist to process data where many variables need to be taken into account, reducing dimensionality and allowing the grouping of data and the identification of patterns. One such technique is Principal Component Analysis (PCA), a multivariate analysis method where a statistical tool is employed to reduce the variables of a dataset into principal components consisting of orthogonal linear combinations of the original variables, which retain as much as possible of the original information [59, 79]. Therefore, applying PCA to the analysis of HEA data may help to highlight the most important variables, as well as provide an empirical tool for prediction and discovery of novel materials.

4.2 Experimental conditions

The prediction of HEAs is performed in Matlab using Principal Component Analysis (PCA) techniques and validation has been carried out by producing 3 new HEAs by arc melting followed by microstructural characterization by SEM and XRD. Hardness testing has also been performed on the 3 new alloys as an additional tool. PCA has been run over 79 different HEAs (the input observations), analysed previously by other authors, and 5 variables, which

seem to have a great effect on the formation of this kind of alloy. The dataset is collected in Table 3.2.

4.3 Results and discussion

The PCA output provides the information required for the interpretation of the original dataset, which is visualized through tables and biplots and which are given in Tables 4.1, 4.2 and 4.3.

Table 4.1 summarises the parameters of the alloys used in the analysis (79 observations) giving the mean and standard deviation of each variable. As can be observed from the variables, their units are different to each other and there is a substantial difference in magnitudes (e.g. mean ΔS_{mix} is 13.70 kJ/molK whereas $\Delta\chi$ mean is 0.13 Pauling). This fact requires the analysis to be carried out under the correlation matrix instead of the covariance, in order to avoid difference in magnitudes (vector length) and misunderstanding of the results. The correlation matrix is shown in table 4.3.

Table 4.2 shows the weights/contribution of each variable to the new principal compo-

	Observations	Mean	Standard deviation
ΔH_{mix}	79	-9.34	7.712
ΔS_{mix}	79	13.70	1.462
δ	79	5.49	1.880
VEC	79	6.91	1.390
$\Delta\chi$	79	0.13	0.065

Table 4.1 Principal Component Analysis output: Descriptive statistics

nents (PCs), which are represented by the eigenvectors as well as the variance given by each PC.

Firstly, the number of principal components (PCs) required to represent the data is shown in Table 4.4. It shows the correlation of PCs with the variables (1 means perfect correlation, -1 inverse correlation and 0 no correlation) and the variance represented by each PC. One criterion for selecting the number of PCs needed is based on the cumulative percentage of the total variance which is often considered satisfactory when it lies within the range 70% and 90% [59]. Therefore, the first PCs where the cumulative percentage exceeds the cut-off value would preserve most of the information. Looking at Table 4.4, the cumulative variance

	PC1	PC2	PC3	PC4	PC5
Eigenvectors					
ΔH_{mix}	-0.462	0.442	0.450	-0.285	0.553
ΔS_{mix}	0.397	-0.403	0.692	-0.426	-0.130
δ	0.643	-0.005	-0.136	0.160	0.736
VEC	-0.351	-0.552	0.320	0.646	0.223
$\Delta\chi$	0.301	0.578	0.443	0.539	-0.293
Eigenvalues:	2.00	1.57	0.70	0.44	0.27
Percentage of variance(%):	40.02	31.51	14.29	8.76	5.42
Cumulative	40.02	71.53	85.82	94.58	100

Table 4.2 Principal Component Analysis output: Eigenvalues and eigenvectors

	PC1	PC2	PC3	PC4	PC5
ΔH_{mix}	-0.660	0.549	0.379	-0.191	0.288
ΔS_{mix}	0.566	-0.501	0.588	-0.281	-0.069
δ	0.911	0.002	-0.112	0.108	0.382
VEC	-0.492	-0.698	0.270	0.429	0.115
$\Delta\chi$	0.407	0.737	0.373	0.357	-0.153

Table 4.3 Principal Component Analysis output: Correlation between variables and PCs

exceeds 70% after the second PC, which means that the first two PCs represent the 72% of the information given by the five variables. 3 PCs are enough to describe 86% of the variance.

Secondly, the effect of PC1 and PC2 is visualized through a biplot as shown in Figure

	PC1	PC2	PC3	PC4	PC5
ΔH_{mix}	-0.66	0.55	0.38	-0.20	0.29
ΔS_{mix}	0.57	-0.49	0.59	-0.27	-0.07
δ	0.90	0.00	-0.10	0.11	0.37
VEC	-0.50	-0.70	0.27	0.43	0.11
$\Delta\chi$	0.41	0.74	0.36	0.36	-0.14
Eigenvalues	2.00	1.57	0.70	0.44	0.27
Percentage of variance(%)	40.02	31.51	14.29	8.76	5.42
Cumulative	40.02	71.53	85.82	94.58	100

Table 4.4 The correlation between PC1, PC2, PC3 and the variables.

4.1a (biplots showing the relationship between variables and observations and the variables themselves according to PC1-PC3 and PC2-PC3 are included into Figures 4.1b and 4.1c). This plot is useful for easy visualization of the data as well as interpretation of the relationship between the alloys structure and the variables.

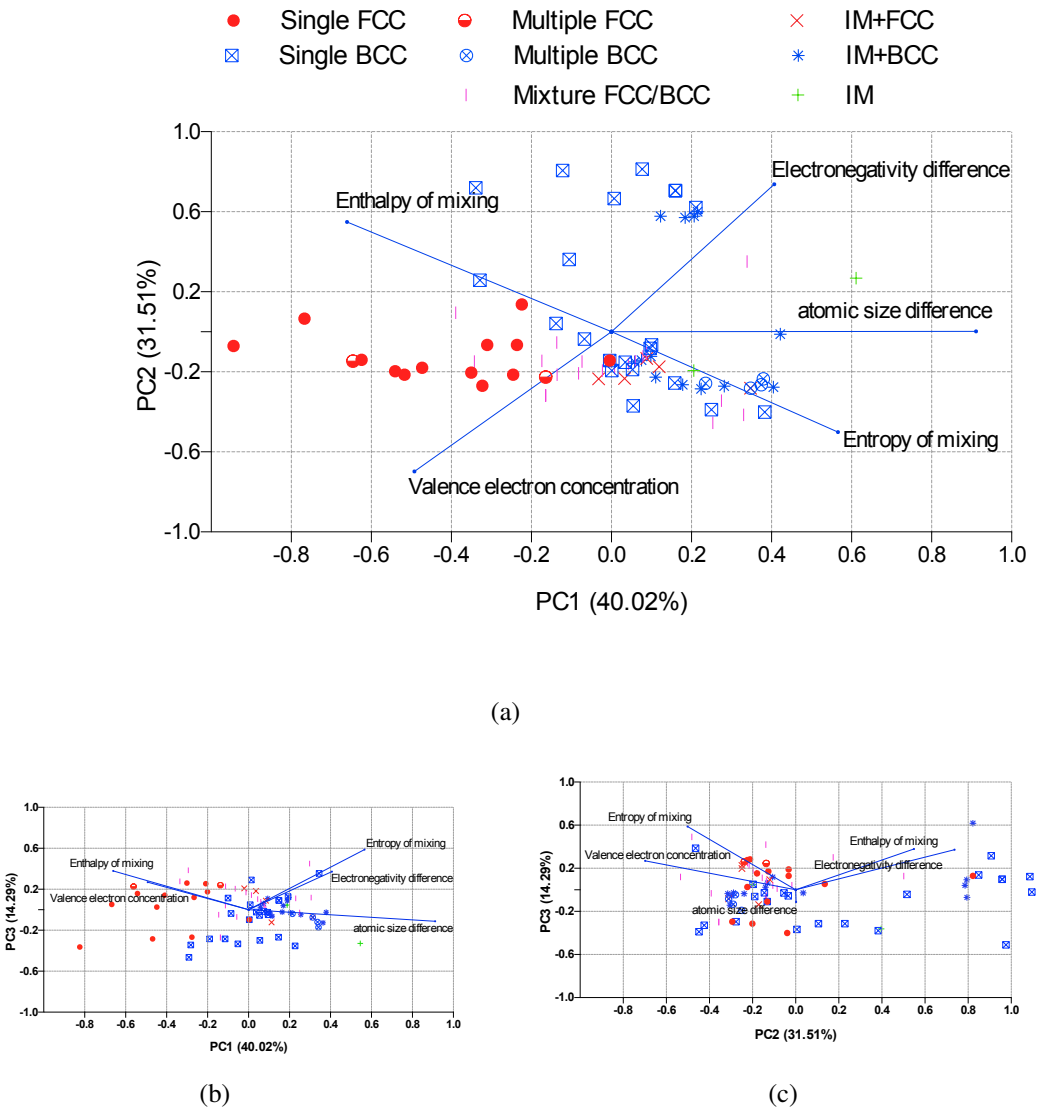

(a)

(b)

(c)

Fig. 4.1 (a) Biplot of the first two PCs (capturing 72% of the variation), (b) biplot of PC1 against PC3 (capturing 55% of the variation), (c) biplot of PC2 and PC3 (capturing 46% of the variation).

These figures not only include the alloys reported as intermetallics or multiple phases, single phase fcc and single phase bcc, shown by different symbols, but also the positions of the axes corresponding to variations in each of the different input variables as lines. It is clearly observed that alloy systems giving different structures tend to segregate into different regions on the plot. This implies that the crystalline structure of novel HEAs can

be predicted in a simple way by identifying the region where the candidate alloy would lie from its thermodynamic and electronic properties or even by identifying the target properties for an alloy to have a desired structure, (for example, by orthogonal projections of the observations onto the PC axes) [59, 79]. There is a certain region of overlap between regions, but from the alloys plotted the discrimination obtained would be expected to be good.

It should be noted that the enthalpy of mixing used here is a parameter relating to the solid solution, though this could be much larger and negative if the enthalpy of formation of certain intermetallics were considered. This, coupled with the small entropic contribution in (highly ordered) intermetallics, means that the Gibbs free energy of such phases can easily be very low, making them more stable than the solid solution due to effects that are not directly considered in this approach. In addition, there is not a clear effect of the entropy of mixing in the crystalline structure of these equiatomic alloys due to the overlapping between observations (see Table 4.4), which has mainly been used for differing between conventional alloys and HEAs, while giving their actual name, but nothing else.

Here it is effectively assumed that the interactions driving ordering are small, and it is somewhat unexpected that the predictions work in spite of this. However, even this type of plot may not be necessary to make adequate predictions in all cases. For example, it can be noted from Figure 4.1a that the axes representing the variation in δ and VEC are at a non-zero angle to each other, showing that between the two a proportion of the variance can be represented. This is expected as plotting these parameters (or parameters derived from them) against each other has been found by previous authors to go some way to isolating the structures, such as Guo et al. [5] and Polletti et al. [7]. Nevertheless, the angle between the vectors representing VEC and δ is obtuse, indicating some degree of (negative) correlation. The angle between some other variables is closer to 90 degrees, indicating that they express the variability in a more independent manner (vectors at right angles are fully independent in terms of the plotted components). An example of this would be VEC and ΔH_{mix}.

Examples of the data plotted against only 2 of the five variables are shown in Figure 4.2a and Figure 4.2b. These graphs show VEC against δ, representing the type of plot demonstrated in previous work, and VEC against ΔH_{mix}, where trends are found to be particularly clear. Figures 4.3 and 4.4 also include a complete series of plots containing the alloys systems reported with respect to parameter pairs.

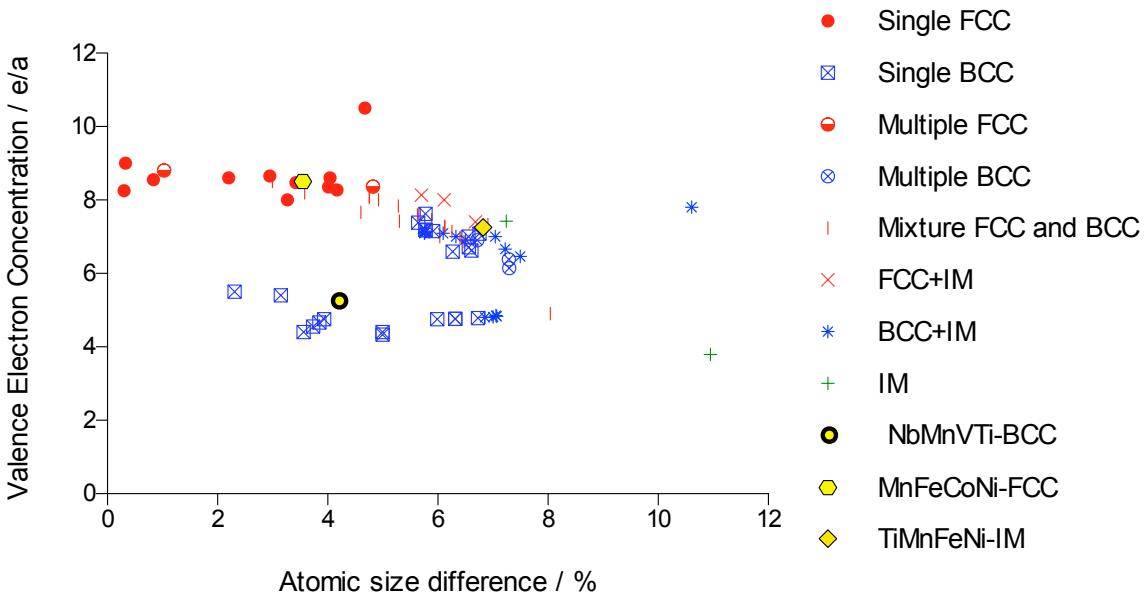

(a)

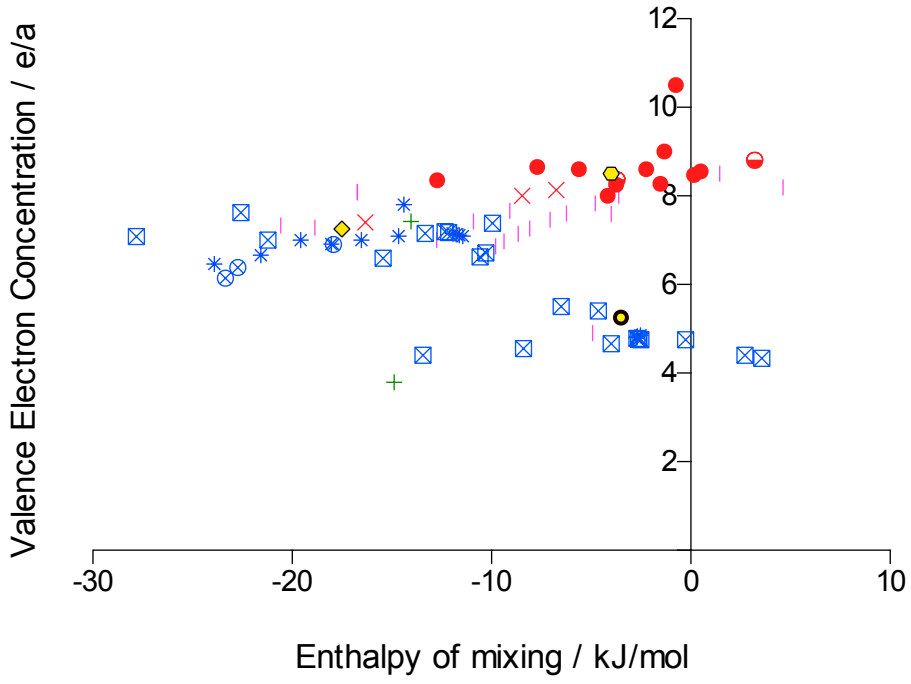

(b)

Fig. 4.2 (a) The correlation between VEC and δ and the formation of HEAs showing different crystalline structures, (b) the correlation between VEC and ΔH_{mix} and the formation of HEAs showing different crystalline structures.

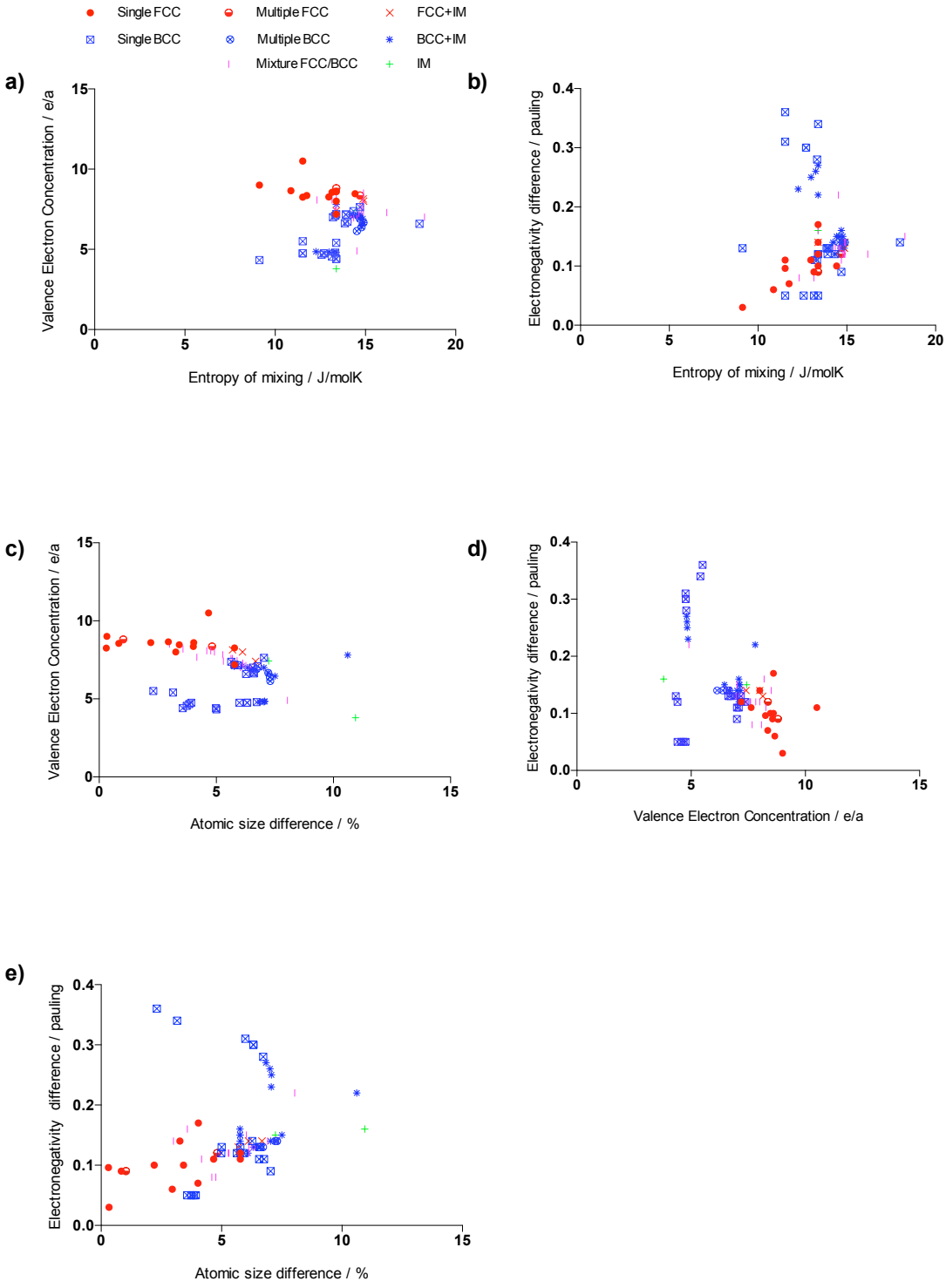

Fig. 4.3 Collection of plots of variables by pairs. (a) VEC against ΔS_{mix}, (b) $\Delta\chi$ against ΔS_{mix}, (c) VEC against δ, (d) $\Delta\chi$ against δ, (e) $\Delta\chi$ against δ.

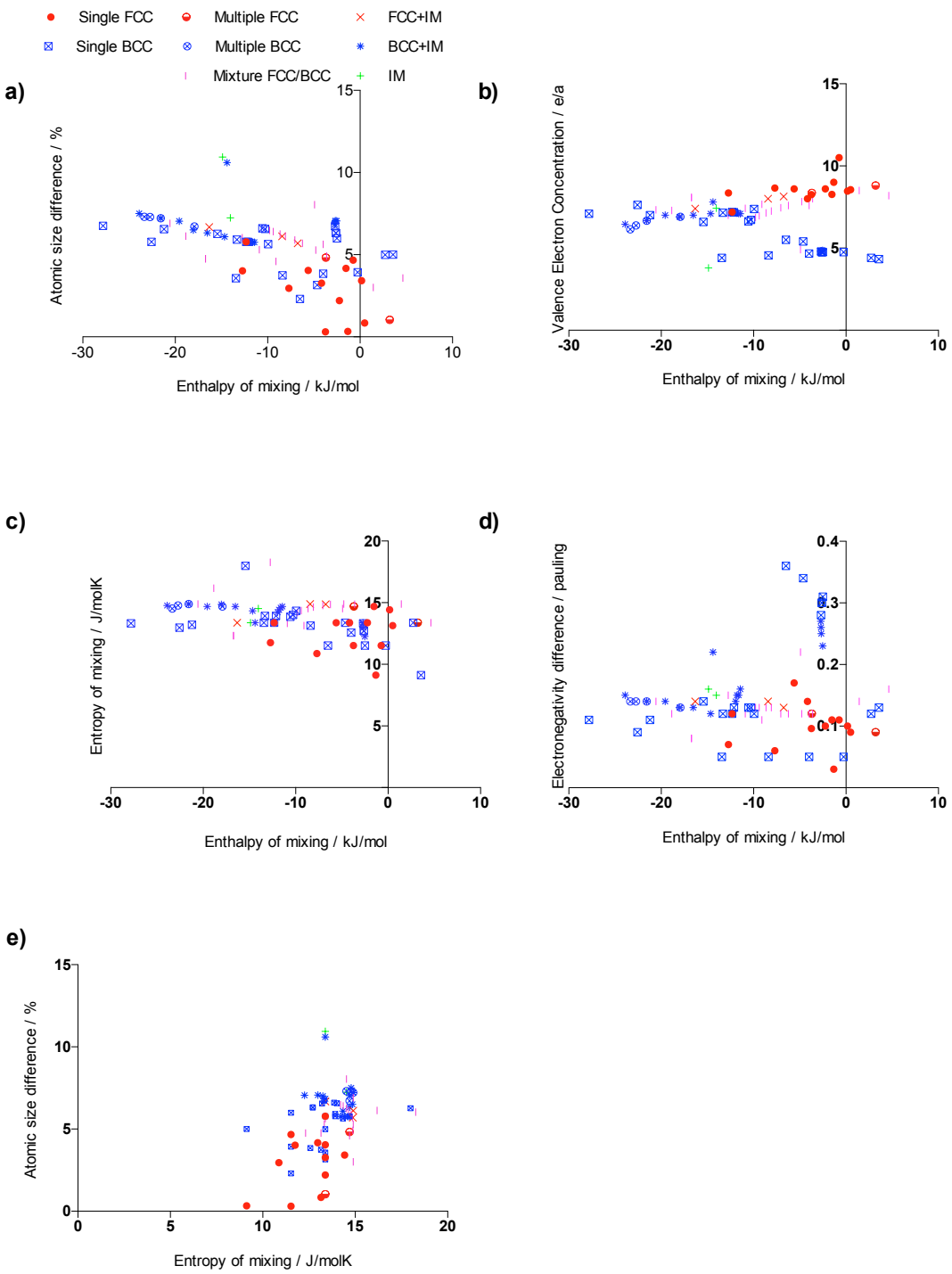

Fig. 4.4 Collection of plots of variables by pairs. (a) δ against ΔH_{mix}, (b) VEC against ΔH_{mix}, (c) ΔS_{mix} against ΔH_{mix}, (d) $\Delta\chi$ against ΔH_{mix}, (e) δ against ΔS_{mix}.

VEC and δ are plotted against each other for the full dataset in Figure 4.2a, with different symbols used to indicate the alloys that are reported to form intermetallics or multiple phases, single phase fcc and single phase bcc. These data show clear groupings of the structures in different regions of the plot. However, it is also clear that there are important variables affecting the behaviour that are not fully represented in this plot; the majority of the data points track an apparent curve, hinting at a more complex interrelationship between the parameters.

VEC against ΔH_{mix} is shown in Figure 4.2b. This way of presenting the data does show almost entirely separated regions for intermetallic or multiphase alloys, and single phase fcc or single phase bcc. The separation between multiple and single phase appears to occur on the ΔH_{mix} axis, while the VEC seems to influence the split between fcc and bcc structure, harking back to the ideas of Hume-Rothery. Importantly, these results would appear to permit the design of HEAs, as both the VEC and ΔH_{mix} can be calculated for a candidate alloy, and the location on the graph of the resultant point evaluated to determine the structure.

Taking both of these plots into account, ranges can be defined for each of the 3 parameters where the formation of different structures would be expected, Table 4.5 (note that these represent the ranges in which these structures are most likely to form without confusion with other structures, not the full extent of their observed envelopes). These ranges can form the basis of design of new alloys.

To test these relationships, the novel alloy compositions were selected, designed so that

Structure	ΔH_{mix} kJ/mol		VEC e/a		δ %	
	min	max	min	max	min	max
Single phase bcc	-5	0	3	6	2	6
Single phase fcc	-5	0	8	11	2	6
Compounds and multiple phases	-20	-15	6	8	6	8

Table 4.5 The required ranges for key variables to produce HEAs of different structures

their ΔH_{mix}, δ and VEC values spread them across the plots in Figure 4.2a and Figure 4.2b, with each one falling in a different region. To fully challenge the predictive capabilities, the alloys were further all chosen to have 4 components (at equiatomic composition), as 4 component HEAs are particularly rare. After the predictions were made (values represented as yellow dots in Figure 4.2), samples of each alloy were produced by arc melting, and were examined using XRD and SEM (Figures 4.5 and 4.6). These results show that the structures

have formed as expected, TiMnFeNi is a mixture of phases and MnFeCoNi and TiVMnNb are two novel 4 component FCC and BCC alloys respectively. According to the definitions that we have applied, the TiMnFeNi alloy would not be classed as a HEA, because it contains multiple phases, which are likely to be intermetallics, but the MnFeCoNi and TiVMnNb can be as their constituent phases are both solid solutions and simple.

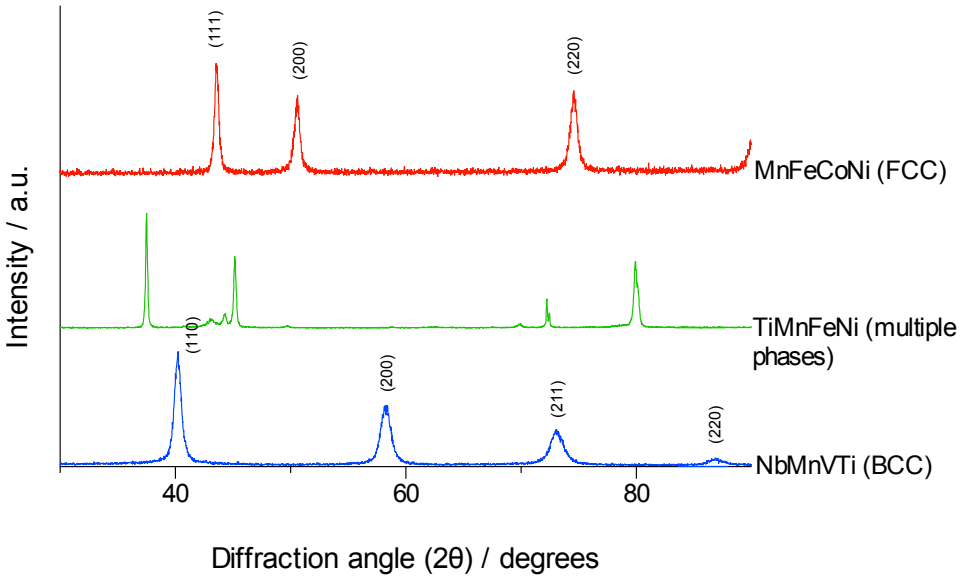

Fig. 4.5 X-ray patterns $\theta - 2\theta$ scans for samples predicted to be multiphase, fcc and bcc. (a) TiMnFeNi (multiphase), (b) MnFeCoNi (fcc) and (c) TiVMnNb (bcc)

The X-ray traces of the alloys show peaks consistent with the majority of the material being made up of the predicted phases (fcc for MnFeCoNi, bcc for TiVMnNb and mixed phases/intermetallics for TiMnFeNi). While these traces may not have high enough resolution to show if there are very small amounts of other phases present, results of this type are usually taken as evidence of the formation of HEAs (it should be noted that recent work indicates that many HEAs thought to be single phase actually show segregation on a fine scale [9]). The micrographs shown in Figure 4.5 are consistent with this view, with a multiphase structure shown by TiMnFeNi (shown in more detail in the high magnification image for clarity), a grain structure present in MnFeCoNi and interesting dendritic structure is observed in TiVMnNb.

Examining the 110 X-ray peak for TiVMnNb and analysing the data more closely, Figure 4.7, reveals that this is in fact a 2 phase microstructure. The deconvolution shows the

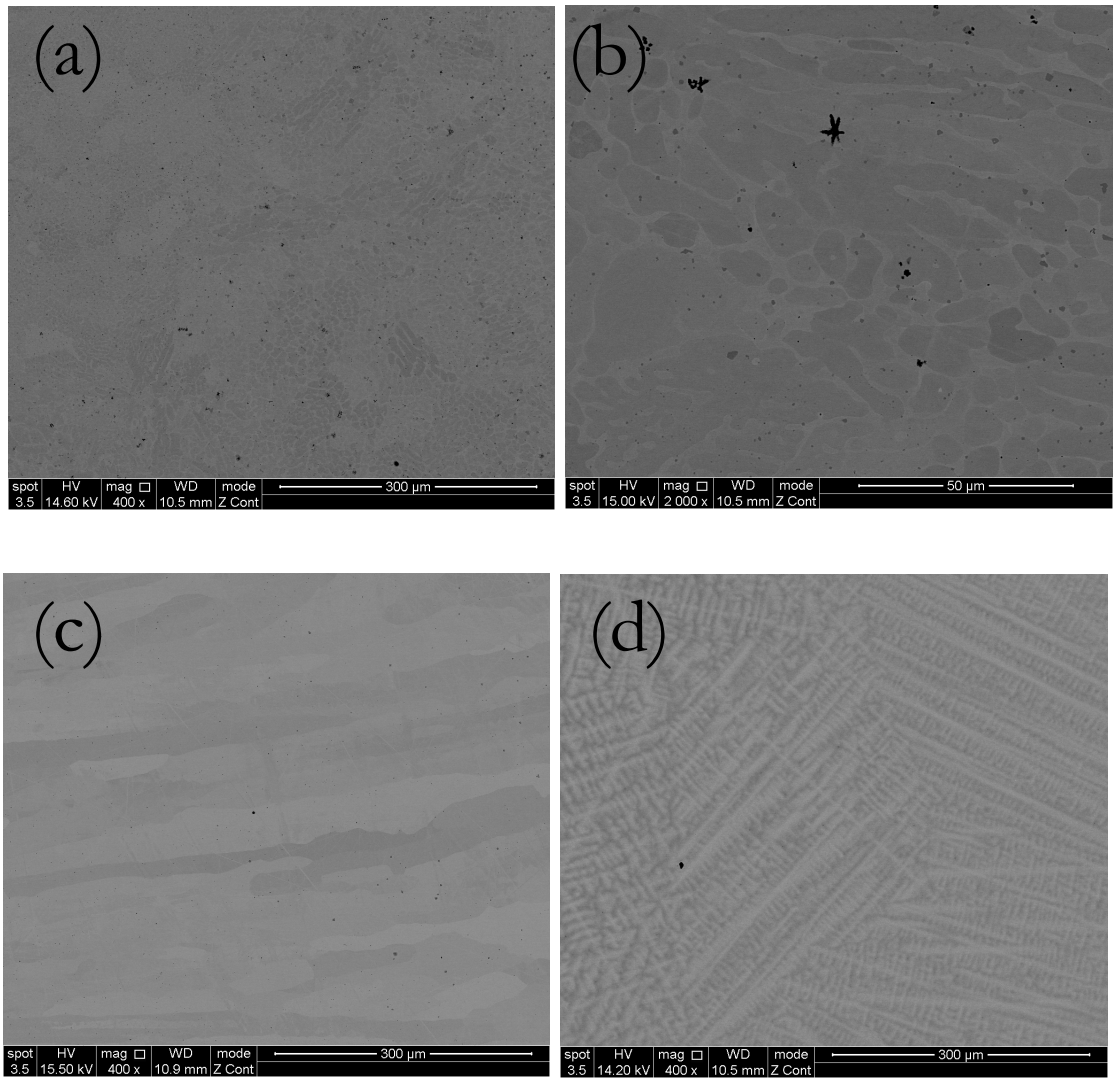

Fig. 4.6 Backscattered images of (a) and (b) multiphase TiMnFeNi at low and high magnification respectively, (c) single fcc MnFeCoNi and (d) apparently single bcc TiVMnNb.

presence of two peaks, corresponding to 2 bcc phases with similar lattice parameters (approximately 3.14 and 3.15 Å). It is interesting to note that this type of microstructure (i.e. comprising 2 solid solutions with simple crystal structures) seems to be relatively common in multiprincipal component alloys, having been observed in [69] and [43], indicating that this may be an interesting area for future research.

The hardness data for the alloys shows that the fcc structure has the lowest hardness

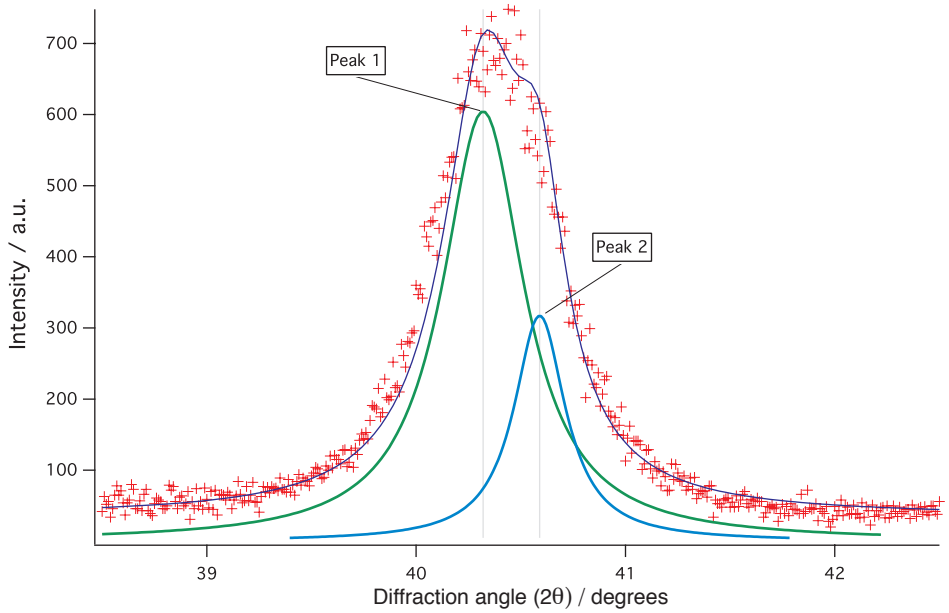

Fig. 4.7 X-ray trace of the specimen predicted to be bcc (TiVMnNb) within diffraction angle between 38.5 °to 42.5 °.

with a value of 164.2 ± 12.4HV0.1, the bcc with a value of 476.3 ± 16.5HV0.1, is the next highest with the highest value occurring for the structure exhibiting multiple phases with a value of 751.5 ± 26.7HV0.1. This order would be expected from the nature of dislocation motion in single and multiphase microstructures [80]. It can be noted in passing that TiVMnNb, which shows a high hardness, bcc structure and would be predicted to show a high melting point, could be an attractive material for applications in high temperature aggressive environments.

4.4 Summary

The work discussed in this chapter has performed Principal Component Analysis on a dataset of High Entropy Alloys for the first time. This has shown that while the previously introduced

method of exploring the likely phase formation in these materials of plotting electronegativity against atomic size difference captures some of the variability, a greater amount can be expressed in plots of other parameters. In particular, when plotting the wider dataset of multicomponent alloys the structures formed resolve themselves with an unusually high degree of consistency into largely separate regions on a plot of VEC against ΔH_{mix}. The explicit consideration of entropy is not required in this approach. Using this, a series of novel four component alloys are predicted with different structures, which on production are found to be consistent. While not giving a conclusive explanation for the reasons behind the formation of these phases, this work provides a simple to use tool for the prediction of HEA forming compositions of many types, which has so far proved accurate. Nevertheless, some experimental confirmation and exploration of novel HEAs compositions will still be required. For this techniques to allow the screening of large number of compositions, scanning across composition ranges are required.

Chapter 5

High throughput synthesis of HEAs: novel methodology and its validation.

5.1 Introduction

Conventional approaches used to investigate novel alloys involve the study of one composition at a time by changing elemental quantities aiming to reach the most suitable properties for a particular application. This approach requires a huge amount of time, which increases with the addition of further elements. An alternative approach, which allows rapid exploration of a wide parameter space by quickly changing the types and amounts of elements involved may bring several advantages, such as reproducibility and automation of processes as well as fast discovery of knowledge and obviously the reduction of the time required. This approach is motivated by factors such as discovery of completely new materials, among others [56].

Computational AB initio calculations have already been used to explore the low temperature phase diagrams of some binary systems, inorganic compounds and some potential magnetic and spintronics systems. The contribution of computational techniques to the combinatorial high throughput discovery of new materials becomes even more powerful in those situations where high temperature or pressures are required during experimentation or hazardous, reactive elements are involved as well as elements not physically available [81, 82]. Therefore, the combination of those computational and experimental techniques could build a stronger database of new materials composed of multiple elements.

A specific system which has already been analysed (by conventional means) and reported is Ti_xFeCoCrNi [12], with 0, 7 and 12 at% Ti. It is found that the number of phases included in

the system increases with increasing titanium content, from a simple fcc solid solution at Ti 0 and 7 at% to multiphase at 12 at%. This system would be a good candidate for validation of new methods, and further exploration.

This chapter is mainly focused on the development of a suitable methodology for synthesizing HEAs while following a high throughput route and using conventional equipment; high throughput methods are particularly suited to the investigation of HEAs, with other techniques with this capability recently proposed [83]. Given the existing partial experimental data in the literature the alloy system $Ti_xFeCoCrNi$ provides an ideal example that can be used to validate the novel high throughput procedure introduced here in High Entropy Alloys.

5.2 Experimental technique

The characteristics of the elements used in this chapter are included in Table 3.3 corresponding to SUX01; the elements used here are a mixture of 99.99% pure Fe, Co, Cr and Ni powders at 25 at% each and a disc of 99.99% pure Ti foil whose diameter and thickness are 60 and 0.300 mm respectively. Spark Plasma Sintering is used to consolidate the powder mixture into the form of a 60 mm diameter disc with the foil on the upper surface, under 850°C temperature, 57 kN load and a dwell time of 10 minutes using graphite moulds. Boron nitride is sprayed on the face of the punch that contacts with the foil in order to prevent it from sticking to the moulds. After the consolidation step, the Electron Beam Melting (EBM) equipment is used to provide an electron beam and move this in a controlled manner to produce 16 weld tracks of 20 mm length on the surface of the specimen where the Ti foil is attached (see Figure 3.2 for clarification). The processing parameters of both SPS and EBM are collected into Table 3.5.

A metallographic cross section of the weld tracks was prepared for (1) EDX chemical analysis, for obtaining backscattered images and (2) hardness tests performed under a load of 100 g and a dwell time of 15 s. Quantitative phase analysis, QPA was carried out using an image analysis procedure described in Chapter 3. In addition, larger samples were made up from elemental ingot for crystal structure analysis by X-ray diffraction.

5.3 Results and discussion

5.3.1 Design of High Entropy Alloys

Compositional design

The first stage of the design step is applied to ensure that the alloy system used has the potential to form HEAs. It is done by setting out thermodynamic and electronic parameters such as ΔH_{mix}, ΔS_{mix}, δ, VEC and $\frac{Tm}{Tc}$ used for determining the formability of solid solution HEAs. The calculation of these parameters is carried out as performed by previous authors [5, 30] and the values of which are included in Table 5.1. The first two columns correspond to the inputs as elemental quantity of Ti varies from 0 to 95 at% while Fe, Co, Cr and Ni are kept in equiatomic composition. The other six columns include the output values of each composition.

Following the requirement for HEA solid solution stability established by Guo et al. [5] which combines ΔH_{mix}, ΔS_{mix} and δ, Ti_xFeCoCrNi should form solid solution phases for Ti quantity below 35 at%. However, this quantity is predicted to be reduced to 15 at% if the requirements applied are the ones established by Zhang et al.[4] instead. This fact is mainly due to the restriction proposed on size difference between atoms contained in the system, δ, which has a lower maximum limit in the approach of Zhang than in that of Guo. Nevertheless, both approximations give an indication of the starting point for the formation of HEAs. In addition, VEC could give an idea of the crystalline structure expected to form within the HEA-zone, which would be predicted to be fcc [6].

The prediction method explained in chapter 4 is used here to visualise the possible crystalline structure that the alloy system SUX01 (Ti_xFeCoCrNi) is expected to form. Figure 5.1 shows the relationship between Valence Electron Concentration and Enthalpy of mixing of several alloy systems with addition of the new alloy system SUX01. 5 compositions with different additions of Ti have been calculated (x=0, 5, 10, 15 and 20 at%) and plotted together. It is observed that the alloy without Ti falls completely within the fcc region, and it progresses towards the region of the plot that indicates multiple phases as the amount of Ti increases.

Geometrical design

As mentioned earlier, the new method developed for the processing of different multi-component samples requires the production of several weld tracks. This method of creating a compositional gradient needs the penetration depth for each weld track to be estimated in

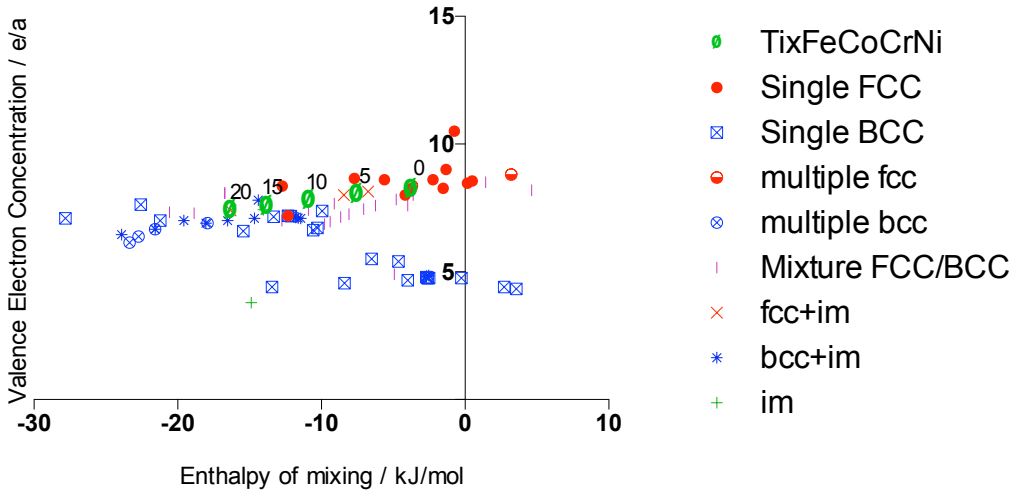

Fig. 5.1 Representation of ΔH_{mix} against VEC including values of $Ti_xFeCoCrNi$.

advance in order to achieve the right composition first time without having to run several additional experimental trials to determine the correct range of beam parameters. The estimation of weld track penetration is carried out for the hypothetical case in which the whole material is composed of pure Ti. The thermal properties of Ti required for the estimation are shown in Table 5.2 and the discussion on the approximation for this hypothesis will be shown later on.

5.3.2 Alloying verification

Melt pool identification

It is well known from electron beam welding how the electron beam parameters can affect the geometry of the melted pool; in particular, current, diameter, velocity and focus position of the beam as well as accelerating voltage; physical properties of the workpiece and the vacuum chamber are also some of the most significant parameters to take into account during welding for the estimation of the weld pool penetration.

For the proposed approach, the key for producing a compositional change between weld tracks is based on varying one operational parameter, the electron beam speed, s_{eb} while keeping the others constant. It consequently affects the weld track penetration depth with deeper weld tracks being formed when the beam is moved more slowly [64, 84].

Figure 5.2 shows the backscattered images, at low and high magnification, of the section

Ti	Cr Fe Co Ni	ΔH_{mix}	ΔS_{mix}	δ	T_m	T_c	VEC
at%	at%	$\frac{kJ}{mol}$	$\frac{J}{molK}$	%	K	K	e/a
95	1.25	-4.14	2.23	3.22	1937	1860	4.2
90	2.5	-7.87	3.85	4.487	1934	2041	4.42
85	3.75	-11.18	5.23	5.38	1931	2132	4.64
80	5	-14.07	6.47	6.07	1926	2175	4.85
75	6.25	-16.55	7.56	6.62	1927	2190	5.05
70	7.5	-18.61	8.54	7.06	1919	2180	5.27
65	8.75	-20.24	9.42	7.4	1917	2150	5.49
60	10	-21.48	10.21	7.67	1912	2105	5.7
55	11.25	-22.3	10.91	7.85	1910	2044	5.9
50	12.5	-22.69	11.53	7.945	1905	1967	6.12
45	13.75	-22.67	12.06	7.96	1903	1878	6.34
40	15	-22.23	12.51	7.9	1898	1777	6.55
35	16.25	-21.38	12.86	7.77	1896	1679	6.75
30	17.5	-20.1	13.15	7.52	1892	1528	6.97
25	18.75	-18.41	13.32	7.17	1889	1383	7.19
20	20	-16.32	13.38	6.68	1886	1220	7.4
15	21.25	-13.79	13.31	6.01	1881	1037	7.6
10	22.5	-10.87	13.07	5.1	1879	830	7.82
5	23.75	-7.52	12.6	3.73	1874	596	8.04
0	25	-3.75	11.52	0.29	1872	324	8.25

Table 5.1 Values of elemental composition as inputs and their respective thermal and electronic parameters as output

across the weld tracks SUX01-02, SUX01-05, SUX01-10 and SUX01-14. Low magnification images show their depth and width in the plane normal to the direction of the electron beam motion, as well as part of the Ti foil and powder not affected by the beam.

SUX01-02 has been designed to be the starting point with the estimated conditions of the electron beam for pure Ti predicting the penetration of the beam to be slightly smaller than the thickness of the foil. This would produce a pure Ti sample.

The consecutive weld tracks are formed using the same electron beam conditions as SUX01-02 but decreasing s_{eb}, and consequently, the beam creates deeper weld tracks that exceed the foil thickness with the objective of melting increasing quantities of the powder with the foil, and then creating alloys.

The compositional change results in a microstructural transformation and this is observed

Thermal conductivity W/mK	Density g/cc	Heat Capacity J/gK
22.0	4.2	0.621

Table 5.2 Thermal properties of titanium at the synthesising temperature $T_0 = 1200$K.

in the high magnification images. SUX01-02 appears to contain a matrix phase composed mainly of Ti with a small amount of segregation of the other elements possibly incorporated due to diffusion between powder and foil. If now we observe the microstructure of SUX01-05, it shows a deeper penetration than SUX01-05 with 3 phases present.

Verification of the number of phases has been carried out in each weld track, using the contrast difference in the backscattered electron images and image analysis as a high throughput method, and a maximum of 3 phases are observed at this magnification. In contrast, Shun et al. [12] observed a simultaneous content of 4 phases in the composition range between 0 and 12 at%, so we surmise that another phase has not been detected due to its small contribution or due to a possible low contrast between phases. However, as simple single phase structures are being sought, this lack of discrimination is not a drawback.

Compositional identification

Chemical analysis has been performed on several samples in order to identify whether the elements are homogeneously distributed in the weld material as well as to identify the elemental composition of the phases present. This would not be as well suited to high throughput analysis as the image based method, but could be employed for more detailed follow up investigations, and here provides verification of the technique. Figure 5.3 shows the elemental distribution on the surface of a portion of SUX01-13. The left side of the pictures corresponds to the area affected by the electron beam showing a portion of the weld track, which is obviously the area containing less porosity and where the five elements, Fe, Co, Cr, Ni and Ti seem to be present and homogeneously distributed. The right side of the pictures is the area where each particle can be easily identified as being composed of one individual element as well as the area with higher porosity in the sample. The microstructure of this area has not been melted and is similar to what would be expected for the as-consolidated sample. This is bonded due to the solid state sintering carried out during the consolidation step, but as the SPS process is rapid, little interdiffusion between the particles has taken place. In addition, EDX analysis has identified titanium, not only in the melted region, but also in the as-consolidated region where (a priori) non presence of Ti was expected. One of

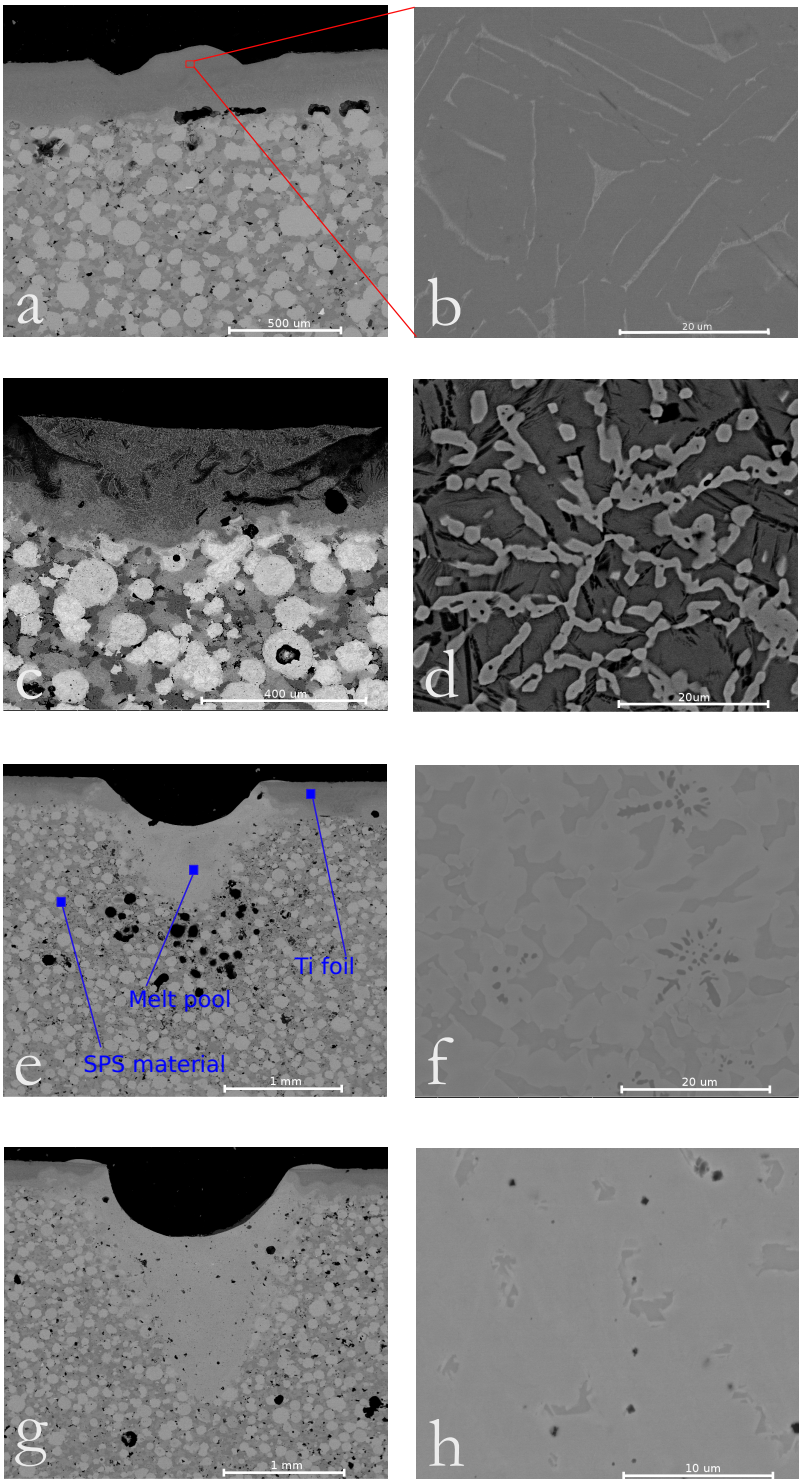

Fig. 5.2 Backscattered images at low and high magnification of weld tracks SUX01-02 (a, b), SUX01-05 (c, d), SUX01-10 (e, f) and SUX01-14 (g, h).

the reasons for this to happen is to capillary infiltration of melted titanium into the porous skeleton produced during SPS [85].

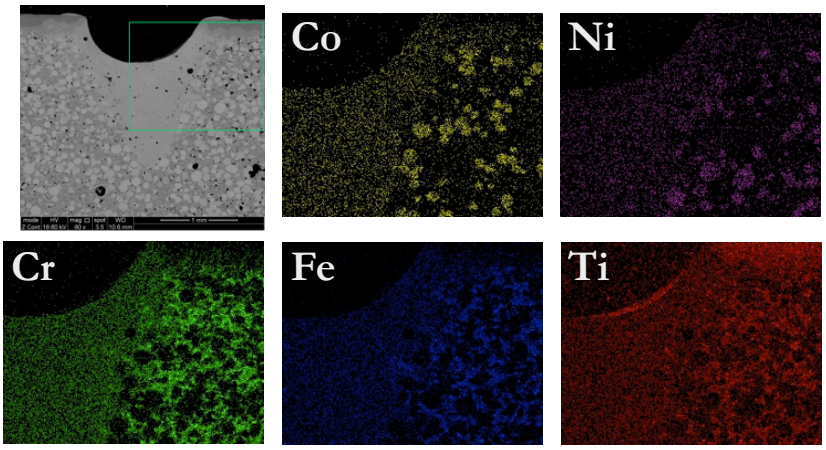

Fig. 5.3 EDX mapping of a portion of SUX01-13 and its surroundings, including the elemental distribution of Co, Ni, Cr, Fe, and Ti.

As shown previously, a maximum of three phases are observed in the image analysis, but to understand what these phases are their composition must be determined. Table 5.3 includes the results of the EDX analysis performed at high magnification on the phases identified in SUX01-03 and SUX01-13.

It is observed that both weld tracks contain a Ti rich phase and a Cr-Fe rich phase, the quantity of which varies with Ti concentration. The presence of a Ti rich phase seems to be due to the fact that when present in high quantity this has not been able to dissolve within the system and it forms a separate phase, incorporating some of the other elements. The Cr-Fe phase may be responsible for the sigma phase as has been shown by other authors [12]. On the other hand, the third phase identified in SUX01-03 as Ti-Ni rich phase seems to undergo a transformation to near equiatomic phase with decreasing Ti levels. It can be explained from the point of view of the enthalpy of mixing when looking at the values for atomic pairs between Fe, Co, Cr, Ni and Ti calculated by Miedema's model [25]. The most negative contribution to the enthalpy of mixing of the system is due to the pair Ti-Ni being $\Delta H_{mix}^{Ti-Ni} = -35 kJ/mol$. When decreasing the quantity of Ti, the contribution of ΔH_{min}^{Ti-Ni} to the entire system decreases too, and therefore the enthalpy of mixing approaches zero, making the formation of a solid solution easier.

ID	Element	Ti rich	(Cr,Fe) rich	(Ti,Ni) rich
SUX01-04	Ti	95.1 ± 3.1	88.7 ± 0.6	70.0 ± 1.6
	Cr	1.0 ± 0.4	4.4 ± 0.7	3.8 ± 2.4
	Fe	0.8 ± 0.3	3.4 ± 0.2	4.7 ± 2.3
	Co	0.4 ± 0.1	1.8 ± 0.2	6.3 ± 0.3
	Ni	0.5 ± 0.1	1.8 ± 0.8	15.1 ± 1.5
ID	Element	Ti rich	(Cr,Fe) rich	(Ti,Ni) rich
SUX01-13	Ti	34.0 ± 3.6	6.5 ± 3.0	13.8 ± 2.8
	Cr	24.1 ± 1.3	27.9 ± 0.7	24.2 ± 0.0
	Fe	18.9 ± 1.5	27.5 ± 0.4	23.4 ± 0.6
	Co	13.1 ± 0.4	19.1 ± 0.7	18.6 ± 0.6
	Ni	9.9 ± 0.4	19.0 ± 0.8	20.1 ± 1.6

Table 5.3 EDX analysis performed at x20000 on three different phases observed in SUX01-03 and SUX01-13.

5.3.3 Identification of High Entropy Alloy phases

Quantitative phase analysis

For the purpose of identifying likely HEA compositions, Quantitative Phase Analysis (QPA) has been carried out by applying image analysis techniques to the microstructures at high magnification in the section across each weld track. Figure 5.4 represents the volume fraction of the 3 distinct phases identified in each weld track. Looking at the evolution of the Ti rich phases, it can be observed that the quantity of these additional phases within the system is reduced when reducing electron beam speed, s_{eb}. For s_{eb} between 1300 and 1000 mm/s, Fe-Cr rich and Ti-Ni rich phases appear. The Fe-Cr rich phase has a maximum contribution of 64 vol% while Ti-Ni rich keeps increasing in volume fraction until it reaches approximately 95 vol% of the microstructure. Furthermore, this phase begins to dominate the whole microstructure for electron beam speeds below 400 mm/s with around 85 vol% Ni-Ti rich phase. This region has therefore been identified as the HEA-zone because of the high probability to find a single phase HEA in this region. Nevertheless, this observation, relying on contrast in the SEM, needs to be verified by determining the crystal structure of the samples contained in the HEA-zone.

Crystal structure

Producing structures in the HEA-zone, SUX01-10, SUX01-11 and SUX01-12 have similar volume fraction of Ni-Ti rich phase (around 85 vol%), although the quantity of Ti differs between them being 44 at% for SUX01-10, 29 at% for SUX01-11 and 17at% for SUX01-12.

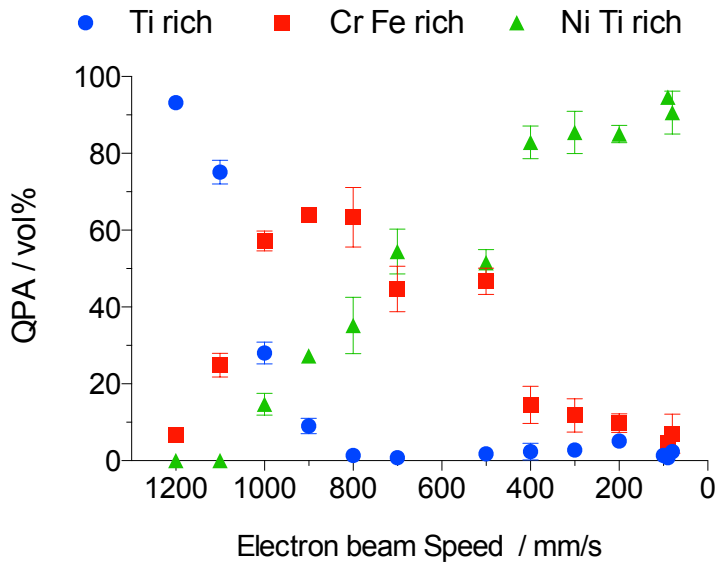

Fig. 5.4 Quantitative phase analysis (QPA) of each weld track. Evolution of the 3 phases identified on each weld track against the electron beam speed, s_{eb}.

In SUX01-14 and SUX01-15 the whole microstructure is dominated by the Ni-Ti rich phase, which makes up more than 95vol% of the structure.

According to these results, alloys where the Ti concentration is above 35at% do not form solid solution phases, (as expected following the approaches of [6] and [69]), and SUX01-10 should therefore be excluded from the HEA-zone. However there is still a region of uncertainty for compositions between those of SUX01-11 and SUX01-12 which requires further examination to verify the crystalline structure formation. Only one composition close to SUX01-14 and SUX01-15 is required for verification due to the similarity in compositions. So three of the alloy compositions were produced by arc melting to provide larger samples, suitable for crystal structure identification.

Table 5.4 includes the composition of these three new samples, with a similar composition to the weld tracks obtained from the chemical analysis results; SUX01-11 and SUX01-12, with aproximately 85 vol% Ti-Ni rich phase and SUX01-15 with around 95 vol% as an example of the structure within what is identified as the HEA-zone.

The X-ray analysis performed on the arc-melted samples is shown in Figure 5.5. After indexing the peaks and looking at the systematic absences, dominant phases with fcc crystal structures are identified in AMSUX01-12 and AMSUX01-15. However, no similar simple

phase can be identified in the trace from AMSUX01-11. Although such an observation can occur if the peaks are obscured by those arising from other phases contained in the sample, it is more likely there is no dominant solid solution found in this alloy, as found from the high throughput tests. The XRD results confirm the presence of a simple fcc crystal structure when Ti content is lower than 20 at%, confirming the range detected in the high throughput method. It is interesting to note that this range is intermediate between the predictions of the two models used suggesting that while they each provide a guideline, neither fully captures the detail of the behaviour in this system.

sample ID	Elements (at%)				
	Ti	Fe	Co	Cr	Ni
AMSUX01-11	32.0 ± 0.3	14.4 ± 0.3	20.1 ± 0.3	14.9 ± 0.2	18.5 ± 0.4
AMSUX01-12	20.8 ± 0.1	14.2 ± 0.1	22.0 ± 0.2	18.9 ± 0.1	24.2 ± 0.3
AMSUX01-15	10.8 ± 0.2	16.8 ± 0.2	26.2 ± 0.2	23.1 ± 0.2	23.1 ± 0.2

Table 5.4 Elemental composition, obtained from the EDX results, of the three samples made by arc melting: SUX01-11, SUX01-12 and SUX01-15.

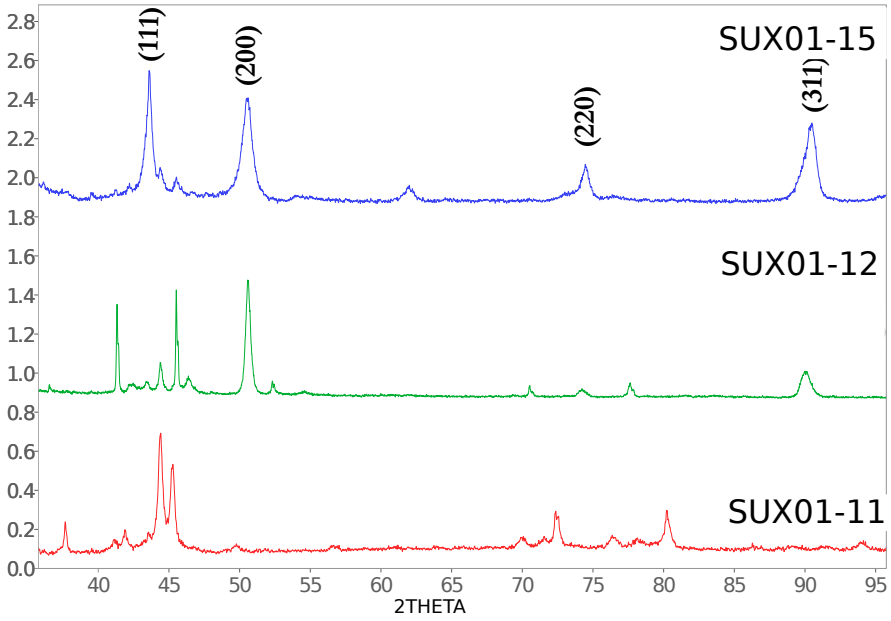

Fig. 5.5 XRD pattern of the arc melted alloys, top to bottom, SUX01-15, SUX01-12 and SUX01-11.

5.3.4 Reproducibility

All of the results already shown are not only relevant for determining the formation of solid solution HEAs, but also to provide a potential tool for exploring the reproducibility and

automation of the processing of this particular alloy system through an EBM route. Figure 5.6 shows the achieved elemental composition (left axis) and both theoretical and actual depth (right axis) of each weld track depending on the s_{eb} applied. For the highest s_{eb}, the beam reaches the smallest depth melting only material at the surface, which corresponds to the Ti foil, and gives rise to an alloy of 100 at% Ti. With decreasing speed, the depth of the weld track increases so a larger quantity of powder is melted together with Ti in the weld track; furthermore, the quantity of the other four elements remains in a near equiatomic ratio for each weld track, indicating that the powders are well mixed and a good approximation to the designed alloy is achieved. In addition, the difference between estimated and actual penetration for each weld track shows the smallest values for weld tracks close to the surface because of the assumption used for the prediction that the whole sample is composed of Ti; as s_{eb} decreases, the composition change increases the difference between actual and theoretical depth.

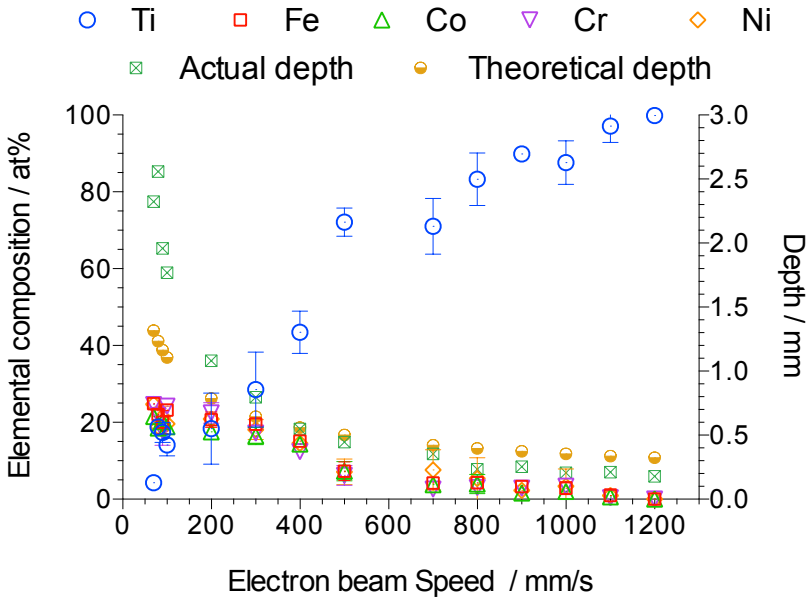

Fig. 5.6 Reproducibility and automation of processing showing: on the left axis, elemental composition of Ti, Cr, Fe, Co and Ni; on the right axis, depth values estimated from the Rosenthal equation (theoretical) and depth calculated on the section across the weld tracks (actual) against speed of the electron beam, S_{EB}.

5.3.5 Mechanical properties

Where a high throughput processing method is achieved, screening results for particular properties of interest requires high throughput test methods. As an example of this, auto-

mated hardness testing has been applied to the sectioned samples. Figure 5.7 shows hardness average (based on 11 indents) against Ti quantity for Ti_xFeCoCrNi produced by different methods: (1) on the section across the weld tracks, (2) on the three samples produced by arc melting and (3) arc melted results from the literature for the same system presented by Shun et al. [12]. Higher variance is observed in both composition and hardness in the weld tracks than in the arc melted samples, which could be due not only to a possible small compositional heterogeneity found across some of the weld tracks, but also to the fact that the other four elements (Fe, Co, Cr or Ni) are not always found to be present in exactly equiatomic ratio and therefore a small addition or deduction of any of these elements could significantly affect the mechanical properties, and thus affect the hardness values.

Across the full range of tested compositions the hardness change is considerable, from a minimum around 348HV for 5 at% Ti (which corresponds to the weld track with the maximum quantity of fcc crystalline structure) passing through an absolute maximum above 956HV for 19 at% Ti, to a local minimum of 517HV for 97 at% Ti. The new hardness values obtained from the arc melted samples are in excellent agreement with those presented by Shun et al. [12] up to the maximum value they reported, 32 at% Ti. Due to the lack of experimental hardness data for the alloy with Ti content higher than 32 at%, it is supposed that the trend that would be followed would be similar to the one already obtained for the weld tracks, presenting its maximum hardness value close to the arc melted samples with 32 at% Ti (1021HV).

5.4 Summary

In summary, here for the first time a high throughput technique for synthesis of HEAs has been reported. The technique consists of the creation of several weld tracks on a specimen composed of a mixture of elemental powders and a foil and the screening of phases present in the final microstructures through a quantitative phase analysis step performed by image analysis methods. The time required for design, processing and characterization and testing of 16 weld tracks using the method and equipment described here has been estimated to be 24 hours; this could potentially be cut further by more bespoke equipment for the process and further automation.

The validation of the proposed high throughput procedure has been carried out using the system Ti_xFeCoCrNi. It shows a good correlation between the compositional results obtained by design and the compositional results obtained experimentally where the target is based on

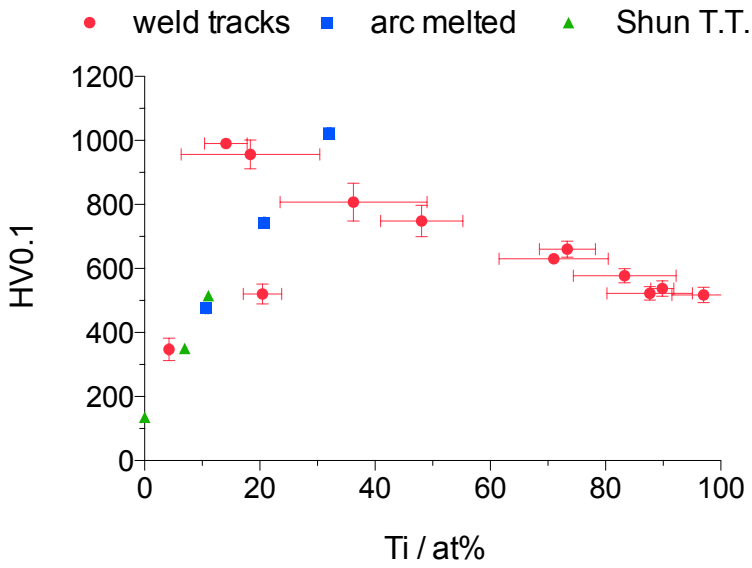

Fig. 5.7 Hardness of TixFeCoCrNi in the section across each weld track and the results obtained for the arc melted specimens combined with other values already calculated by [12].

the change of Ti quantity while Fe, Co, Cr and Ni are kept in equiatomic ratios. Furthermore, the screening analysis method introduced helps to observe the microstructural evolution through the weld track and then determine whether the microstructure is dominated by one single phase or multiple phases. Hardness testing has also been carried out and a HV trend has been observed in this particular alloy system with a maximum hardness close to 1000HV when the level of Ti reaches 19 at%.

The developed methodology has provided excellent results on 16 weld tracks or, equivalently, 16 different samples and this technique is still open to possible modifications in order to reach a larger number of samples in the equivalent time.

Chapter 6

Discovery of novel multicomponent high entropy alloys

Chapter 4 and 5 have shown how to use computational and experimental tools for speeding up the discovery of multicomponent high entropy alloys. The approach followed in chapter 4 has allowed the discovery of 3 novel quaternary metallic systems (two HEAs composed of single phases: MnFeCoNi, TiVMnNb and one system containing multiple phases: TiMnFeNi) during the validation of the prediction stage using Principal Component Analysis. In chapter 5, the methodology has been validated with the production and characterization of the alloy system $Ti_xCrFeCoNi$.

The composition produced by SPS and EBW would be analysed, and posteriorly, the observed data would be stored in a virtual library containing observations of all the produced alloys. Hence, PCA could be used as a "feedback" method in the combinatorial approach, exploring a dataset of HEAs with their properties in order to visualise patterns and trends within the studied space. In this sence, PCA helps to decide the right composition according to the desired properties while reducing time consuming and money.

The current chapter will be split in two different sections: (1) the discovery of novel alloy systems, focused on refractory metals, through the high throughput methodology and (2) the discovery of novel alloys systems by using purely Spark Plasma Sintering. Following the novel high throughput route, three novel alloy systems have been synthesised and their hardness has been measured. Further to this, following solid state sintering through Spark Plasma Sintering, the well-known HEA CrFeCoNi has been produced in order to explore the possibility of synthesising HEAs directly by this route.

6.1 Combinatorial High Throughput Processing Technique Applied to Refractory High Entropy Alloys

6.1.1 Introduction

In the light of the recent discoveries concerning High Entropy Alloys, discussed throughout this thesis, it can be concluded that traditional alloys are composed of one principal element because the centre of multi-component (ternary and higher order) phase diagrams has in most cases not been adequately explored, and there are compositions with great potential in addition to the known metallic alloys. For example, the Aerospace and Nuclear industries require metallic alloys with superior structural and functional properties, and specific application requirements such as compatibility of the structural materials with the nuclear reactor environment. Some typical specifications of desirable materials include: operating temperature range between 1100 and 1400 K, Young's modulus > 2GPa, long term thermal creep strength, low ductile-to-brittle transition temperature, good joining through welding and brazing, and low density [86].

Currently, the scientific community has the opportunity to find the most suitable material within HEAs for a potential application in any of those industries using combinatorial methods that reduce cost, time and effort consumed. This chapter puts to the test the methodology developed with the exploration of several new multicomponent alloy systems.

The combination of the predictive approach (chapter 4) and the high-throughput synthesis of HEAs (chapter 5) is used here for the discovery of unknown HEAs in these systems.

6.1.2 Experimental techniques

Three novel alloys have been synthesised through SPS prior to EBM. The alloy systems are V_xTiMnNb, Zr_xTiNbHf and Ti_xHfTaWRe which are identified as SUX02, SUX03 and SUX04 respectively.

The systems SUX03 and SUX04 are composed of elemental powders (Ti, Nb and Hf for SUX03 and Hf, Ta, W and Re for SUX04) and a thin metallic sheet composed of high purity Zr (in the case of SUX03) or Ti (in the case of SUX04). SUX02 is entirely composed of elemental powders (V, Ti, Mn and Nb) with one of them (V) being pre-compacted to form a thin foil. Further details on the composition of each system are shown in Table 3.3 while the processing parameters are collected in Table 3.5 and Table 3.6.

The final samples have been prepared (following the general guidelines for grinding and polishing described in Table 3.7) for both optical and Scanning Electro Microscopy and for hardness testing. Quantitative Phase Analysis, QPA, has been carried out following the steps included in Table 3.8.

6.1.3 Results and discussion

Prediction of High Entropy Alloys

Firstly, the elements considered to make up the candidate systems should be capable of being manipulated safety and are chosen with the intention of creation an alloy with utility for the types of applications discussed above. High temperature and strength during service are some of the requirements that the novel alloy system should meet if it is required for a potential application in the aerospace or nuclear industry, so metals such as those within the refractory elements, whose crystalline structure is a body-centered cubic (which in general has an improved resistance to radiation damage due to the absence of stable stacking faults) show signs of being the most suitable elements to choose as a starting point.

The predictive approach introduced in chapter 4 is used here for the design of the new metallic systems. The enthalpy of mixing (ΔH_{mix}), the atomic size difference (δ) and the valence electron concentration (VEC) of SUX02, SUX03 and SUX04 for several quantities of the varying element, Ti, V and Zr are calculated using the equations 2.4 for ΔH_{mix}, 2.5 for δ and 2.7 for VEC (described in chapter 2). The resultant values are then plotted within the already known HEAs as shown in Figure 6.1.

The three novel alloy systems are located and spread out in the regions with known HEAs. The HEAs forming single fcc are alloys composed of transition metals of the 3d series, whereas those alloys forming single bcc are composed of transition metals of the 4d and 5d series. It is observed in Figure 6.1 that V_xTiMnNb and Zr_xTiNbHf (SUX02 and SUX03 respectively) are located in the region where HEAs composed of transition metals of the 4d and 5d series, whereas Ti_xHfTaWRe (SUX04) is spread between the 4d single bcc and the multiphase region with changing quantity of Ti. This prediction indicates that SUX02 and SUX03 would form a single bcc phase with any percentage of the added element (vanadium or zirconium). It also indicates that when increasing the amount of Ti in SUX04, the expected set of conditions reaches the region of multiple phases, which means that the formation of multiple phases would be expected at high concentration of Ti, although simple bcc phases

may possibly be found at low concentrations.

At this stage, the candidate components forming a bcc HEA have been chosen and the synthesis of the novel material can commence.

Synthesis and characterization of the alloy SUX02, V-TiNbMn

In this case, the conditions of the foil are slightly different to those described in chapter 5: (1) it is composed of Vanadium instead of Titanium; (2) it has been produced by powder consolidation through SPS instead of using a commercial sheet composed of a high purity metallic element; and (3) as a result of this processing method, its thickness is much greater than that of the foil used for SUX01. (Table 3.3 shows the features of the elements used in each system).

The technique offers the possibility of using a wide range of elements as the foil, increasing the feasibility of using the combinatorial high throughput technique to a wider combination of elements. In addition, the production of a foil from alternative sources could result in a reduction of the processing cost, and also the production of thicker foils could allow for deeper weld tracks, and therefore increase the number of testing techniques suitable for the combinatorial approach. These reasons led to the decision to modify the starting conditions of the material, however it will be shown that also has the effect of increasing the difficulty associated with the processing stage.

The foil thickness is about 1.5 mm, 5 times thicker than that used in SUX01. As a consequence, higher electron beam energy is required to cause complete melting through the foil. This energy increment is achieved by modifying the operational parameters, such as the power and speed of the electron beam.

For the production of deeper weld tracks, the electron beam speed range is kept between 70 and 1300 mm/s (the same as that one used for SUX01), whereas greater power is employed (using the same voltage, 60kV and increasing the beam current). The full set of operational parameters is collected in Table 3.5.

This power increment is the cause of the deeper penetration of the electron beam heating into the workpiece. During the welding, a cavity is created and will remain open if the pressure of the molten material against the walls of the cavity is lower than the vapour pressure generated in the hole. Hence, an undesirable open shape, penetrating down into the

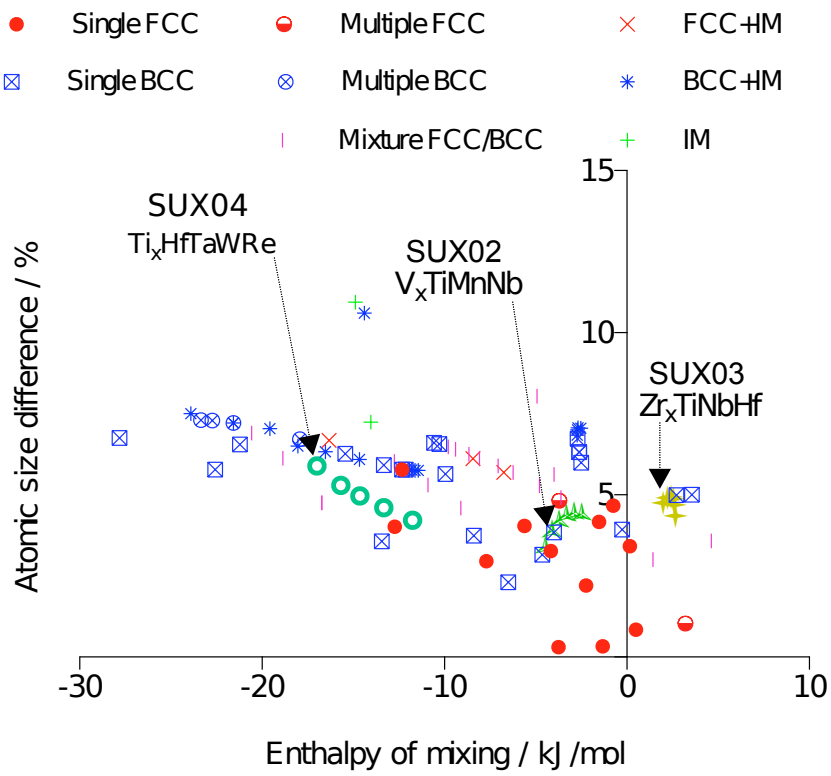

(a)

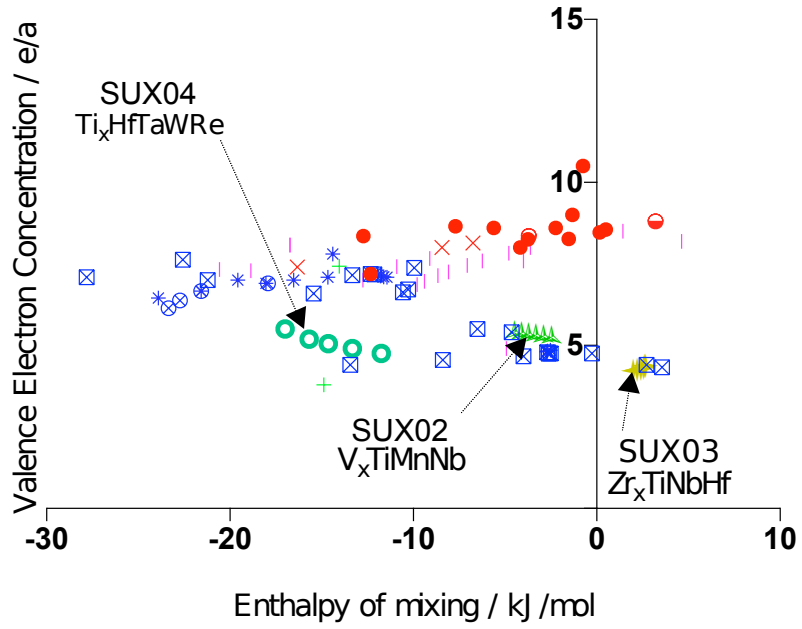

(b)

Fig. 6.1 (a) ΔH_{mix} against δ (b) ΔH_{mix} against VEC mapping HEAs while overlapping the predicted data (SUX02, SUX03 and SUX04) with the experimental values.

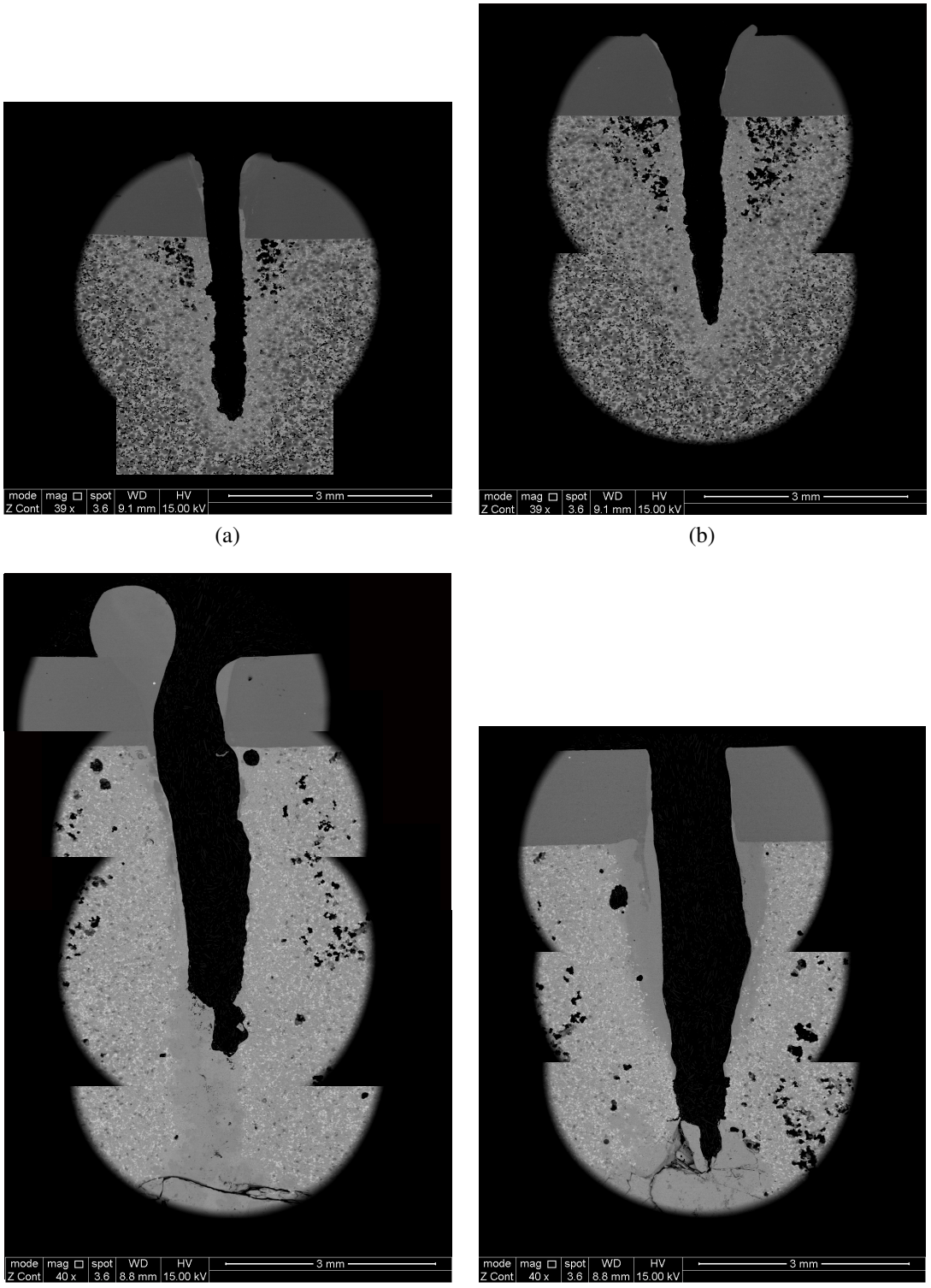

Fig. 6.2 Low magnification backscattered images of the section across the weld tracks: (a) SUX02-09, (b) SUX02-10, (c) SUX02-13 and (d) SUX02-14.

material, known as the keyhole will remain in the weld tracks. Evaporation of any of the elements could be a contributing factor to the formation of a keyhole as introduced in chapter 2.

This keyhole effect is observed in each weld track performed on the system SUX02, as seen in Figure 6.2 where a clear keyhole (approximately 3-6mm deep) is present. As the boiling point of manganese is lower than the melting point of niobium, manganese evaporation could have occurred, which could contribute to some extent to the formation of the keyhole.

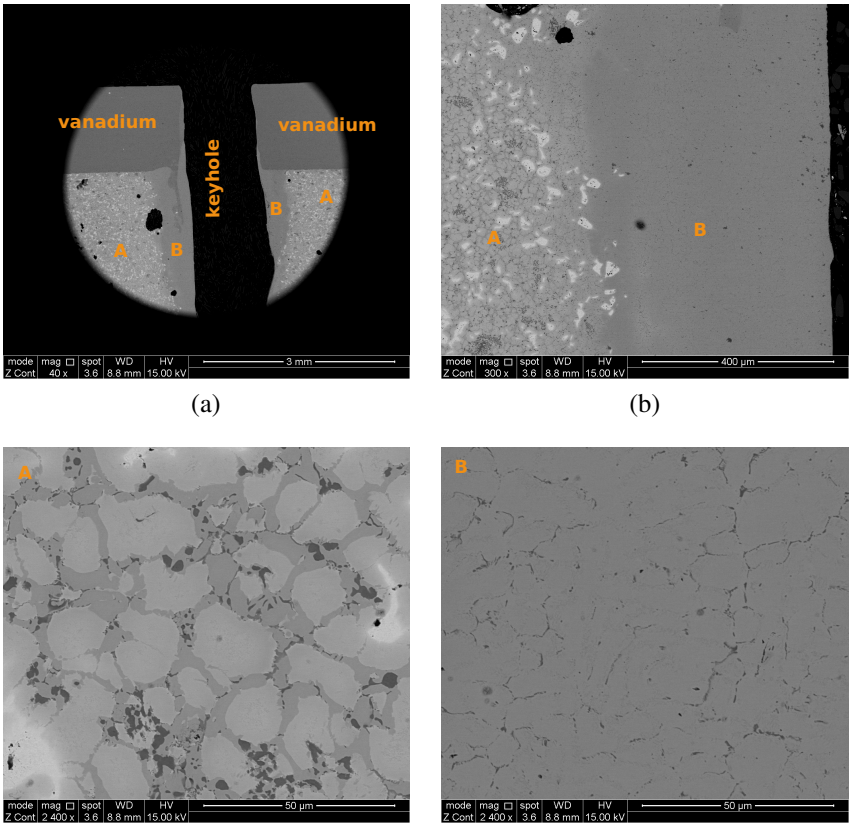

(a) (b)

(c) (d)

Fig. 6.3 Backscattered images of the section across the weld track SUX02-13.

High magnification backscattered images of the section across the weld tracks have been taken in order to characterise their microstructure in more detail.

Each weld track contains the same features, and one (SUX02-13) will be described here

(shown in Figure 6.3) as a reference. As observed in Figure 6.3a , 4 different regions are visible; the vanadium foil on top of the weld track, the deep keyhole in the middle and another 2 regions identified as A and B, symmetrically found on both sides of the weld track. The interface between region A and B is observed in Figure 6.3b while images taken at higher magnification show these two regions separately in Figures 6.3c and 6.3d. It can be seen that region A contains segregation of some elements as well as the presence of multiple phases, whereas in region B, one single phase is observed.

It would be quite tempting to identify region B as the HEA due to its apparent simplicity, however the heterogeneity in region A and the presence of the keyhole and the discontinuity distribution of region B creates a certain doubt about the reliability of such a conclusion. Due to this, determination of the elemental composition of the phases present would be needed, obtained by the performance of a chemical analysis, EDX.

Figure 6.4 includes the elemental mapping results performed in an area of region A over a period of 30 minutes at low magnifications in SUX02-14. Vanadium is found to be homogeneously distributed while niobium has not completely diffused into the system and titanium and magnesium have segregated separately.

Incomplete diffusion of Nb into the system could be explained if the welding temperature has not exceeded the melting point of Nb. Irrespective of this possible effect, the wide range of melting temperatures presented by the elements used in the system (from 1590 to 2750 K) provokes segregation of Mn and Ti.

Quantitative chemical analysis has also been performed in regions A and B in SUX02-14, the results of which are shown in Table 6.1. Spectra s1, s2 and s3 correspond to three different areas of region A (see Figure 6.5 while s4 corresponds to region B (see Figure 6.3d). Spectrum s1 has been taken in a particle of pure Nb, s2 has been taken in the area around the Nb particles and s3 has been taken in the area of Mn segregation. Spectrum s4 shows that the region B is composed of a V-rich phase. Besides, it does not show evidence of the equiatomic contribution of the other three elements into the system.

Hardness testing When performing a visual inspection of the microstructure, it is obvious that there is no evidence of microstructural simplicity to be found under these processing conditions, and therefore the simple screening technique used to discriminate the formation of several phases is not available here. However, hardness can still be used as a high throughput

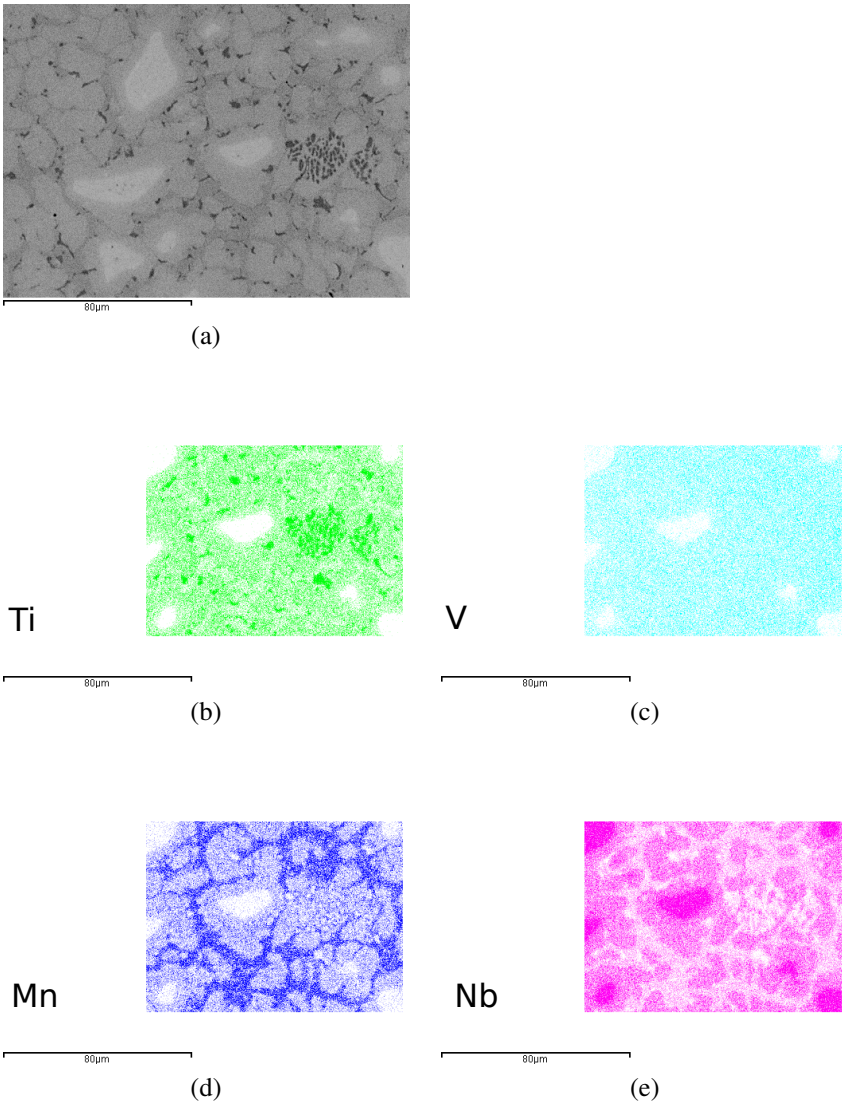

Fig. 6.4 EDX mapping of the area with multiple phases in specimen SUX02-14.

Spectrum	Ti	V	Mn	Nb
s1	0	0	0	100
s2	33.62	4.60	21.81	39.97
s3	24.57	4.77	52.22	18.43
s4(single phase)	9.76	72.27	2.82	13.51

Table 6.1 EDX quantitative analysis of three different areas on SUX03-14.

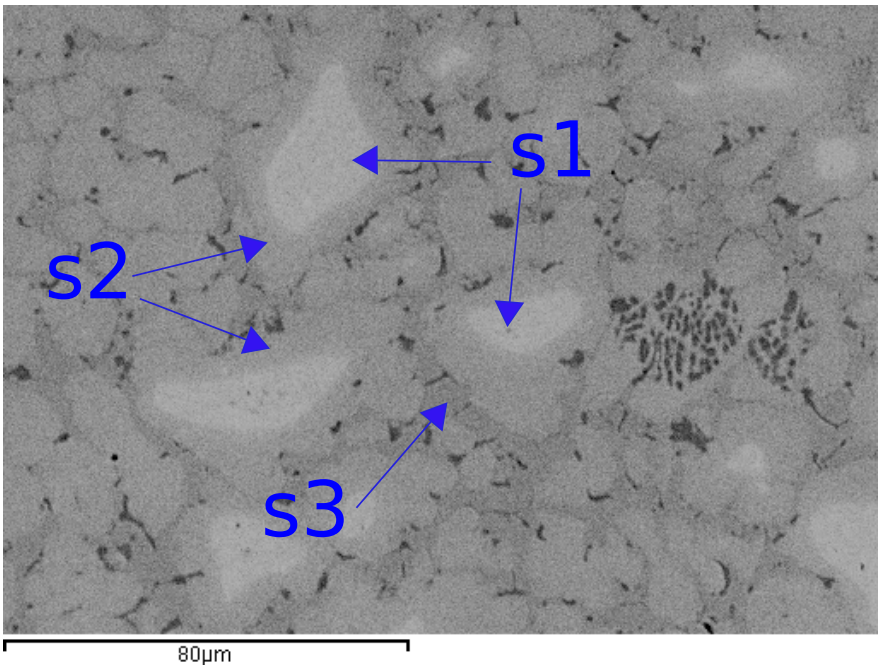

Fig. 6.5 Backscattered image of SUX02-14.

testing tool and it has been performed on the section across some of the weld tracks.

Figure 6.6 shows the hardness of some weld tracks according to the electron beam speed. At high speeds, the electron beam does not overpass the foil, what means that the weld track is mostly composed of vanadium. As the speed decreases, the amount of the base material (Ti, Nb, Mn) welded together with the foil (V) increases, and therefore, the hardness changes, reaching around 800HV. This high value would be expected for a microstructure containing multiple phases, potentially including intermetallics. It also shows a wide deviation in the values of hardness, which may be due to the presence of the different regions (s1, s2, s3 and s4) and their individual hardness differences.

Summary of SUX02

The alloy system $V_xTiMnNb$ has been designed by using the PCA results observed in chapter 4, and it has been predicted to show a single bcc crystalline structure for any level of the vanadium addition. As a reference, in chapter 4, the equiatomic alloy VTiMnNb has already been characterised as a body centered cubic structure.

For the production of the specimen, the thickness of the foil was around 5 times the thickness

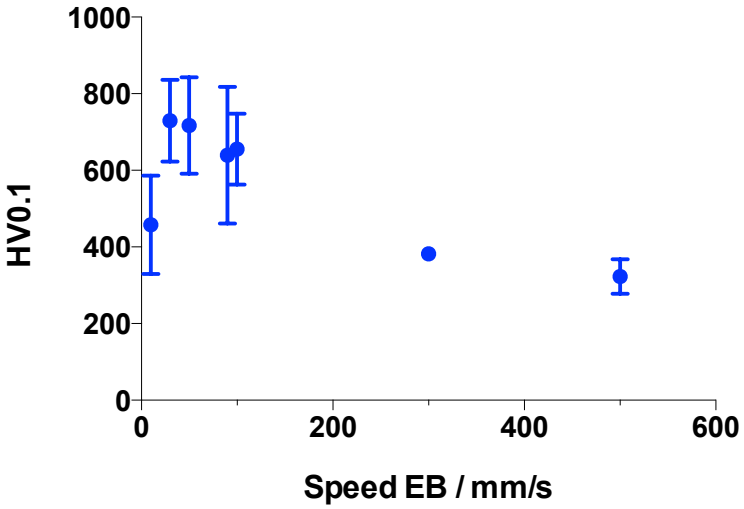

Fig. 6.6 Hardness testing on the section across some weld tracks produced within SUX02.

of the foil used in chapter 5. Consequently, a stronger power beam is required to melt through the foil and to obtain allowing with the material sitting below it. However, in this case, due to the high beam power needed, a keyhole has been created in the weld tracks and has led to unclear variations in microstructure in the samples, making the performance of the screening test impossible.

Although determination of the characteristics of the alloys that would allow their classification as HEAs has not been possible under these operational conditions, hardness testing has allowed the measurement of HV in the weld tracks, where a maximum of 800HV has been reached. After these observations, reduction of the foil thickness has been proposed for future work in order to observe the opposite limitations in geometrical design. At this stage, it needs to be clarified that the interest on understanding the behaviour of many metallic elements when using the technique developed here (as seen in chapter 5), the synthesis of SUX02 has not been carried out under conditions of thinner foil, but an alloy system composed of other refractory elements.

Synthesis and characterization of SUX03, Zr-TiNbHf

The crystalline structure of the novel alloy system has been predicted by using the PCA results obtained from chapter 4. Figure 6.1 includes the calculated values of the enthalpy of mixing, the atomic size difference and the valence electron concentration of the alloy system $Zr_xTiNbHf$. As observed in the figure, the markers of SUX03 sit in the region where the single body-centered cubic HEAs are observed and SUX03 is therefore expected to form a

single bcc phase. Validation of this can be attempted in the production stage.

During the consolidation of the specimen by SPS, a protective layer of graphite is attached to the moulds, and some superficial contamination of the sample needs to be carefully removed. An efficient but also slow method is by grinding it off until a completely clean surface is observed. A faster technique to remove the graphite is by employing a powerful sand blaster, which would completely remove not only the graphite but also a superficial part of the actual sample. This latter method was used here, on a sample where 14 weld tracks have been produced using the operational parameters collected in Table 3.6 which were then characterised and tested.

The images of the section across several weld tracks are collected in Figure 6.8. From the top to the bottom in the images, the electron beam speed increases. It is observed that. as expected, the weld track depth increases as the electron beam speed decreases. This fact can be observed through the depth evolution in the low magnification images (a), (c), (e) and (g).

In the images, the thickness of the Zr foil can be easily distinguished, which ideally should be equal for every weld track. However, it is observed that some parts of the Zr foil have been removed together with the remaining graphite due to the power of the sand blaster which has in places reduced the thickness of or removed entirely the Zr foil layer, as well as the residue of carbon, which was the intended target.

The backscattered images show a high contrast between particles due to the effect of the atomic number where the brightest particles or phases correspond to the ones with highest atomic number [87]. Hence, the brightest and darkest particles in these images correspond to Nb and Ti respectively.

Images b, d, f and h in Figure 6.8 correspond to the high magnification backscattered images taken on some areas of the melted pool of the weld tracks SUX03-01 (Figure 6.7b), -03 (Figure 6.7d), -06 (Figure 6.8b) and -16 (Figure 6.8d). Weld track SUX03-01 contains a heterogeneous melted material, while the heterogeneity seems to be decreasing for deeper weld tracks, as seen in SUX03-16.

Hardness testing has been performed in the section across the weld tracks. The results are shown in Figure 6.9a where hardness values vary within a narrow HV range between 300 and 420 without any aparently systematic trends.

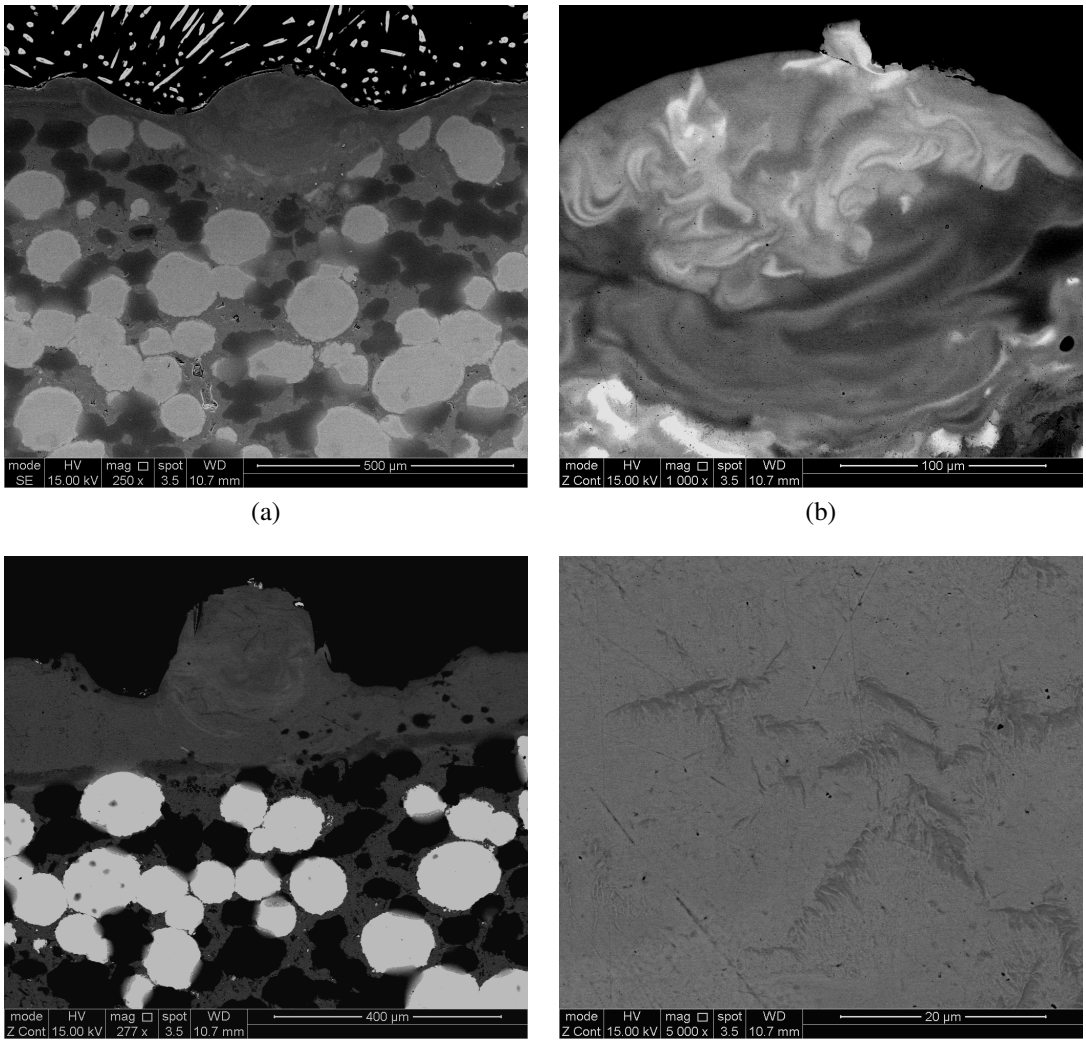

(a) (b)

(c) (d)

Fig. 6.7 Scanning Electron Microscopy images of the section across the weld tracks SUX03-01 (a and b), SUX03-03 (c and d).

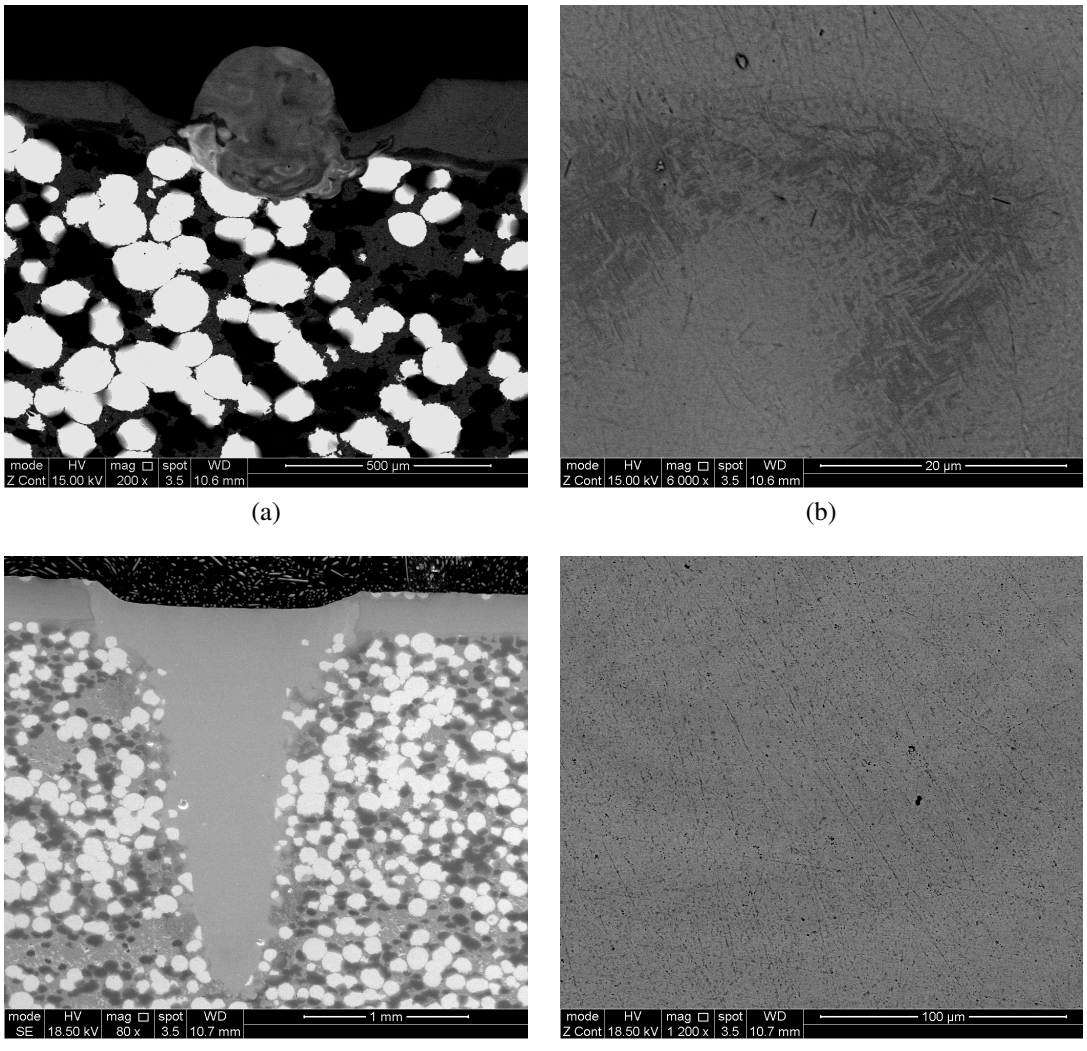

(a) (b)

(c) (d)

Fig. 6.8 Scanning Electron Microscopy images of the section across the weld tracks SUX03-06 (a and b) and SUX03-16 (c and d).

Summary of SUX03

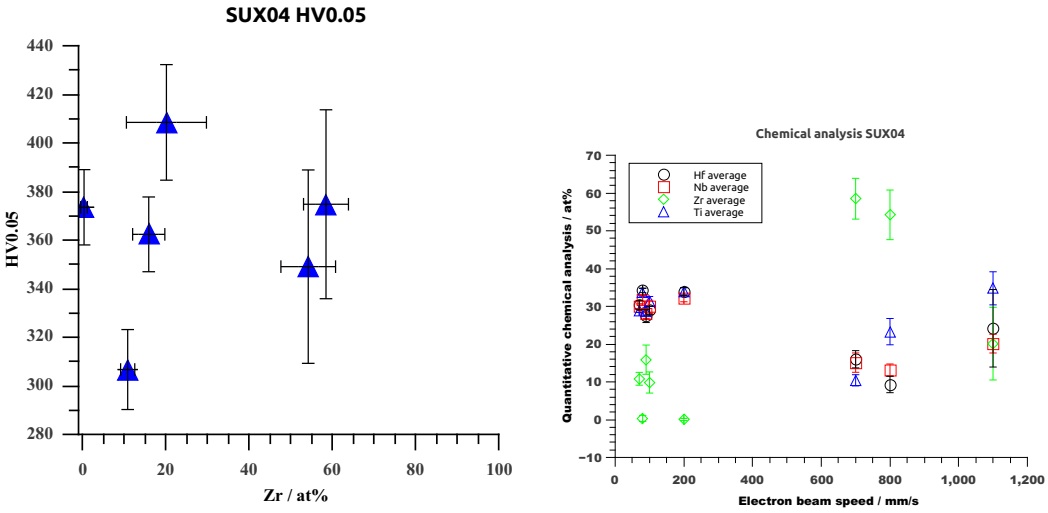

(a) (b)

Fig. 6.9 (a) Hardness testing of the weld tracks with varying Zr content, (b) Elemental chemical analysis performed on several weld tracks

SUX03 has been designed to form a body centered cubic structure. Examination of the sample shows well-shaped weld tracks, however, there are non-systematic variations that make the screening technique not unable to be used for this sample. Nevertheless, hardness has been performed on the weld tracks and found to vary between 300 and 420 HV.

The use of a sand blaster for removing the remaining graphite adhering to the sample surface was selected to decrease the time required for preparation of samples, however, this has resulted in the removal of some of the Zr foil and non-systematic alloy formation. This means that this cleaning technique is not appropriate, and therefore traditional rough grinding would be the ideal graphite removing procedure.

Synthesis and characterization of the alloy SUX04, Ti-HfTaWRe

As seen in Figure 6.1, the prediction of the crystalline structure indicates that the quantity of Ti can strongly affect the final crystalline structure of the HfTaWRe system (designated SUX04) and therefore also change the microstructure and properties.

Figure 6.1 shows the theoretical values (enthalpy of mixing, atomic size difference and

valence electron concentration) of a series of alloys from the system SUX04 with different amounts of Ti. Ti addition decreases the enthalpy of mixing from -10 to -20kJ/mol and increases the atomic size difference. However the valence electron concentration is less sensitive to Ti quantity.

14 weld tracks have been synthesised by using the operational parameters collected in Table 3.6. In this case, unlike for SUX03, the remaining graphite on the samples after the SPS stage was removed by using the conventional (and slow) route, grinding it off with coarse SiC grinding paper such as x120 or even better x80.

High magnification backscattered Scanning Electron Microscope images have been taken for performing phase quantification, while low magnification ones are required for determining the penetration of the electron beam into the weld tracks. The backscattered images of three weld tracks as examples are shown in Figure 6.10.

As in previous instances of the method reported earlier in this thesis, changing the electron beam speed, changes the weld track depth. Hence, the composition changes and the microstructures of the alloys in the different weld tracks are therefore slightly different.

The main difference between each weld track is the quantity of titanium in the system, which is directly dependant on the penetration depth of the electron beam into the workpiece. Figure 6.10 contains the common types of microstructures found in each weld track. Three different kinds of microstructures have been observed after solidification:

- SUX04-01 has been processed at the highest electron beam speed. As observed in the low magnification image, the beam only just penetrates the Ti foil and therefore this specimen should be composed of mostly titanium with small amounts of W, Re, Hf and Ta. The final microstructure seems to be formed of a matrix and non lamellar structure similar to that which is characteristic of a bainitic transformation in non ferrous materials [88].

- SUX04-06 has been processed at lower electron beam speed than SUX04-01 and consequently, the beam passed through the Ti foil, increasing the quantity of the powder elements combined into the specimen (see low magnification image in the middle of Figure 6.10). A grain boundary is observed in the high magnification image and some acicular structures growing inside the grain, similar to those typical of a martensite transformation (for example shown on page 175 in [88]).

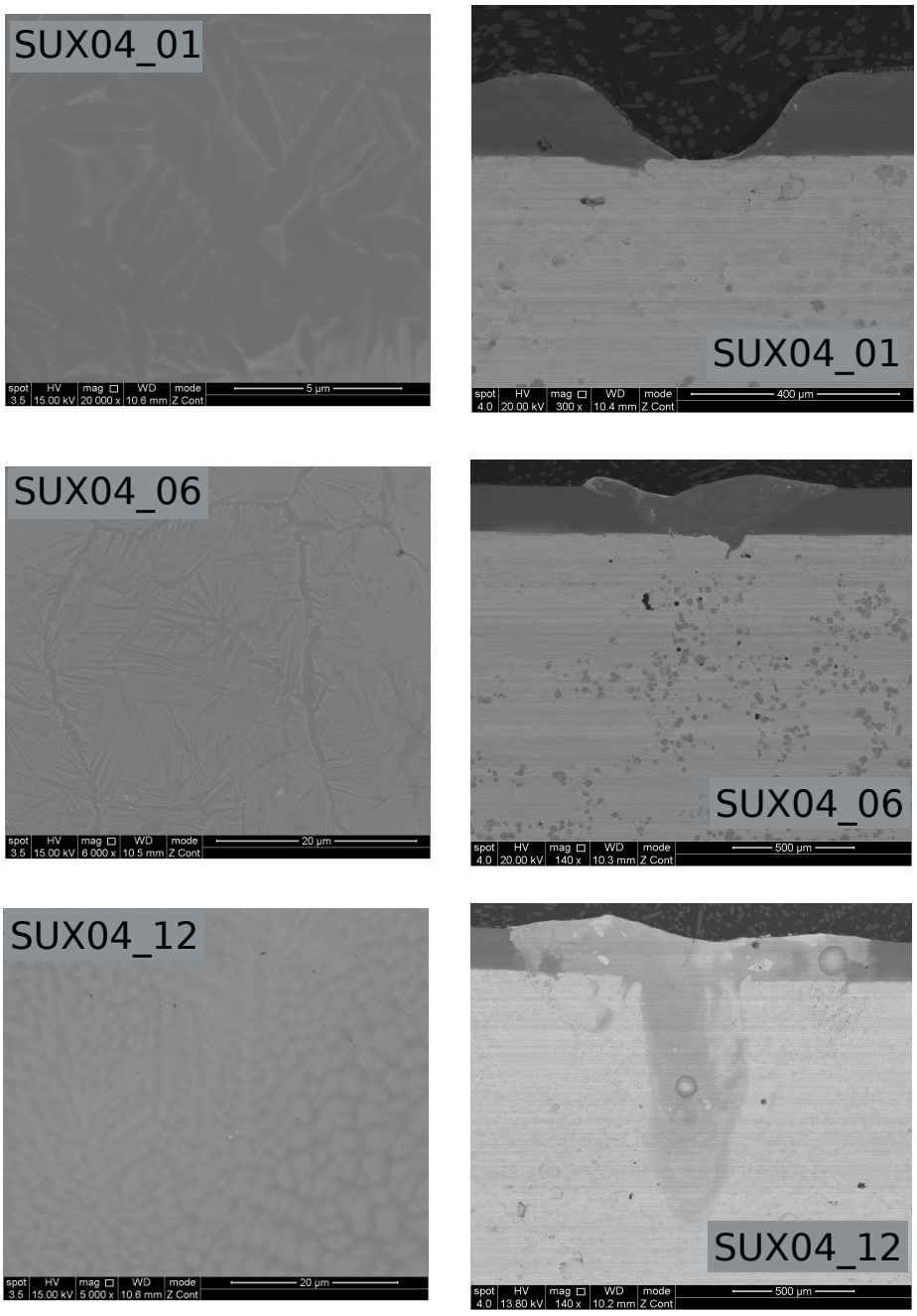

Fig. 6.10 High (on the left) and low (on the right) magnification backscattered images of weld tracks SUX04-01 (top), SUX04-06 (middle) and SUX04-12 (bottom).

- SUX04-12 has been processed at the lowest electron beam speed and the beam has therefore reached the deepest penetration of all the weld tracks in this experiment. The high magnification microstructure shows a dentritic structure typical of solidification [89].

Looking at each of the high magnification backscattered images, the different contrast can be an indicator of the possible different elemental compositions, and therefore the different phases present.

On this basis, quantitative phase analysis, QPA (used for validation of the technique in chapter 5) is implemented here to verify the volume fraction of each phase included in each weld track, as well as to further develop the screening technique which helps to determine whether a single phase HEA is being formed.

As far as can be observed in the high magnification backscattered images, each weld track is mainly composed of only 2 phases while their quantity varies. The volume percentage of each phase in each weld track has been determined, following the protocol outlined in Table 3.8, in order to understand the microstructural evolution, which is summarised in the graph presented in Figure 6.11.

It has been assumed that one of the phases contains the larger quantity of Ti and has been named as "Ti-rich phase". The other phase has been named as "equiatomic phase" assuming that this phase is formed at low levels of Ti. In Figure 6.11, the Ti-rich phase decreases while the equiatomic phase comes to dominate the observed structure in this system up to almost 80 vol% when employing low electron beam speed and producing relatively titanium-poor alloys. According to these quantitative results and the type of microstructure formed by dendritic and interdendritic regions (see SUX04-12 in Figure 6.10), it is more than likely that simple single phases HEAs are obtained in the system SUX04 produced at electron beam speed lower than 500mm/s, corresponding to the lowest levels of titanium below 20 at%. If further testing is required, after mapping this alloy system, chemical analysis would be carried out on the alloys of interest instead of on each one. In this way, time consumed would be reduced.

Mechanical testing Hardness testing has been performed in the middle of the cross section of the weld tracks. The hardness evolution with the electron beam speed has been plotted in Figure 6.12. Weld tracks produced at electron beam speeds higher than 300 mm/s reach a roughly constant hardness value around 500HV, still higher than the hardness of pure

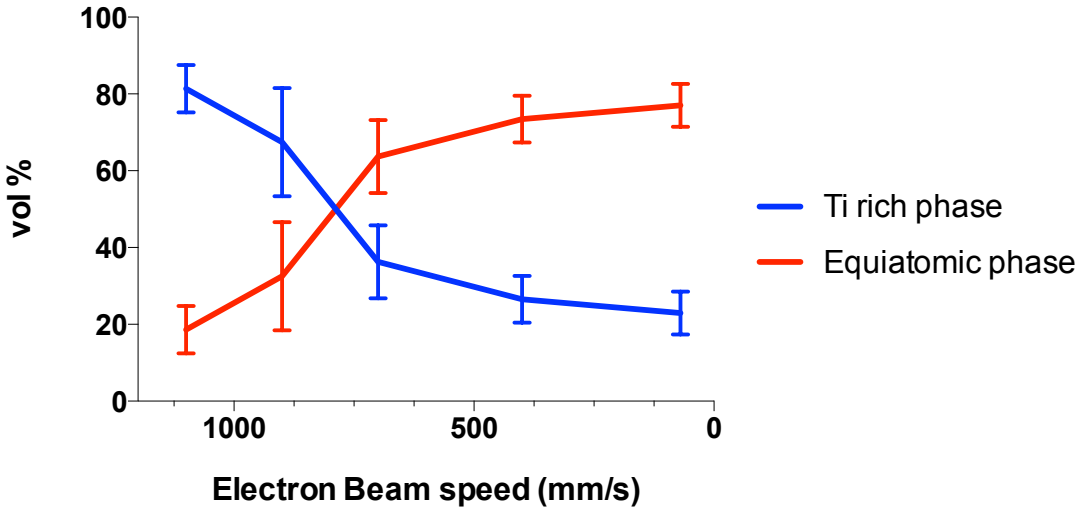

Fig. 6.11 Quantitative Phase Analysis results for alloy SUX04. Determination of the quantity of each phase found in each weld track according to the synthesis parameter, electron beam speed. As seen in Figure 6.1, this alloy system is located below the region where multiple phases are found, and it approaches the area where HEAs 4d-series with decreasing Ti contain.

titanium due to the additions of small amounts of the allowing elements W, Ta, Re and Hf. The weld tracks produced at lower speeds, where the amount of Ti is lower and simple phase HEA can be formed, reaches a much higher hardness values. The average of the lowest speed exceeds 1000HV.

6.2 Solid state alloying of High Entropy Alloys from powder

6.2.1 Introduction

High Entropy Alloys have been widely produced by liquid state methods (e.g. arc melting, laser melting). In a few cases, HEAs have been obtained under solid state conditions by mechanical alloying followed by SPS consolidation. In this case, the whole process required around 30-60 hours for successful mechanical alloying followed by about 15 minutes for SPS consolidation[35–37, 90]. The mechanical alloying stage is therefore clearly the bottleneck in the process that would impose limits on practical production of components form such alloys. Yet SPS can be an attractive process for powder metallurgy, due to the speed and the potential capability to produce certain basic shapes without the need for gurther processing

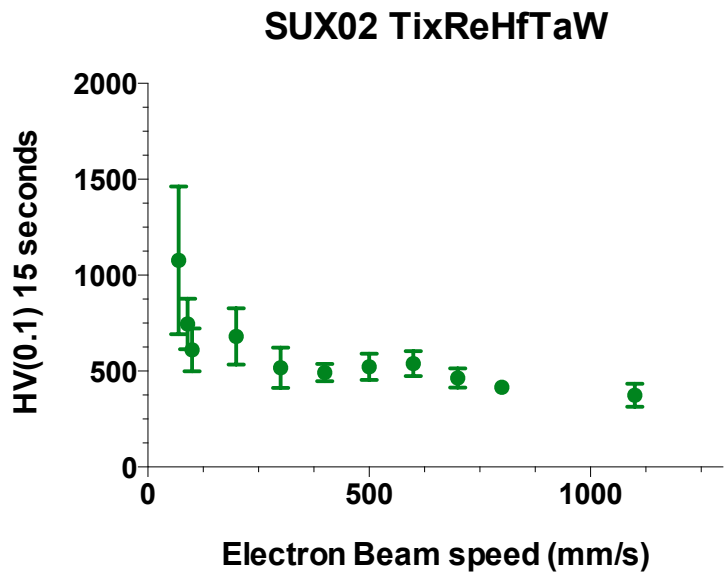

Fig. 6.12 Hardness values of the alloy system $Ti_xHfTaWRe$ according to the processing electron beam speed.

or machining.

The alloy system CrFeCoNi is recognised as a well-known HEA forming single fcc crystalline structure, which has been processed by methods such as arc melting or additive manufacturing [22], proving the simplicity of its crystalline structure as well as its interesting properties, such as its high strength and ductility [22], its corrosion resistance [43] and also its electrical resistivity[13] being comparable to conventional stainless steel, therefore making this particular alloy potentially suitable for applications similar to stainless steel. The stability of this alloy system when adding different 5th elements has also been of interest, showing the effect on structure of the addition of other metallic elements such as Al that stabilises the bcc phase [91] or the addition of Ti that produces the formation of multiple phases [12].

This section will discuss the use of consolidation of individual elemental powders (instead of pre-alloyed) by SPS, in order to explore the feasibility of the technique to produce basic net shape bulk packs from multicomponent high entropy alloys while completely removing the time consuming mechanical alloying stage.

Specimen	Temperature	Pressure	dwell time
	°C	kN	min
SPS1	1100	11	5
SPS2	1100	11	120
SPS3	1150	11	240

Table 6.2 SPS operational parameters used during the consolidation of FeCoCrNi.

6.2.2 Experimental approach

Elemental powders of Fe, Co, Cr and Ni, with high purity (99% purity) were mixed at equiatomic ratio and then 3 samples of 13 g each one have been consolidated by Spark Plasma Sintering. The temperature, pressure and duration of temperature dwell of each sample is shown in Table 6.2. For comparison, the same alloy system has been produced by arc melting and the crystalline structure of all samples has been analysed by X-ray diffraction.

6.2.3 Results and discussion

The crystalline structure of each sample has been examined by XRD and the corresponding x-ray traces are shown in Figure 6.13. The trace at the top of the graph corresponds to the arc-melted sample, whereas the other three traces correspond to the SPS-consolidated samples at different dwell times (from the bottom to the top: dwell time of 5 minutes, 2 hours and 4 hours).

The x-ray trace corresponding to the 5 minutes dwell time sample shows separate peaks of the 4 elements Fe, Co, Cr and Ni. As the dwell time increases from 5 minutes to 2 hours, the elements have further time to interdiffuse and the structure can therefore change. This can be observed through the evolution of the x-ray traces, where some of the peaks observed in the sample SPS-ed for 5 minutes disappear when increasing dwell time.

In addition, the peaks observed in the 2 hours SPS sample show non symmetric and high broadening peaks, which could be the effect of multiple peaks convoluted. This indicates that although there has been some diffusion, a homogeneous alloy has not been achieved.

The spatial distribution of elements of the SPS samples produced at 2 and 4 hours have been explored by EDX and the elemental maps are collected in Figures 6.14 and 6.15 for 2 and 4 hours dwell time respectively.

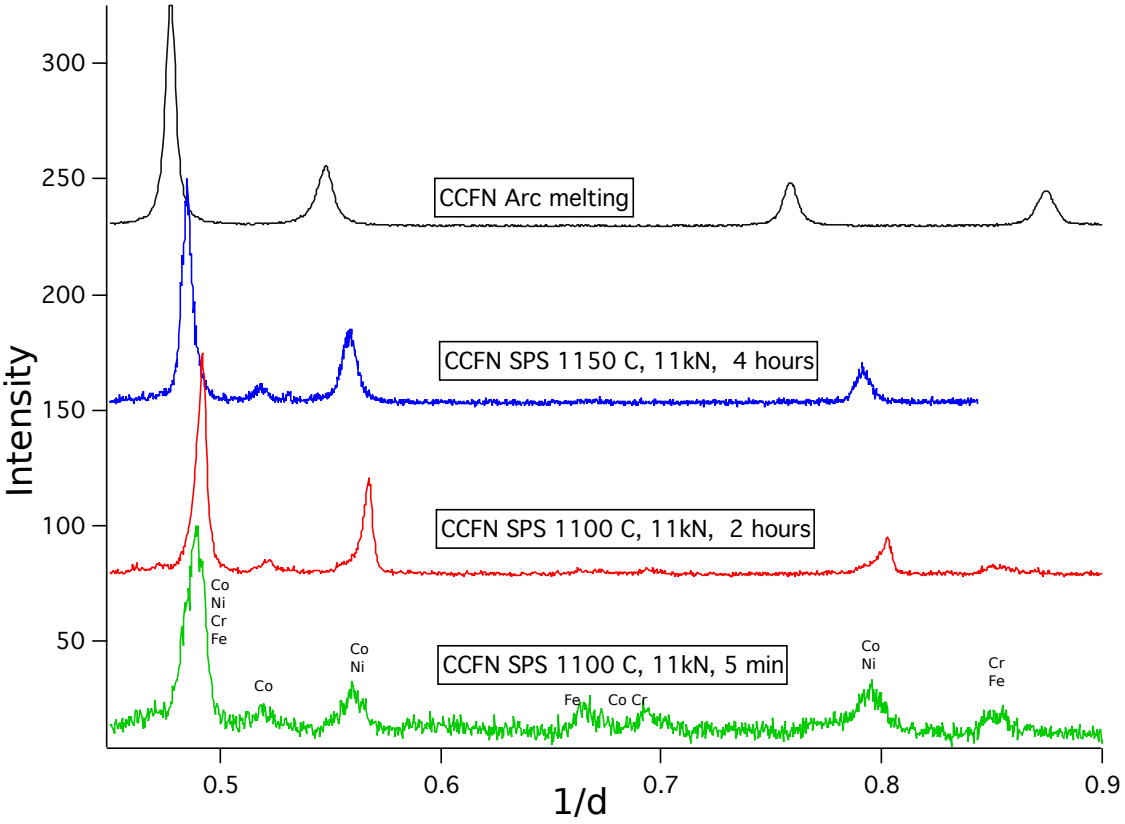

Fig. 6.13 X-ray traces of CrFeCoNi, from the bottom to the top: 5 min dwell time by SPS, 2 hours dwell time by SPS, 4 hours dwell time by SPS and the sample produced by arc melting.

Figure 6.14 is the elemental mapping of the SPS sample after 2 hours where individual particles of Ni and Co are still detected. After 4 hours consolidation (see Figure 6.15 a better diffusion between the 4 elements is achieved, although separation of some Ni and Co particles can still be observed, likely due to the effect of the sluggish diffusion rate between these elements.

The results obtained in the elemental mapping are in agreement with the crystalline structure observed in Figure 6.13, where a change in the crystalline structure is observed, but a single phase is not completely realised after 4 hours consolidation. This is understandable as for a similar alloy of this type, Tsai et al [13] observed slow diffusion between the elements within the HEA system composed of Fe Co Cr Ni and Mn, where it was found that Ni and Co interdiffuse slower than Fe and Cr.

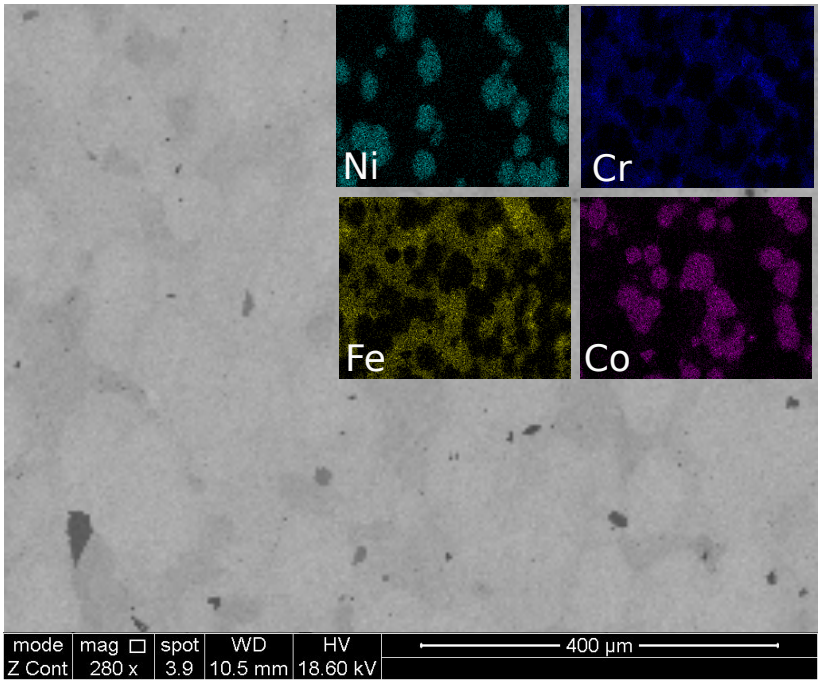

Fig. 6.14 EDX mapping of FeCoCrNi after 2 hours sintering in SPS in the centre.

It could be possible to achieve full alloying of the elements by increasing the extent of diffusion, either by increasing the temperature (to increase the rate) or increasing the dwell time (to allow more time for it to happen). A Differential Thermal Analysis, DTA of the alloy FeCoCrNi was performed by Brif et al. [22]. It was shown that no phase transformation occurs up to the melting point (1414 °C). This suggests that the formation of a stable single

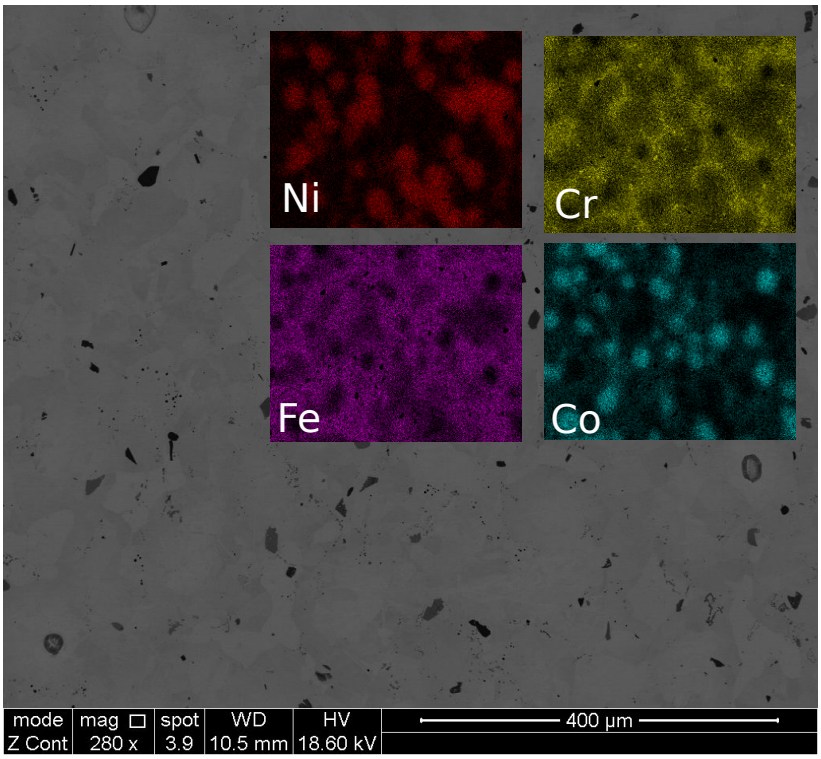

Fig. 6.15 EDX mapping of FeCoCrNi after 4 hours sintering in SPS in the centre.

face-centered cubic phase could be present whether the dwell time or temperature is increased.

6.2.4 Summary

In summary, the high throughput methodology validated in Chapter 4 and Chapter 5 has been used here for the discovery of novel HEAs. Three different alloy systems (Ti_xHfTaWRe, V_xTiMnNb and Zr_xTiNbHf) have been selected according to the prediction method (each predicted to form a single bcc structure) and have been synthesised through SPS and EBM. Different conditions were applied to the systems, and, as a result, it has been found that in this process the thickness of the foil seems to be a critical parameter for reaching a successful synthesis. When the thickness is too high, high electron beam energy is required and keyhole can be produced, creating a defective weld track. On the other hand, too small thickness of the foil requires a low energy that may be limited by the equipment. It is also important that the removal of residual carbon from the SPS is carried out carefully, as there is the potential to damage the foil and prevent the results form being systematic. If the correct conditions are achieved, as they are in the case of Ti_xHfTaWRe, then new alloy systems can be successfully made and investigated.

Characterization and testing of the synthesised samples have been carried out. SUX04, consisting of no more than 2 phases, has shown its simplicity in microstructure and achieves high hardness values.

The already-known HEA composed of FeCoCrNi has been produced directly by consolidation of elemental powders by Spark Plasma Sintering, SPS. According to the results, the formation of the stable single fcc phase has not been completely reached by the SPS process, even after a dwell time of 4 hours. However, a microstructural evolution with dwell time suggests that the simple fcc phase could be observed if higher dwell times and temperatures are used. The dwell times explored for the synthesis of the HEA CrFeCoNi are not conventional (most SPS processes use less than an hour) and although time consuming, is still lower than the time required for synthesising the alloy by other solid state techniques, such as mechanical alloying, which requires more than 30 hours in most cases.

Chapter 7

Conclusions and Future Work

7.1 Conclusions

The study set out to explore a Combinatorial High Throughput approach suitable for the discovery of novel High Entropy Alloys, and has identified the different stages of the conventional High Throughput approach as the library design, library fabrication, measurements and analysis.

On the one hand, combinatorial high throughput techniques are excellent approaches to implement not only for the discovery of novel material formulations but also for the optimization of already known systems, while reducing the time and cost compared to traditional procedures for material discovery.

Traditional metallic systems are composed of one or two principal elements with other additives used for improving the properties of the final material. This limits the discovery of new materials to the edges of the phase diagrams, leaving undiscovered the areas closer to the centre where multicomponent equiatomic systems such as High Entropy Alloys are located. The discovery of HEAs showed the potential of this region to harbour materials of interest with attractive combinations of functional and structural properties compared with those of conventional alloys.

The stability of HEAs has been explained through thermodynamics, interpreting the high entropy achieved within HEAs the main cause of their formation of simple single phases. In spite of the high number of components, the Hume-Rothery rules, used for understanding the stability of binary system have also been used to explain the solid solubility of HEAs where the effect of the atomic size difference, electronegativity and valence electron concentration

have been taken into consideration.

Principal Component Analysis, as a exploratory technique, has been used to understand and visualise the effect of several thermodynamic and electronic parameters on the stability of HEAs and their crystalline structure. This has not only visualised patterns between HEAs and their parameters, and the parameters themselves, but also allowed a better discrimination between simple and complex phases. In particular, when plotting the wider dataset of multi-component alloys the structures formed resolve themselves with an unusually high degree of consistency into largely separate regions on a plot of VEC against ΔH_{mix}. The explicit consideration of entropy is not required in this approach, possibly indicating that the picture of HEA determination being solely, or largely, due to this parameter is incorrect.

The original thermodynamic and electronic parameters have been used to obtain and visualise the relationship between variables and observations in the new orthogonal space between the main Principal Components, PCs. By projecting these observations and variables in the first 2-3 PCs, it has been possible to determine certain clustering of the crystalline structures. Further to this, PCA can also be used to obtain the original parameters when knowing the values of the observations and variables in the orthogonal space just by multiplying the covariance/correlation matrix by the inverse matrix.

PCA is an extraordinarily easy to manage and practical tool for the computational stage of the Combinatorial High Throughput Method. The development of a virtual library, which contains all the measurements and data collected from each different sample syntheses, could be used as the "feedback" technique that can collect the features of the novel discovered materials in order to improve the design stages.

Combinatorial high throughput techniques should allow synthesising multiple samples at a time followed by rapid characterisation. Sometimes, specific and new equipments are required for the performance of the combinatorial approach (for example, the EU FP7 collaborative project, Accelerated Metallurgy aims to build just such a specific device), however this is not always the case. For example, the combinatorial methodology developed in this project does not required any specific equipment for combinatorial processing, rather conventional equipment is used in a slightly different way to usual. For example, SPS has been used to consolidate powder together with a metallic foil instead of just a powder mixture; and the electron beam melting EBM equipment, typically used for the production of net-shape parts, has been used here for creating weld tracks at different operational parameters in the surface

of a metallic disk.

The combinatorial technique consists of the development of several weld tracks on the top surface of a specimen composed of a metallic foil and a mixture of elemental powders. Then, a screening technique will identify the number of phases present in the microstructures of each weld track by performing a quantitative phase analysis by image analysis methods.

For each iteration of the process as used here, an average of 16 weld tracks has been produced on the top surface of a 80mm disc (the density of these weld tracks could potentially be increased to obtain larger numbers of samples). Therefore, the time consumed when using a combinatorial method would produce 16 different samples, whereas traditional methods would produce 1 single sample. Besides, characterization and testing have also had a great influence in the determination of the combinatorial approach. A screening technique allows the location of the single phase HEAs for a certain composition to be found and automated hardness testing reduces the time consumed during data measurement.

The validation of the method, which has been carefully explained in chapter 5, has been possible by producing and characterising the known HEA $Ti_xFeCoCrNi$. The method is further used here for the discovery of novel HEAs, as seen in chapter 6.

Chapter 6 has been used to include the results obtained in the discovery of novel HEAs, where three alloy systems (SUX02, SUX03, SUX04) have been investigated. They are designed to form single phase HEAs, however, an invalid geometrical design and the extreme operational parameters selected produces defective weld tracks in the systems SUX02 and SUX03 while system SUX04 meets with success (Ti-ReWHfTa). In addition to this, Chapter 6 has also shown an alternative synthesis methodology by using only Spark Plasma Sintering for producing a single phase FeCoCrNi when increasing sintering time.

At this stage, it is needed to remind the reader that the scope of this project was mainly focused on the development of a technique suitable for the synthesis of multiple compositions at the same time. A small scale high-throughput synthesis methodology has been explained here and on top of that some novel HEAs have been discovered. On the contrary, not enough attention has been put to the understanding of the stability of those novel alloys to find out further details on their stablility. Therefore this should take am part of the future work of this project where heat treatment of these novel alloys should be performed.

As a global conclusion, this project started with the development of a technique that allows the discovery of novel HEAs in a combinatorial high throughput manner and this thesis has shown the validation of a suitable technique as well as its successful application for the discovery of novel refractory HEAs. This project has covered every stage of the process from the virtual library to the data analysis passing through the library production and measurement. In addition, 3 novel equiatomic HEAs and 4 different metallic systems have been produced within this project.

7.2 Future work

Improvement of high throughput methodology The properties achieved by these multiple principal element alloys have caught the interest of researchers and end users, increasing the investment of effort for the understanding of HEAs and ther suitability for potential applications.

An efficient combinatorial high throughput approach should produce and characterise as many samples as possible in a given time. Further improvement of the technique is required for the reduction of time consumed and to obtain a larger number of HEAs with the desired properties.

The effect of common impurities O, C and N on the phase chemistry was not undertaken but would likely be an important aspect of future work, since powder based processing of reactive alloys, and especially of pure elemental powders that are always particularly reactive, is frequently undermined by uncontrolled and sometimes excessive O and N pick up from the atmosphere, and C.

Design.

Chapter 4 has shown how the crystalline structure of HEAs is predicted according to some thermodynamic and electronic parameters. For instance, when the enthalpy of mixing of a metallic system is close to zero, single and simple fcc/bcc cystalline structures are found. As this value is increasingly negative, multiple phases are found, including intermetallic compounds, which overlap with bcc crystalline structures (as seen in Figure 4.2b). The discrimination between simple and complex phases (the overlapping) in this region is not completely understood, which means that further research is required. This overlapping may be reduced or, even better, removed if modifications in the design stage are performed.

In the collation of all the data collected at the end of each measurement in the virtual library will occur. As this dataset of alloy systems and properties builds up, performing PCA on the full dataset could help to visualise patterns that previously were not obvious (e.g. eliminate the overlapping between some single bcc alloys and others with multiple phases). Figure 7.1 shows an schematic of the PCA process used as a "feedback" technique.

Processing Improvements in the processing stage may also be possible. As shown in

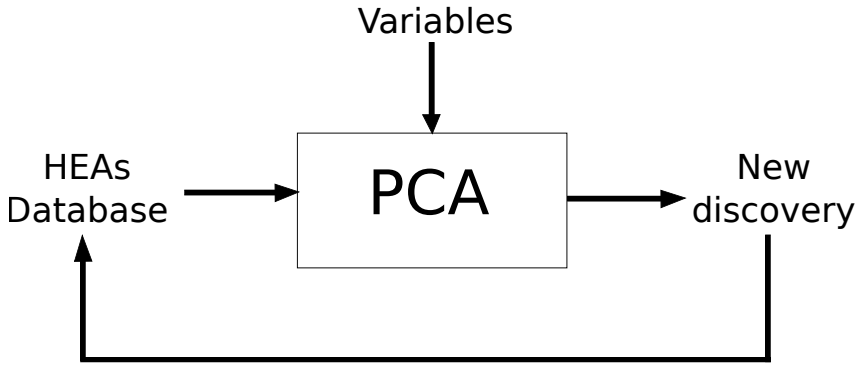

Fig. 7.1 Schematic of a feeding PCA cycle showing both the input and the output.

Chapter 5 and 6, each weld track follows a straight line trajectory of about 10-12mm length on all the samples. High penetration of the electron beam is achieved when increasing the electron beam power. This produces deeper penetration of electrons in the workpiece, producing undesirable keyholes in the centre of the melted pool and consequently wasted weld tracks for further testing.

Synthesis of samples using a extend variety of trajectories could be beneficial when performing a wide range of testing by producing different shapes and sizes of melted pools to be tested. Changing the trajectory may also help to eliminate the keyhole without modifications of the operational parameters. For this latter instance, when a single straight trajectory produces a weld track with a keyhole, this could be closed when using a figure-O or -8 trajectory (see a and b in Figure 7.2). In addition, if other required testing techniques need larger surfaces (e.g. wear testing), melting through rastering instead of single trajectories could be used to melt a large surface (see c and d in Figure 7.2).

Improvement can be obtained not just by modifying the trajectory of the electron beam, but also by increasing the number of systems able to be synthesised in one single step. Chapter 3 has explained how a single foil is consolidated on the top surface of a powder mixture, producing a sample as the one seen in Figure 7.3a. This could be improved by changing both

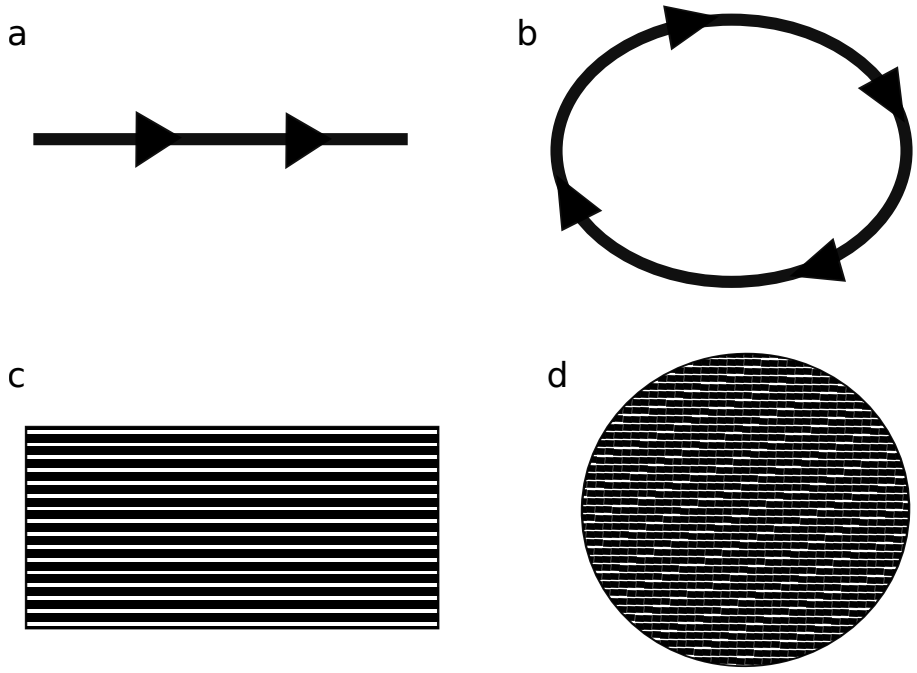

Fig. 7.2 Trajectories to follow up during melting: (a) single weld track; (b) circular weld track; (c) rectangular weld surface; (d) circular weld surface.

the operational parameters and the number of components used as foils. Figure 7.3b shows the specimen from the plant view when four different foils are used. In this case, the welding can be produced in the same manner in four different regions and therefore it would result in alloys with varying composition over 4 different metallic systems instead of a single one.

Testing The sections across the weld tracks have been mechanically tested, particularly under hardness testing. The average hardness of each weld track has been evaluated whilst accounting for a set of 9-20 indentations. As a high throughput test method, microhardness mapping would be useful for detecting different phases when Quantitative Phase Analysis, QPA is not suitable.

Further properties for the alloys could also be obtained. The size of the weld tracks limits the availability of techniques to the small scale. Some suitable testing are wear and microcompression. Wear testing could be performed on the top surface of the weld tracks along their length.

Microcompression has been used to study the effect of the size on the plastic behaviour and testing over a range of temperatures [92]. The samples produced by arc melting required for validation of the PCA technique (equiatomic TiMnFeNi, MnFeCoNi and TiVMnNb) have been provided to the collaborating group at the University of Cambridge for microcompres-

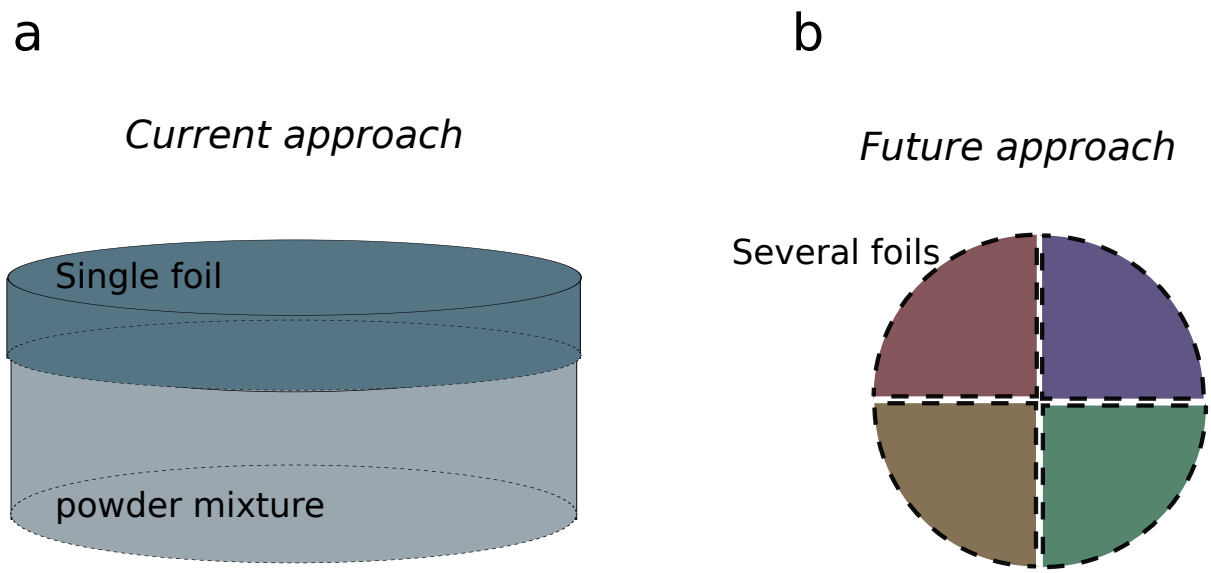

Fig. 7.3 Schematic of (a) the approach implemented within this project and (b) the approach proposed for further research.

sion testing within the AccMet project.

Samples synthesized within the project During the progress of this project, several metallic systems composed of a wide range of elements have been produced either by arc melting for validation of the PCA prediction shown in chapter 4 or by the combinatorial high throughput methodology explained in chapter 5.

The validation of the prediction method required the production of 3 metallic systems not included in the starting database and therefore considered novel systems. These systems are MnFeCoNi forming a single fcc phase, TiVMnNb forming a single bcc phase and TiMnFeNi forming multiple phases.

The validation of the combinatorial methodology has been validated and involved the production of 16 different compositions of the metallic system $Ti_xFeCoCrNi$ (SUX01). The hardness results cover a wide range between 400HV and 1100HV depending on the Ti quantity. Further testing of the sample reaching the highest HV would be of interest to verify its potential.

These alloys have a potential for application in aerospace, nuclear or medical such as this high hardness sample obtained in the $Ti_xFeCoCrNi$ system, samples composed of W

in Ti_xReHfTaW and biocompatible elements used in Zr_xTiNbHf. Further testing would be needed for proving the suitability of any of these HEAs but the indications from this work are that they are worthy of further study.

Automation For full implementation and achieving the High Throughput goals, the method could even be fully automated. The introduction of an invariant and consistent procedure, or even the implementation of self-controlled robotic equipment, which would continuously synthesize and characterise new materials, would reduce time consumed. Besides, all the measured data and movements of the robot would be stored in a PC in order to localise problems in case of faults.

Figure 7.4 shows the automatised processing route which could be followed every time a new system is produced. The work flow would be:
1) Design of the HEA according to the PCA predictions.
2) Select operational parameters of the SPS and EBW according to physical properties such as temperatures and desired weld tracks penetration (using Rosenthal equiation).
Systematic metallographic preparation of the weld tracks, following the same strategy. For example, for a 80 mm diameter disc: (1) cutting half weld tracks following the blue lines, (2) Mounting several weld tracks together in the same holder, (3) Grinding and polishing while following a general guideline and (4) performance of the same tipe of testing in the specimens.

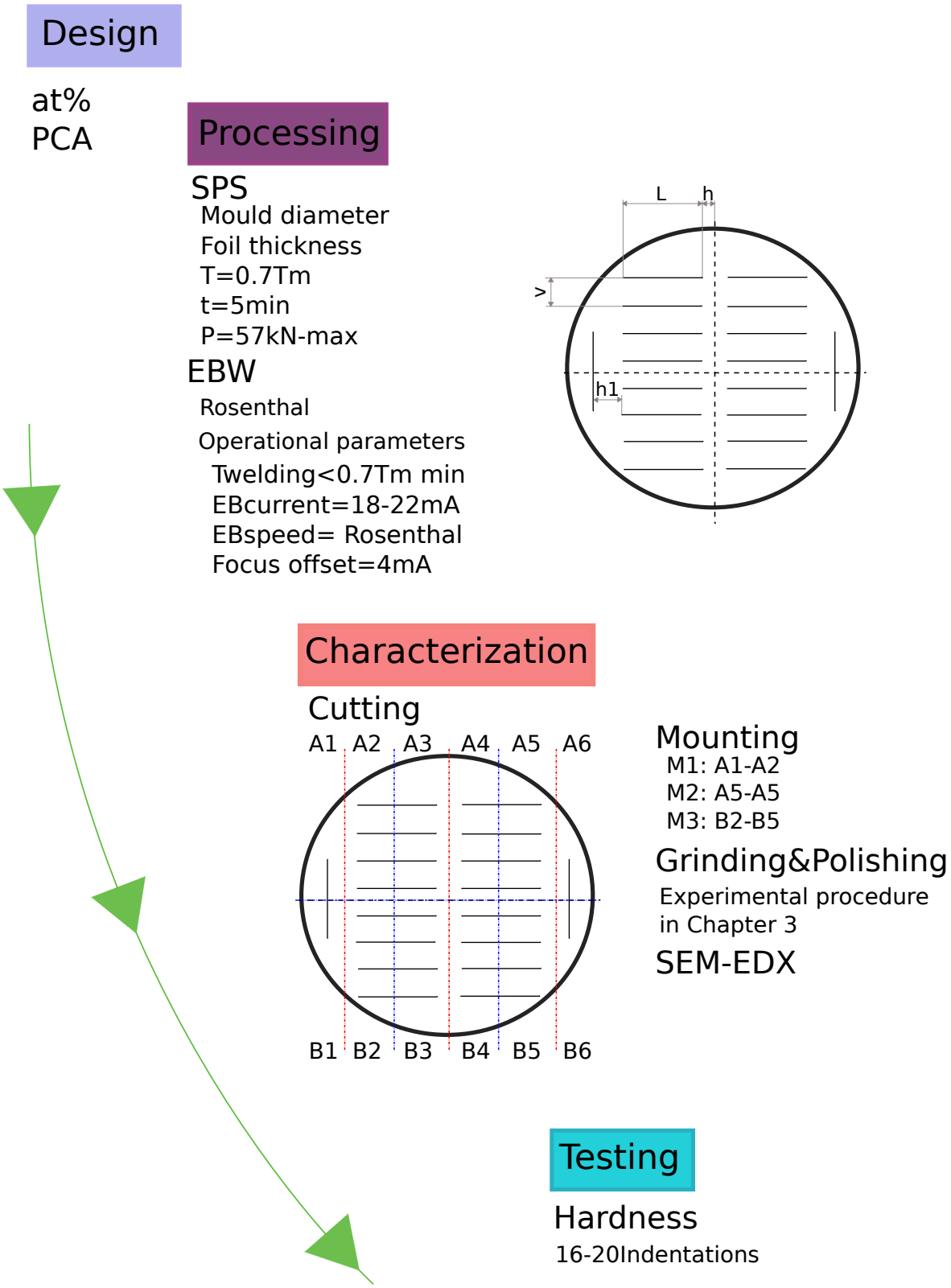

Fig. 7.4 Proposed automatised procedure for speeding up the discovery of HEAs.

References

[1] B Cantor. Multicomponent and High Entropy Alloys. *Entropy*, 16:4749–4768, 2014.

[2] J-W Yeh, S.-K. Chen, S.-J. Lin, J.-Y. Gan, T.-S. Chin, T.-T. Shun, C.-H. Tsau, and S.-Y. Chang. Nanostructured High-Entropy Alloys with Multiple Principal Elements: Novel Alloy Design Concepts and Outcomes. *Advanced Engineering Materials*, 6(5):299–303, May 2004.

[3] Y Zhang, Y J Zhou, J P Lin, G L Chen, and P K Liaw. Solid-solution phase formation rules for multi-component alloys. *Advanced Engineering Materials*, 10(6):534–538, 2008.

[4] X Yang and Yong Zhang. Prediction of high-entropy stabilized solid-solution in multi-component alloys. *Materials Chemistry and Physics*, 132(2-3):233–238, February 2012.

[5] Sheng Guo and C T Liu. Phase stability in high entropy alloys: Formation of solid-solution phase or amorphous phase. *Progress in Natural Science: Materials International*, 21(6):433–446, 2011.

[6] S Guo, C Ng, J Lu, and C T Liu. Effect of valence electron concentration on stability of fcc or bcc phase in high entropy alloys. *Journal of Applied Physics*, 109(103505):1–5, 2011.

[7] M G Poletti and L Battezzati. Electronic and thermodynamic criteria for the occurrence of high entropy alloys in metallic systems. *Acta Materialia*, 75:297–306, August 2014.

[8] W H Liu, Y Wu, J-Y He, Y Zhang, C-T Liu, and Z-P Lu. The Phase Competition and Stability of High-Entropy Alloys. *JOM*, 2014.

[9] Y Zhang, T-T Zuo, Z Tang, M C Gao, K A Dahmen, P K Liaw, and Z-P Lu. Microstructures and properties of high-entropy alloys. *Progress in Materials Science*, 61:1–93, 2014.

[10] Z. A. Munir, U. Anselmi-Tamburini, and M. Ohyanagi. The effect of electric field and pressure on the synthesis and consolidation of materials: A review of the spark plasma sintering method. *Journal of Materials Science*, 41(3):763–777, February 2006.

[11] H Giedt and L N Tallerico. Prediction of Electron Beam Depth of Penetration. 1988.

[12] T-T Shun, L-Y Chang, and M-H Shiu. Microstructures and mechanical properties of multiprincipal component CoCrFeNiTix alloys. *Materials Science and Engineering: A*, 556:170–174, 2012.

[13] M-H Tsai. Physical Properties of High Entropy Alloys. *Entropy*, 15(12):5338–5345, December 2013.

[14] C Stanley and C Smith. Materials and the Development of Civilization and Science. *Science, New Series*, 148(3672):908–917, 1965.

[15] J J Hanak. The "multiple-sample concept" in materials research: Synthesis, compositional analysis and testing of entire multicomponent systems. *Journal of Materials Science*, 5(11):964–971, 1970.

[16] G Briceno, H Chang, X Sun, Peter G Schultz, and X Xiang. A class of cobalt oxide magnetoresistance materials discovered with combinatorial synthesis. 270(October):273–275, 1995.

[17] A J B Vincent. *A study of three multicomponet alloys*. PhD thesis, University of Sussex, 1981.

[18] P Knight. *Multicomponent alloys*. Bsc part 2, Univeristy of Oxford, 1995.

[19] B Cantor, I T H Chang, P Knight, and A J B Vincent. Microstructural development in equiatomic multicomponent alloys. *Materials Science and Engineering: A*, 375-377:213–218, July 2004.

[20] J.W. Yeh. High-entropy multielement alloys, October 31 2002. US Patent App. 10/133,495.

[21] J-W Yeh, Y L Chen, S J Lin, and S K Chen. High-Entropy Alloys - a new era of exploitation. *Materials Science Forum*, 560:1–9, 2007.

[22] Y Brif, M Thomas, and I Todd. The use of high-entropy alloys in additive manufacturing. *Scripta Materialia*, 99:93–96, 2015.

[23] H Zhang, Y Pan, Y He, and H Jiao. Microstructure and properties of 6FeNiCoSiCrAlTi high-entropy alloy coating prepared by laser cladding. *Applied Surface Science*, 257(6):2259–2263, January 2011.

[24] J-W Yeh. Alloy Design Strategies and Future Trends in High-Entropy Alloys. *Jom*, 65(12):1759–1771, October 2013.

[25] A Takeuchi and A Inoue. Classification of Bulk Metallic Glasses by Atomic Size Difference, Heat of Mixing and Period of Constituent Elements and Its Application to Characterization of the Main Alloying Element. *Materials Transactions*, 46(12):2817–2829, 2005.

[26] S Fang, X Xiao, L Xia, W Li, and Y Dong. Relationship between the widths of supercooled liquid regions and bond parameters of Mg-based bulk metallic glasses. *Journal of Non-Crystalline Solids*, 321(1-2):120–125, June 2003.

[27] Y Dong, Y Lu, L Jiang, T Wang, and T Li. Effects of electro-negativity on the stability of topologically close-packed phase in high entropy alloys. *Intermetallics*, 52:105–109, September 2014.

[28] M. Kamal. The Role of Valence Electron Concentration on the Structure and Properties of Rapidly Solidified Sn-Ag Binary Alloys. *Materials Sciences and Applications*, 03(03):179–184, 2012.

[29] U Mizutani. *Introduction to the electron theory or metals*. Cambridge University Press, Cambridge, 2001.

[30] A Cunliffe, J Plummer, I Figueroa, and I Todd. Glass formation in a high entropy alloy system by design. *Intermetallics*, 23:204–207, April 2012.

[31] M G Poletti, G Fiore, B A. Szost, and L Battezzati. Search for high entropy alloys in the X-NbTaTiZr systems (X=Al, Cr, V, Sn). *Journal of Alloys and Compounds*, 620:283–288, 2015.

[32] C-C Tung, J-W Yeh, T-T Shun, S-K Chen, Y-S Huang, and H-C Chen. On the elemental effect of AlCoCrCuFeNi high-entropy alloy system. *Materials Letters*, 61(1):1–5, January 2007.

[33] T.M. Yue, H. Xie, X. Lin, H.O. Yang, and G.H. Meng. Solidification behaviour in laser cladding of AlCoCrCuFeNi high-entropy alloy on magnesium substrates. *Journal of Alloys and Compounds*, 587:588–593, February 2014.

[34] M H Tsai, J-W Yeh, and J Y Gan. Diffusion barrier properties of AlMoNbSiTaTiVZr high-entropy alloy layer between copper and silicon. *Thin Solid Films*, 2008.

[35] Z Fu, W Chen, Z Chen, H Wen, and E J Lavernia. Influence of Ti addition and sintering method on microstructure and mechanical behavior of a medium-entropy Al 0.6 CoNiFe alloy. *Materials Science and Engineering A*, 619:137–145, 2014.

[36] S. Praveen, B. S. Murty, and Ravi S. Kottada. Alloying behavior in multi-component AlCoCrCuFe and NiCoCrCuFe high entropy alloys. *Materials Science and Engineering A*, pages 83–89, 2012.

[37] W Ji, Z Fu, W Wang, H Wang, J Zhang, Y Wang, and F Zhang. Mechanical alloying synthesis and spark plasma sintering consolidation of CoCrFeNiAl high-entropy alloy. *Journal of Alloys and Compounds*, 589:61–66, 2014.

[38] M Baricco, M Palumbo, D Baldissin, E Bosco, and L Battezzati. Metastable phases and phase diagrams. *La Metallurgia Italiana*, (11), 2004.

[39] K N Ishihara. Thermodynamics and Kinetics of Metastable Phase Formation. In *Non-equilibrium Processing of Materials*, chapter 2, pages 5 – 20. Elsevier, 1999.

[40] M S Lucas, G B Wilks, L Mauger, J A Muñoz, Oleg N Senkov, E Michel, J Horwath, S L Semiatin, M B Stone, D L Abernathy, and E Karapetrova. Absence of long-range chemical ordering in equimolar FeCoCrNi. *Applied Physics Letters*, 100(25), 2012.

[41] O.N. Senkov, G.B. Wilks, D.B. Miracle, C.P. Chuang, and P.K. Liaw. Refractory high-entropy alloys. *Intermetallics*, 18(9):1758–1765, September 2010.

[42] O.N. Senkov, J.M. Scott, S.V. Senkova, D.B. Miracle, and C.F. Woodward. Microstructure and room temperature properties of a high-entropy TaNbHfZrTi alloy. *Journal of Alloys and Compounds*, 509(20):6043–6048, May 2011.

[43] Y-J Hsu, W-C Chiang, and J-K Wu. Corrosion behavior of FeCoNiCrCux high-entropy alloys in 3.5% sodium chloride solution. *Materials Chemistry and Physics*, 92(1):112–117, July 2005.

[44] B. Gorr, M. Azim, H.-J. Christ, T. Mueller, D. Schliephake, and M. Heilmaier. Phase equilibria, microstructure, and high temperature oxidation resistance of novel refractory high-entropy alloys. *Journal of Alloys and Compounds*, 624:270–278, 2015.

[45] O N Senkov, F Zhang, and J D Miller. Phase Composition of a CrMo0.5NbTa0.5TiZr High Entropy Alloy: Comparison of Experimental and Simulated Data. *Entropy*, 15(9):3796–3809, September 2013.

[46] W-Y Huo, H-F Shi, X Ren, and J-Y Zhang. Microstructure and Wear Behavior of CoCrFeMnNbNi High-Entropy Alloy Coating by TIG Cladding. *Advances in Materials Science and Engineering*, 2015:1–5, 2015.

[47] C-J Tong, Y-L Chen, S-K Chen, J-W Yeh, T-T Shun, C-H Tsau, S-J Lin, and S-Y Chang. Microstructure Characterization of Al x CoCrCuFeNi High-Entropy Alloy System with Multiprincipal Elements. 36, April 2005.

[48] Y Lu, Y Dong, S Guo, L Jiang, H Kang, T Wang, B Wen, Z Wang, J Jie, Z Cao, H Ruan, and T Li. A Promising New Class of High-Temperature Alloys: Eutectic High-Entropy Alloys. *Scientific Reports*, 4:6200, 2014.

[49] N. Liu, P.H. Wu, P.J. Zhou, Z. Peng, X.J. Wang, and Y.P. Lu. Rapid solidification and liquid-phase separation of undercooled CoCrCuFexNi high-entropy alloys. *Intermetallics*, 72:44–52, May 2016.

[50] Z Tang, L Huang, W He, and P K. Liaw. Alloying and processing effects on the aqueous corrosion behavior of high-entropy alloys. *Entropy*, 16:895–911, 2014.

[51] H.P. Chou, Y.S. Chang, S.K. Chen, and J-W Yeh. Microstructure, thermophysical and electrical properties in AlxCoCrFeNi (o< x< 2) high-entropy alloys. *Materials Science and Engineering B*, 163:184–189, 2009.

[52] I. Kunce, M. Polanski, and J. Bystrzycki. Structure and hydrogen storage properties of a high entropy ZrTiVCrFeNi alloy synthesized using Laser Engineered Net Shaping (LENS). *International Journal of Hydrogen Energy*, 38(27):12180–12189, September 2013.

[53] Y-F Kao, S-K Chen, J-H Sheu, J-T Lin, W-E Lin, J-W Yeh, S-J Lin, T-H Liou, and C-W Wang. Hydrogen storage properties of multi-principal-component CoFeMnTixVyZrz alloys, 2010.

[54] M H Tsai, C W Wang, C W Tsai, W J Shen, and J-W Yeh. Thermal Stability and Performance of NbSiTaTiZr High-Entropy Alloys Barrier for Copper Metallization. *Journal of The electrochemical Society*, 158(11):H1161–H1165, 2011.

[55] Y Zhang, T Zuo, Y Cheng, and P K Liaw. High-entropy alloys with high saturation magnetization, electrical resistivity, and malleability. *Scientific reports*, 3:1455, January 2013.

[56] W F Maier, K Stöwe, and S Sieg. Combinatorial and high-throughput materials science. *Angewandte Chemie (International ed. in English)*, 46(32):6016–67, January 2007.

[57] R Potyrailo, K Rajan, K Stoewe, I Takeuchi, B Chisholm, and H Lam. Combinatorial and High-Throughput Screening of Materials Libraries: Review of State of the Art. *ACS Comb. Sci*, 13:579–633, 2011.

[58] M J Fasolka and E J Amis. Combinatorial Materials Science: Measures of Success. In Balaji Narasimhan, Surya Mallapragada, and Marc D Porter, editors, *Combinatorial Materials Science*, chapter Chapter 1, pages 1–20. John Wiley & Sons, New Jersey, 1 edition, 2007.

[59] I T Jolliffe. Choosing a Subset of Principal Components or Variables. In *Principal Component Analysis*, Springer Series in Statistics, chapter 6, pages 111–149. Springer-Verlag, New York, 2nd edition, 2002.

[60] K R Gabriel. The biplot graphic display of matrices with application to principal component analysis. *Biometrika*, 58:453–467, 1971.

[61] Z Shen, M Johnsson, Z Zhao, and M Nygren. Spark Plasma Sintering of Alumina. *Journal of the American Ceramic Society*, 85(8):1921–1927, 2002.

[62] L. A. Stanciu, V. Y. Kodash, and J. R. Groza. Effects of heating rate on densification and grain growth during field-assisted sintering of α-Al2O3 and MoSi2 powders, 2001.

[63] Y Zhou, K Hirao, Y Yamauchi, and S Kanzaki. Effects of heating rate and particle size on pulse electric current sintering of alumina. *Scripta Materialia*, 48(12):1631–1636, 2003.

[64] A H Meleka. Thermal effects. In *Electron-beam Welding: Principles and Practice*, chapter 3, pages 77–111. McGraw-Hill, London, 1971.

[65] H Schultz. *Electron beam welding*. Abington, Cambridge, 1993.

[66] J W Elmer, W H Giedt, and T W Eagar. The transition from shallow to deep penetration during electron beam welding. *Supplement to the welding journal*, pages 167–176, 1990.

[67] H Schwarz. Mechanism of High-Power-Density Electron Beam Penetration in Metal. *Journal of Applied Physics*, 35(7):2020, 1964.

[68] X. Yang, Yong Zhang, and P.K. Liaw. Microstructure and Compressive Properties of NbTiVTaAlx High Entropy Alloys. *Procedia Engineering*, 36:292–298, January 2012.

[69] Y Zhang, X Yang, and P K Liaw. Alloy Design and Properties Optimization of High-Entropy Alloys. *JOM*, 64(7):830–838, July 2012.

[70] Y.J. Zhou, Y. Zhang, Y.L. Wang, and G.L. Chen. Microstructure and compressive properties of multicomponent Alx(TiVCrMnFeCoNiCu)100-x high-entropy alloys. *Materials Science and Engineering: A*, 454-455:260–265, April 2007.

[71] K Zhang and Z Fu. Effects of annealing treatment on phase composition and microstructure of CoCrFeNiTiAlx high-entropy alloys. *Intermetallics*, 22:24–32, March 2012.

[72] J.M. Zhu, H.M. Fu, H.F. Zhang, a.M. Wang, H. Li, and Z.Q. Hu. Microstructures and compressive properties of multicomponent AlCoCrFeNiMox alloys. *Materials Science and Engineering: A*, 527(26):6975–6979, October 2010.

[73] J-W Yeh, S-Y Chang, Y-D Hong, S-K Chen, and S-J Lin. Anomalous decrease in X-ray diffraction intensities of Cu–Ni–Al–Co–Cr–Fe–Si alloy systems with multi-principal elements. *Materials Chemistry and Physics*, 103(1):41–46, May 2007.

[74] S. Varalakshmi, M. Kamaraj, and B.S. Murty. Processing and properties of nanocrystalline CuNiCoZnAlTi high entropy alloys by mechanical alloying. *Materials Science and Engineering: A*, 527(4-5):1027–1030, February 2010.

[75] C. Li, J.C. Li, M. Zhao, and Q. Jiang. Effect of alloying elements on microstructure and properties of multiprincipal elements high-entropy alloys. *Journal of Alloys and Compounds*, 475(1-2):752–757, May 2009.

[76] X.F. Wang, Yong Zhang, Y. Qiao, and G.L. Chen. Novel microstructure and properties of multicomponent CoCrCuFeNiTix alloys. *Intermetallics*, 15(3):357–362, March 2007.

[77] B. Ren, Z.X. Liu, D.M. Li, L. Shi, B. Cai, and M.X. Wang. Effect of elemental interaction on microstructure of CuCrFeNiMn high entropy alloy system. *Journal of Alloys and Compounds*, 493(1-2):148–153, March 2010.

[78] T Nagase, S Anada, P D. Rack, J H Noh, H Yasuda, H Mori, and T Egami. MeV electron-irradiation-induced structural change in the bcc phase of Zr–Hf–Nb alloy with an approximately equiatomic ratio. *Intermetallics*, 38:70–79, July 2013.

[79] I Toda-Caraballo, E I. Galindo-Nava, and P E J Rivera Diaz del Castillo. Unravelling the materials genome: Symmetry relationships in alloy properties. *Journal of Alloys and Compounds*, 566:217–228, July 2013.

[80] B. H. Flowers and E. Mendoza. *Properties of Matter*. John Wiley & Sons Ltd., London, 1st edition, 1970.

[81] Stefano Curtarolo, Aleksey N Kolmogorov, and Franklin Hadley Cocks. High-throughput ab initio analysis of the Bi–In, Bi–Mg, Bi–Sb, In–Mg, In–Sb, and Mg–Sb systems. *Calphad*, 29(2):155–161, June 2005.

[82] Stefano Curtarolo, Wahyu Setyawan, Shidong Wang, Junkai Xue, Kesong Yang, Richard H. Taylor, Lance J. Nelson, Gus L.W. Hart, Stefano Sanvito, Marco Buongiorno-Nardelli, Natalio Mingo, and Ohad Levy. AFLOWLIB.ORG: A distributed materials properties repository from high-throughput ab initio calculations. *Computational Materials Science*, 58:227–235, June 2012.

[83] D B Miracle, J D Miller, O N Senkov, C Woodward, M D Uchic, and J Tiley. Exploration and development of high entropy alloys for structural applications. *Entropy*, 16(1):494–525, January 2014.

[84] N Taniguchi, T Miyazaki, I Miyamoto, and T Miyazaki. Electron beam processing. In *Energy-beam processing of materials: advanced manufacturing using various energy sources*, chapter 3, pages 138–199. Oxford Series on Advanced Manufacturing, Oxford (UK), 1989.

[85] P C Angelo and R Subramaina. Presintering Operations. In *Powder metallurgy: science, technology and applicaitons*, chapter 8, pages 175–183. PHI - New Delhi, India, 1st edition, 2008.

[86] M S. El-Genk and J M Tournier. A review of refractory metal alloys and mechanically alloyed-oxide dispersion strengthened steels for space nuclear power systems. *Journal of Nuclear Materials*, 340(1):93–112, April 2005.

[87] G E. Lloyd. Atomic Number and Crystallographic Contrast Images with the SEM: A Review of Backscattered Electron Techniques, 1987.

[88] W Rostoker and J R Dvorak. Solid state transformation. In *Interpretation of metallographic structures*, page 157. Academic press, London, 2nd edition, 1977.

[89] G F Vander Voort. Volume 9: Metallographic and Microstructures. In *ASM Handbook*, page 1184. ASM International, 2004.

[90] W Ji, W Wang, H Wang, J Zhang, Y Wang, F Zhang, and Z Fu. Alloying behaviour and novel properties of CoCrFeNiMn high-entropy alloy fabricated by mechanical alloying and spark plasma sintering. *Intermetallics*, 56:24–27, 2015.

[91] W-L Wang and J-W Yeh. Phases, microstructure and mechanical properties of AlxCoCrFeNi high-entropy alloys at elevated temperatures. *Journal of Alloys and Compounds*, 589:143–152, March 2014.

[92] S Korte, R J. Stearn, J M. Wheeler, and W J. Clegg. High temperature microcompression and nanoindentation in vacuum, Jan 2012.

Appendix A

Matlab and Scilab codes

Calculation of thermodynamic and electronic parameters of multicomponent high entropy alloys

As an example, the code shows the calculation of the thermodynamics and electronic parameters of the alloy system $Al_{20}Mg_{23}Co_{18}Cu_{18}Zn_{18}$.
First of all, it will load 2 matrices: (1) MT.mat and (2) AH.mat;

- (1) MT.mat contains elemental properties per columns such as melting point, atomic size, valence, electronegativity, atomic weight and density whereas each row is a different element ordered by atomic number (furthermure, the row number coincides with the atomic number so thus it makes easy to add any element).
- (2) AH.mat contains the values of ΔH_{mix}^{AB} of the element A and B obtained from a table from the literature developed by [25]

Secondly, each column of MT.mat is identified; C is the percentage of each element and is located into the first column, Tm is the melting point and is located into the second column, and so on.
Then, the calculation of the parameters begins with "for" loops, whereas there will be as many loops as elements in the alloy. In the example, there are 5 elements, so thus 5 loops (one "for" for each element). This way of calling the elements is useful when the parameters of many different compositions need to be calculated, otherwise the loops could be avoid. Nevertheless, once the elements are called, the parameters can be calculated as shown in the equations in the literature review.
Finally, the code will print the matrix SS, which contains the composition of the alloy/s and the values of the parameters of interest.

```
load('AH.mat');clear MT; load('MT.mat');
IDENTIFICATION OF EACH COLUMN IN MT.mat
C=MT(:,1);% percentage
Tm=MT(:,2);%melting temperature
r=MT(:,3);%atomic size
vec=MT(:,4);%valence
x=MT(:,5);%electronegativity
Aw=MT(:,6);%atomic weight
Di=MT(:,7);%density at room temperature
format long
ss=zeros(2,15);
p=1
%A=2;
%B=0.5;
for Al=0.2;%0:B:A;
C(13)=Al;
for Mg=0.23;
C(12)=Mg;
for Co=0.18;%:B:A;
C(27)=Co;
for Cu=0.18 %0:B:A;
C(29)=Cu;
for Zn=0.18;%0:B:A;
C(30)=Zn;
sum(C) % It must be one
%calculate melting point, Tm
Tm_av = sum(C.*Tm);
% Calculate Atomic weight
Aw_av = sum(C.*Aw);
% Calculate Electronegativity difference
X_av = sum(C.*x);
AX = sqrt(sum(C.*(x-X_av).^2));
%density column 7
num = sum(C.*Aw);
den = sum(C.*Aw./Di);
D_av = num/den;
```

```
%calculate AHmix
for i=3:80;
for j=3:80;
AHij(i,j) = C(i).*C(j).*AH(i,j);
end
end
s = sum(AHij); AHmix = 4.*sum(s');
%calculate ASmix
n=80;
for k = 1 : n
if C(k) == 0
F(k) = 0;
else
F(k) = C(k).*log(C(k));
end
end
ASmix = -8.314.*sum(F);
%ratio omega
Om = Tm_av.*ASmix./(1000*abs(AHmix));
% atomic size difference, delta
r_av = sum(C.*r);
delta = 100.*((sum(C.*(1-(r./r_av)).^2)).^0.5);
VEC = sum(C.*vec);
%calculate critical temperature, Tc
Tc = 1000*abs(AHmix)/ASmix;
s=[C(13) C(12) C(27) C(29) C(30) D_av Om Tm_av Tc AHmix ASmix delta VEC AX Aw_av];
ss(p,:) = s;
p = p+1
end
end
end
end
end
```

Matlab code used to perform the Principal Component Analysis

load('rev.mat'); load('ob'); %rev.mat is the matrix containing the whole series of data.
%descriptive statistics
mean=mean(rev)
standard-deviation=std(rev)
%correlation matrix
$[R,P] = corrcoef(rev)$
%Eigenvalues and eigenvectors
$[V,D] = eig(R)$;
%ordering V,D
D2=diag(sort(diag(D),'descend'));% make diagonal matrix out of sorted diagonal values of input D
$[c,ind] = sort(diag(D),$'descend'); % store the indices of which columns the sorted eigenvalues come from
$V2 = V(:,ind)$; % arrange the columns in this order
Eigenvalue=diag(D2)
Eigenvector=V2 %Coefs=Eigenvector;
%PRINCIPAL COMPONENT ANALYSIS ON THE CORRELATION MATRIX
var='DHmix' 'DSmix' 'd' 'VEC' 'DX';
%[coefs,score,latent]=pca(PCV);%covariance matrix
[coefs,score,latent,tsquare]=princomp(zscore(rev));%correlation matrix z-score: standardized values
coefs
latent
cumsum(latent)./sum(latent)
components='PC1', 'PC2','PC3','PC4','PC5';
pareto(latent, components)
%3D BIPLOT REPRESENTATION
biplot(coefs(:,1:3), 'scores', score(:,1:3),'varlabels',var,'obslabels',ob) %cov matrix.
%2D BIPLOT REPRESENTATION
%biplot(coefs(:,1:2), 'scores', score(:,1:2),'varlabels',var,'obslabels',PCobsrev) %cov matrix.

Prediction of weld tracks

n=0.8 //efficiency

//OPERATIONAL PARAMETERS
I=20; //CURRENT [mA]
V=60;//Voltaje [kW]
S=1.3;//beam velocity [m/s]

//MATERIALS PROPERTIES AT BUILDING TEMPERATURE (in the case of the compositional gradient, the material properties to choose would be the properties of the material used as a foil)

//Material: HEA CoCrFeNi + Ti Foil

$k = 23$; //thermal conductiviy [W/mK] "of titanium at 25 C deg"(for pro beam). if using arcam with pre-heating, the values should be at built temperature.
$Tb = 300$;//building temperature [K] (25 C deg)
$Tl = 2506$;//liquidus temperature [K]
$ro = 13310$;//density [kg/m3] CONSIDERING THAT DENSITY VARIATION ON SOLID STATES IS MINIMUM
$Cp = 143.64$;//specific heat capacity [J/kgK]
alpha=k/(Cp*ro); //thermal difusivity [m2/s]

//Rosenthal equation
$P = I*V*n$;//effective powder of the electron beam
$thetam = Tl - Tb$; //maximun difference of temperature from the plate
$x = 0.001709$; //aproximation of x coordinate for peak temperature
$C1 = P/(2*\%pi*k*thetam)$;
$C2 = 2*alpha$;

//Newton-Raphson method for depth approximation
$F = C1*exp(-S*x/(S*x+C2)) - x$;
$dF = C1*exp(-S*x/(S*x+C2))*(-S*(S*x+C2)+S*(-S*x))/(S*x+C2)^2 - 1$;
$xn = x - F/dF$
$x = xn$; //Run Newton-Raphson Method untill $x = xn$

$RMB = x$;
$xMB = (-S*RMB^2/(S*RMB+C2))$
$D = (RMB^2 - xMB^2)^0.5$ //Depth of weld track [m]

$Depthmm = D * 1000$